OCCLUSION OF OIL DROPLETS WITHIN INORGANIC HOST CRYSTALS FOR LAUNDRY APPLICATIONS

Aikaterini Tatani

Supervisor: Prof. Steven P. Armes

Department of Chemistry

The University of Sheffield

ABSTRACT

Well-defined spherical diblock copolymer nanoparticles were synthesised by reversible addition-fragmentation chain transfer (RAFT) aqueous emulsion polymerisation of 2-ethylhexyl methacrylate using a water-soluble poly(methacrylic acid) precursor as a steric stabiliser. These nanoparticles are homogenised with a model oil (methyl myristate) under high shear with subsequent high pressure microfluidisation leading to the formation of oil-in-water nanoemulsions. The relative low glass transition temperature of the hydrophobic poly(2-ethylhexyl methacrylate) block leads to *in situ* dissociation of the nanoparticles, with the resulting strongly amphiphilic block copolymer chains acting as a polymeric surfactant for the oil droplets. This wholly aqueous route to nanoemulsions represents a useful improvement on a recent report that utilised RAFT dispersion polymerisation of lauryl methacrylate in methanol (Y. Ning et al., *Chem. Sci*. **2019**, *10*, 8964-8972). The model oil was then replaced with various hydrophobic multicomponent fragrances supplied by the industrial sponsor of this project (Procter & Gamble). The poly(methacrylic acid) block confers anionic character on the oil droplets, which enables their occlusion within calcium carbonate (calcite) crystals prepared *in situ* by the ammonia diffusion method at pH 9. Given the environmentally benign nature of the inorganic host matrix, such oil-loaded crystals offer a potential new biocompatible matrix for fragrance encapsulation/release in laundry applications. Systematic variation of the mean degree of polymerisation of the hydrophobic block indicated that poly(methacrylic acid)$_{138}$-poly(2-ethylhexyl methacrylate)$_{45}$ gave the best emulsifier performance for the production of stable nanoemulsions in which the oil phase comprised a multi-component fragrance. Scanning electron microscopy studies of oil-loaded calcite crystals confirmed the successful occlusion of micron-sized droplets. Thermogravimetric analysis indicated a maximum oil loading of 8.3% by mass for optimised formulations.

TABLE OF CONTENTS

ACKNOWLEDGEMENTS

I would firstly like to thank Prof. Steve Armes for giving me the opportunity to become a member of his group for my postgraduate studies. His guidance, support and understanding has been very much appreciated and I am incredibly grateful for all the skills I acquired as an Armes Group member. I would also like to thank Dr. Yin Ning for all the help, guidance and teaching he provided me with since I joined the group and also for being a great friend to me. A big thank you goes to the members of the Armes group for making my time in the office and the lab a very enjoyable one - especially to Csilla, as working with her was one of my highlights in the Armes group.

My research project was funded by EPSRC and Procter & Gamble (P & G). I would like to thank Dr. Johan Smets and An Pintens of P & G's Research Center in Brussels for supporting my project, for the time I spent in their laboratory in Brussels and for kindly providing me with the necessary raw materials to conduct my experiments.

Thank you to my friends here in Sheffield, Hüseyin, Konstantina, Olympia and Sotiria for their love and support during these two memorable years. I would also like to thank my other friends that despite the distance, were always there for me, such as Maritina, Christina, Sara and Marcel.

Last but not least, I want to express my greatest gratitude to my parents and my brother for supporting me through this very valuable experience. I am so grateful for having such a wonderful family, including my extended family from back home. I would like to dedicate this Thesis to my parents, Dimos & Elena, as I would not have made it this far without their support.

1. INTRODUCTION

The Fast-Moving Consumer-Goods (FMCG) sector is one of the largest global industries, with international annual sales exceeding $66 billion.[1] FMCG products such as cosmetics, laundry formulations and fabric softeners are sold in more than 160 countries by many global companies such as Nestlé AG and Procter & Gamble. There is no doubt that such household products have a huge beneficial impact on the daily lives of millions of people. Nevertheless, there is plenty of room for improvement. Government legislation regarding consumer product ingredients are becoming ever stricter in terms of sustainability, with the aim of minimising long-term environmental impact. For example, the European Union is becoming a leader in the reduction of waste plastic, with a ban on up to 90% of microplastic pollutants starting in 2020.[2,3] Microplastics are very commonly used in FMCG products, particularly laundry formulations. For example, melamine formaldehyde (MF) resin is a versatile thermoset copolymer that is widely used for the microencapsulation and release of volatile fragrances.[4] An example of such MF capsules of approximately 40 μm diameter is illustrated in Figure 1: Williams et al. recently prepared MF-coated Pickering emulsions in collaboration with P & G.[5] However, the melamine and formaldehyde building blocks are known to be both toxic and carcinogenic. Thus, alternative routes to microencapsulation are urgently being sought, preferably involving minimal use of synthetic polymers to avoid the new regulations governing the use of microplastics.

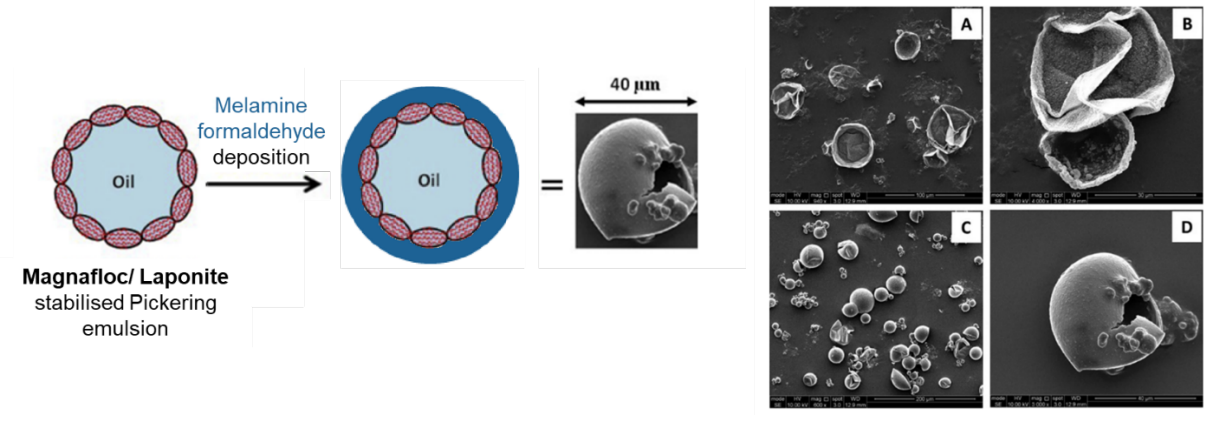

Figure 1. Melamine formaldehyde-coated microcapsules derived from Laponite-based Pickering emulsions for potential laundry formulation applications.[5]

Recently, formaldehyde-free microcapsules have been designed that are based on less harmful polymers, such as polyurethanes, poly(methyl methacrylate) or poly(lactic acid). However, such materials still fall foul of the microplastics ban that many

countries are expected to introduce in the near future. Thus, the work described in this Thesis focuses on developing an alternative environmentally friendly alternative technology for the encapsulation of multicomponent fragrances to be used in laundry products such as fabric conditioners. Ideally, such microcapsules require fragrance retention for 12-18 months with triggered fragrance release being achieved on demand via a pH switch or a change in temperature, or by mechanical action. In principle, using inorganic crystals for fragrance encapsulation should avoid the use of toxic, non-(bio)degradable polymers in home care formulations. For example, calcium carbonate ($CaCO_3$) is one of the most abundant naturally-occurring biominerals.[6] It exists in various crystal polymorphs such as calcite, vaterite and aragonite and is of tremendous significance for various living organisms.[7] It is also widely used for various industrial applications, such as paints & coatings, paper manufacture, construction,[8] the oil & gas industry [9] and biomedical applications.[10] In principle, synthetic polymers can be used to improve the mechanical properties of $CaCO_3$-based biominerals provided they are used at relatively low concentrations (ca. 0.1 – 0.2% by mass) to remain compliant with microplastics legislation. More specifically, anionic amphiphilic diblock copolymer emulsifiers can act as emulsifiers to form oil-in-water nanoemulsions. Then $CaCO_3$ can be grown in the presence of such microscopic oil droplets to produce oil-loaded calcite crystals, see Figure 2. Ning et al. have shown that pure oils such as methyl myristate, squalene or sunflower oil can be encapsulated using this approach, but in principle it could be extended to include multicomponent fragrances as well.[11]

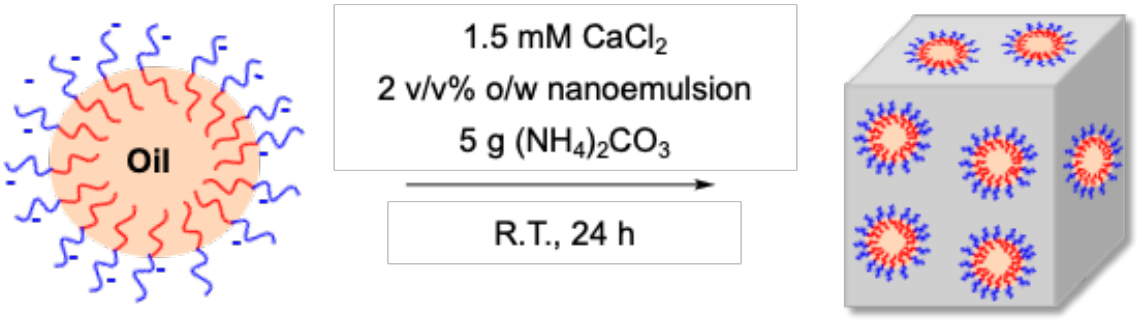

Figure 2. Occlusion of oil droplets stabilised via amphiphilic diblock copolymer chains within growing calcite crystals, as recently reported by Ning and co-workers.[11]

2. Literature Review

2.1 Polymer Chemistry

Polymers are long-chain molecules, also known as macromolecules, that consist of many repetitive sub-units, or monomers.[12] Polymers can be either naturally-occurring (e.g. DNA and cellulose) or man-made (e.g. polypropylene and polystyrene): they can exhibit a remarkably diverse range of physical properties, making them essential to modern life. Indeed, the field of polymer science has been advancing remarkably over the past few decades. Applications for synthetic polymers now include textile fibres for clothing and bed linen, latex binders for paints and coatings, fire-retardant materials for electrical cable insulation, non-stick surfaces for kitchenware, highly transparent materials for contact lenses and spectacles, and biomedical devices such as plastic heart valves.[13–18] The mean number of monomer repeat units per polymer chain is known as the mean degree of polymerisation, or DP. Polymers may consist of many repeat units of the same monomer (homopolymers) or can comprise two or more comonomers (copolymers).[19] Various polymer architectures are known, such as linear homopolymers, block copolymers, statistical (or random) copolymers, alternating copolymers, and graft copolymers, see Figure 3.[20] Non-linear examples include branched copolymers and gel networks. This Thesis will focus on amphiphilic diblock copolymers and their self-assembly to form sterically-stabilised nanoparticles in aqueous media.

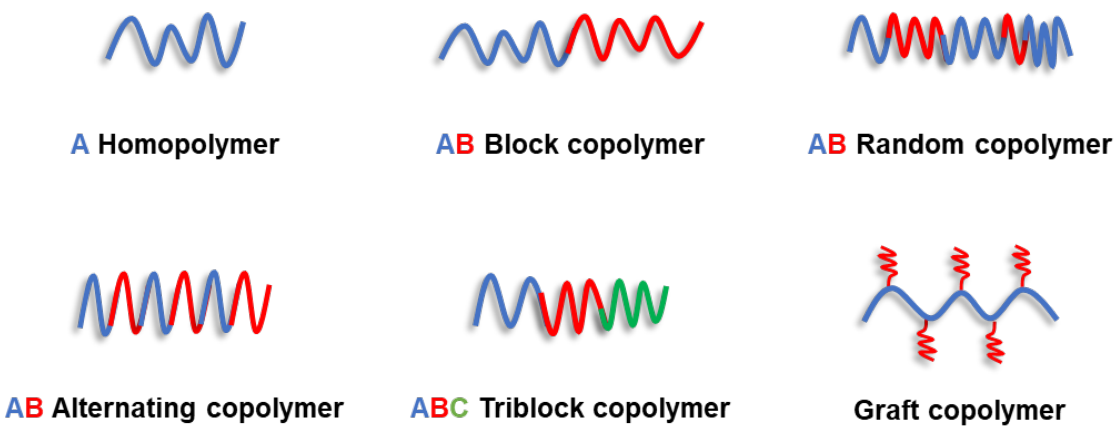

Figure 3. Examples of various polymer architectures.

Many polymer properties (e.g. fibre strength or latex film adhesion) depend on the DP of the polymer chains. Unlike small molecules, polymers are polydisperse materials, meaning that they do not exhibit a discrete molecular weight. Instead, they exhibit a

molecular weight distribution. There are two common moments of such molecular weight distributions. One is the number-average molecular weight (M_n), which is calculated using equation (1):

$$M_n = \frac{\Sigma n_i M_i}{\Sigma n_i} \quad (1)$$

Here n_i represents the number of polymer chains with i repeat monomer units and M_i is the molecular weight of these chains. Alternatively, the weight-average molecular weight (M_w) can be used, as defined according to Equation 2.

$$M_w = \frac{\Sigma n_i M_i^2}{\Sigma n_i M_i} \quad (2)$$

This parameter is more biased towards the longer chains within the molecular weight distribution. A schematic representation of a molecular weight distribution curve is shown in Figure 4 to illustrate the difference between M_n and M_w.

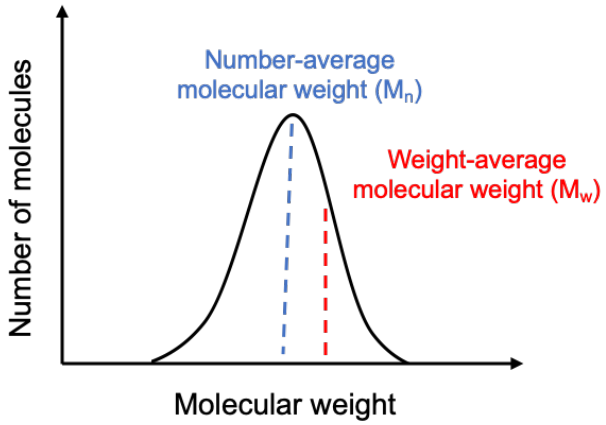

Figure 4. Schematic representation of the molecular weight distribution for a polymer, illustrating the difference between M_n and M_w.[21]

The dispersity (*Đ*), or M_w/M_n ratio, is defined according to Equation 3.

$$Đ = \frac{M_w}{M_n} \quad (3)$$

For some naturally-occurring polymers such as certain proteins or DNA, the dispersity can be unity, which means that all the polymer chains have precisely the same length and mass. However, for all synthetic polymers, Đ is greater than unity, indicating a molecular weight distribution curve of finite width.[22] In fact, the dispersity can be used

as a crude measure of the width of the molecular weight distribution curve. Since the 1950s, various polymerisation techniques have been developed to prepare so-called near-monodisperse polymers, for which *Đ* is less than 1.20.

Depending on the mechanism for their synthesis, polymers can be categorized as either *step-growth* polymers or *chain-growth* polymers. Step-growth polymerisation involves the gradual build-up of high molecular weight polymer chains over a prolonged period of time via series of step-wise reaction between monomers, oligomers etc.[23] Examples include the synthesis of polyesters or Nylon for textile applications. However, step-growth polymerisation is not relevant to this Thesis and so will not be discussed further. Chain-growth polymerisations can produce high-molecular weight polymers very rapidly via addition of multiple monomer units to the growing chain-ends. Chain-growth polymerisation can be conducted using anions, cations or free radicals. Only the latter species are relevant to this Thesis. There are two types of free radical-based chain-growth polymerisations: one is uncontrolled while the other is relatively well-controlled, see the red and blue curves respectively shown in Figure 5.[24] In this Thesis, a type of well-controlled chain-growth polymerisation is used to control the molecular weight distribution and copolymer architecture of the final product. In this case, the polymer molecular weight increases linearly with the monomer conversion, see Figure 5. In the following section, various chain-growth polymerisation techniques are discussed.

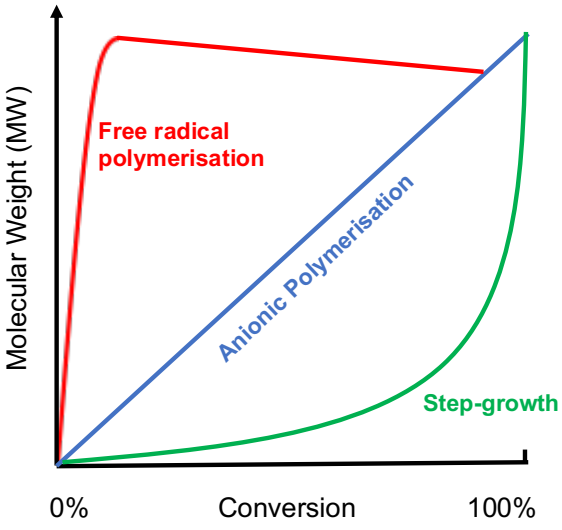

Figure 5. Evolution of molecular weight with monomer conversion for uncontrolled (red curve) and well-controlled (blue curve) chain-growth polymerisations, and also step-growth polymerisation (green curve).

2.2 Free radical polymerisation

Free radical polymerisation is a type of uncontrolled chain-growth polymerisation that is widely used for the industrial manufacture of vinyl polymers.[25] Many functional monomers can be used and this technique is tolerant of protic solvents and the presence of impurities.[26] Free radical polymerisation can be performed in various conditions, including in solution, under emulsion or dispersion conditions, or even in the bulk.[27] The polymerisation mechanism comprises four main steps: *initiation*, *propagation*, *chain transfer* and *termination*, see Figure 6.

A radical polymerisation is initiated once the initiator has undergone unimolecular decomposition to produce primary radicals (I$^{\bullet}$). The initiator is typically a compound possessing a bond with a relatively low dissociation energy, which can undergo homolytic fission under mild conditions.[28] Some examples of suitable initiators include azo compounds, peroxides or persulfates.[29] Thermal decomposition is usually used to generate a radical flux. This step is relatively slow and normally dictates the overall kinetics of polymerisation.

Once the primary radicals are formed, they react almost instantaneously with the vinyl monomer to produce monomer-initiator radicals (M$^{\bullet}$). These species then react with further monomer units to form a propagating polymer chain ($P_n^{\bullet}$), which grows rapidly (chain growth is typically complete within a fraction of a second). Throughout the polymerisation, various chain transfer side-reactions can occur because the propagating polymer radicals can react with the solvent or with dead polymer chains or (occasionally) with unreacted monomer without causing propagation. In some cases, a chain transfer agent (denoted as T) is added to regulate (i.e. lower) the mean degree of polymerisation of the polymer chains. In this latter case, reinitiation can occur to generate a second polymer chain.[30]

A free radical polymerisation can be terminated by either combination or disproportionation. In the former case, the molecular weight of the final 'dead' (non-propagating) polymer is equal to the sum of the molecular weights of the two reacting polymer radicals. In the latter case, two 'dead' polymer chains are formed, with one of these chains containing an unsaturated chain-end (see Figure 6). Polymers prepared via free radical polymerisation typically exhibit broad molecular weight distributions (M_w/M_n > 2.0). This is partly owing to termination and partly because the rate of

initiation is relatively slow compared to chain transfer and propagation, so new chains continue to be formed even towards the end of the reaction (i.e. under monomer-starved conditions). Chain transfer side-reactions also tend to broaden the molecular weight distribution. Another well-known side-reaction involves the reaction of polymer radical with oxygen, which leads to the formation of an unreactive peroxy radical adduct. This is why free radical polymerisations have to be conducted in the absence of aerial oxygen to avoid unwanted retardation or inhibition.

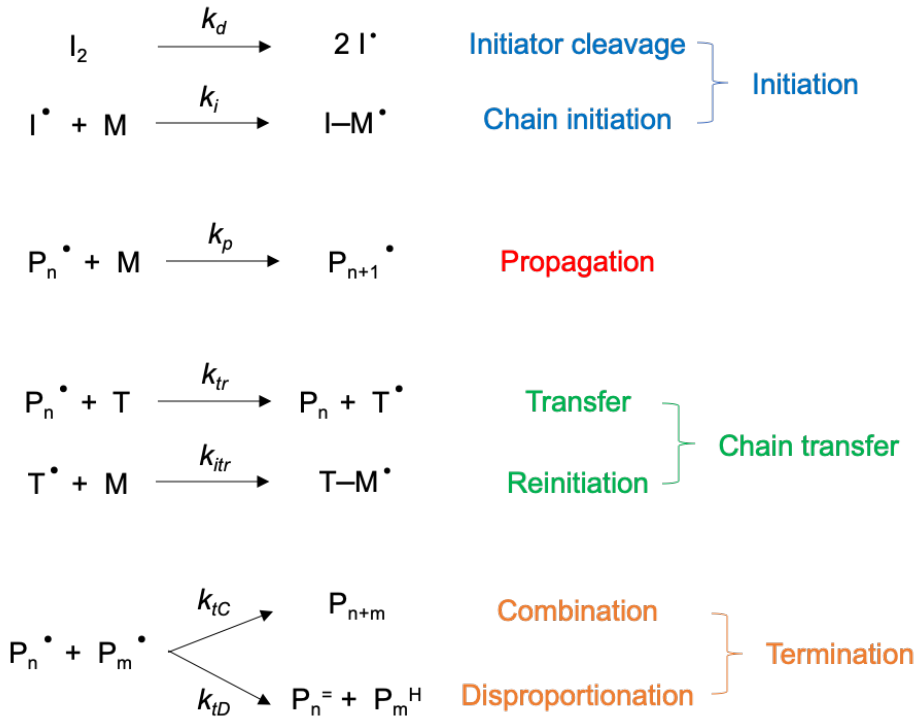

Figure 6. The generally accepted mechanism for free radical polymerisation, showing the four stages of initiation, propagation, chain transfer and termination.[23,31]

For unimolecular decomposition, the rate of formation of primary radicals via unimolecular decomposition of the initiator is given by Equation 4, in which $[I]$ is the initiator concentration, R_d is the rate of decomposition, and k_d is the rate constant for the initiator decomposition.

$$-\frac{d[I]}{dt} = R_d = k_d[I] \tag{4}$$

The rate of initiator decomposition is typically much slower than the rate of reaction of the monomer with the primary radical, which makes this the rate-determining step. Moreover, an initiator efficiency (*f*) must be introduced to allow for the fact that not all

of the primary radicals go on to generate polymer chains. The overall expression for initiation of a polymerisation is given by Equation 5.

$$\frac{d[I\text{–}M^{\cdot}]}{dt} = R_i = 2fk_d[I] \quad (5)$$

The monomer-initiator radical adduct can then react with further vinyl monomers to produce a propagating polymer radical ($P_n^{\bullet}$). The rate of propagation, R_p, is given by Equation 6, where k_p is the rate constant for propagation.

$$-\frac{d[M]}{dt} = R_p = k_p[M][P_n^{\cdot}] \quad (6)$$

As shown in Figure 6, termination can occur by either combination or disproportionation. These two reactions have differing rate constants, k_{tC} and k_{tD}. The final rate expressions for each case are given by Equations 7 and 8, respectively. The overall rate of termination can be expressed as shown in Equation 9, where the rate constant, k_t, is equal to the sum of these rate constants, $k_{tC} + k_{tD}$.

$$R_{tC} = k_{tC}[P_n^{\cdot}]^2 \quad (7)$$

$$R_{tD} = k_{tD}[P_n^{\cdot}]^2 \quad (8)$$

$$R_t = 2k_t[P_n^{\cdot}]^2 \quad (9)$$

Chain transfer can occur throughout the polymerisation, whereby the active radical centre is transferred from the growing polymer radical to a different species within the reaction mixture. The rate of chain transfer, R_{tr}, can be expressed as shown in Equation 10, where *T* denotes the species to which the radical centre is transferred and k_{tr} is the rate constant for the chain transfer.

$$R_{tr} = k_{tr}[P_n^{\cdot}][T] \quad (10)$$

To determine the overall rate expression for free radical polymerisation, the steady-state approximation is invoked. This approximation states that the rate of initiation equals the rate of termination, i.e. there is no net gain or loss in the concentration of radical species.[32] It is further assumed that chain transfer reactions are negligible. Thus, the overall rate equation only depends on the initiation, propagation and

termination steps of the polymerisation. The final expression for the rate of polymerisation, R_{polym} , is given by Equation 11:

$$R_{polym} = k_p[M]\sqrt{\frac{fk_d[I]}{k_t}} \qquad (11)$$

The main problem with free radical polymerisation is that it provides poor control over both the molecular weight distribution and the copolymer architecture.[33] In particular, it is not possible to prepare well-defined diblock copolymers. In the following sections, alternative polymerisation techniques are introduced that confer much better control over the molecular weight distribution and, more importantly, the copolymer architecture.

2.3 Living Anionic Polymerisation

Living anionic polymerisation was first reported by Szwarc in 1956.[34] The polymerisation is initiated by a carbanionic species and the polymerisation is termed 'living' because, unlike free radical polymerisation, there is no intrinsic termination step. Once all the monomer has been consumed, the carbanionic end-groups remain active and further chain growth can occur if a second monomer charge is added. This is because, unlike radicals, carbanions cannot react with each other. [35] There is also essentially no chain transfer during anionic polymerisation. Furthermore, the rate of propagation is significantly slower than the rate of initiation.[27,36] This means that all the polymer chains are formed immediately and there is no overlap between the initiation and propagation steps. This leads to very narrow molecular weight distributions (M_w/M_n < 1.10). As indicated in Figure 5, the molecular weight of such polymers increases linearly with monomer conversion.

In Szwarc's pioneering studies, styrene was polymerised in dry THF using a sodium-naphthalene complex as the initiator.[37] The initial styrene radicals dimerise to form a dianionic species, with electron transfer to styrene occurring during the initiation step. Subsequent propagation leads to polystyrene chains comprising two anionic end-groups. Szwarc noted that there was no colour change in the reaction mixture once all the styrene had been consumed. Moreover, subsequent monomer addition led to further polymer growth, thus confirming the so-called 'living' character of this polymerisation. Introducing water into the reaction solution led to immediate

termination because anionic polymerisations are highly intolerant towards protic impurities.

An example of a living anionic polymerisation is depicted in Figure 7. An organolithium complex, in this case *n*-butyl lithium, is used to initiate this polymerisation.[20] In principle, 4-substituted styrenes can be polymerised instead of styrene.[38] Other suitable vinyl monomers include isoprene, butadiene, 2-vinylpyridine and 4-vinylpyridine.[39]

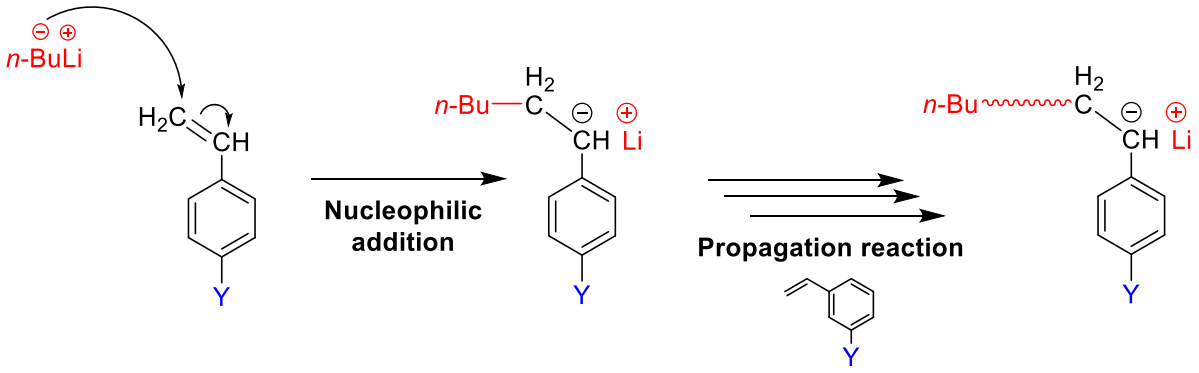

Figure 7. Reaction mechanism for the polymerisation of 4-substituted styrene monomers via living anionic polymerisation using *n*-BuLi as the initiator.[20]

The discovery of living anionic polymerisation was an important breakthrough. Firstly, this method affords precise control over the target molecular weight up to 10^6 g mol^{-1}, simply by adjusting the monomer/initiator molar ratio.[40] Secondly, the resulting polymers have remarkably narrow molecular weight distributions, with dispersities sometimes less than 1.05.[41] A Poisson distribution can be used to describe the molecular weight distribution.[35] Moreover, as there is no termination step and carbanions are highly reactive, sequential addition of a second monomer leads to the formation of well-defined diblock (or triblock) copolymers, which cannot be prepared using free radical polymerisation.[42] Finally, very high monomer conversions (> 99%) can be routinely achieved.

However, there are certain limitations to anionic polymerisation, which prevent its widespread industrial use. Firstly, anionic polymerisation is highly intolerant towards protic impurities such as water. Furthermore, many functional monomers containing hydroxyl, primary amine or carboxylic acid groups are incompatible with carbanions and so cannot be polymerised via living anionic polymerisation.[43] Indeed, rather few vinyl monomers are amenable to anionic polymerisation.

2.4 Reversible Deactivation Radical Polymerisation (RDRP)

Free radical polymerisation and living anionic polymerisation each possess various advantages and disadvantages. Free radical polymerisation is preferred for the industrial manufacture of viny polymers owing to its ease of implementation and tolerance of monomer functionality and protic sources.[24] However, it offers very limited control over the copolymer architecture, molecular weight and dispersity. In contrast, living anionic polymerisation offers precise control over the target molecular weight, produces a narrow molecular weight distribution and provides convenient access to complex architectures. Nevertheless, it is only applicable to a rather narrow subset of vinyl monomers and rather stringent reaction conditions are required to remove all traces of water. In principle, combining the positive attributes from these two techniques while minimising their limitations should enable the precise synthesis of functional vinyl polymers with well-defined architectures. This general approach is now known as Reversible Deactivation Radical Polymerisation (RDRP).

RDRP enables the synthesis of a wide range of functional polymers with pre-determined molecular weights, narrow dispersities and complex architectures.[44] The general principle for such polymerisations involves the suppression of termination relative to propagation. In principle, this can achieved either by rapid reversible deactivation of polymer radicals to produce dormant polymer chains (see Figure 8) or by rapid reversible chain transfer using highly efficient chain transfer agents (CTAs).[45]

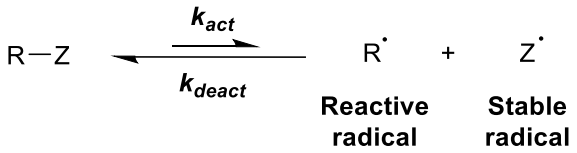

Figure 8. Generic reaction scheme for an RDRP equilibrium, with the dormant species shown on the left-hand side of the equilibrium and the active polymer radical species on the right-hand side.[20]

There are three main types of RDRP: nitroxide-mediated polymerisation (NMP), atom transfer radical polymerisation (ATRP) and reversible addition-fragmentation chain transfer (RAFT) polymerisation. All copolymers prepared in this Thesis were synthesised using RAFT polymerisation, which is discussed in more detail below.

2.5 Reversible Addition Fragmentation Chain Transfer (RAFT) Polymerisation

RAFT polymerisation was first reported in 1998 by Moad et al. and has subsequently revolutionised the field of polymer synthesis.[46] It enables the synthesis of complex copolymer architectures while providing good control over the molecular weight distribution. As shown in Figure 9, the molecular weight distribution of a polymer prepared by RAFT polymerisation is significantly narrower than that prepared by conventional free radical polymerisation. Moreover, RAFT polymerisation introduces functional end-groups that can be further modified.[47]

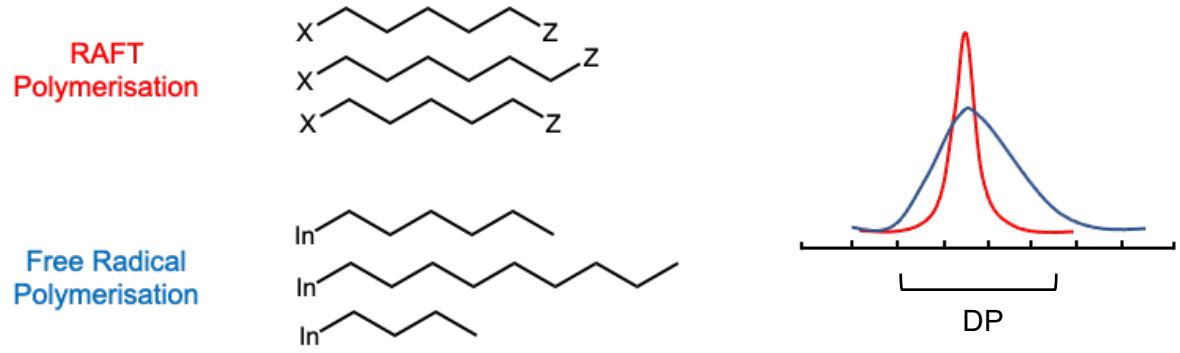

Figure 9. RAFT polymerisation produces near-monodisperse polymer chains of adjustable molecular weight. In contrast, free radical polymerisation provides much less control over both the molecular weight distribution and the target molecular weight. RAFT polymerisation also provides convenient access to complex copolymer architectures and introduces functional end-groups that can be used for further derivatisation.[48]

Over the past two decades or so, RAFT polymerisation has become widely recognised as one of the most versatile types of controlled living polymerisation.[49] This is in part because of its applicability to many vinyl monomers and reaction conditions.[50] It utilises an organosulfur chain-transfer agent (CTA) that mediates the polymerisation via rapid reversible chain transfer.[48 51] This rapid exchange of end-groups between the growing polymers is essential for achieving a narrow molecular weight distribution. The choice of the type of RAFT agent and its R and Z groups depends on the type of monomer being polymerised, as depicted in Figure 10. The S-R bond must be sufficiently weak to fragment rapidly to form the radical leaving group R$^{\bullet}$, preferably without undergoing any side reactions. The nucleophilic nature of the Z group ensures activation of the thiocarbonyl bond and also stabilises the intermediate radical adduct.[52]

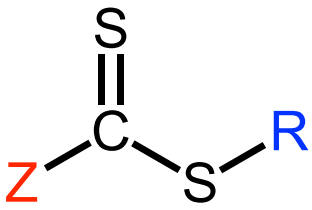

Figure 10. Generic structure of a RAFT chain transfer agent.

Figure 11 shows the chemical structures of the most commonly used RAFT agents, which are dithiobenzoates,[50] trithiocarbonates,[51,53] trithiocarbamates[54] and xanthates.[55] In each case, the organosulfur end-groups enable post-polymerisation modification reactions that can dictate potential applications for the resulting polymers.[56]

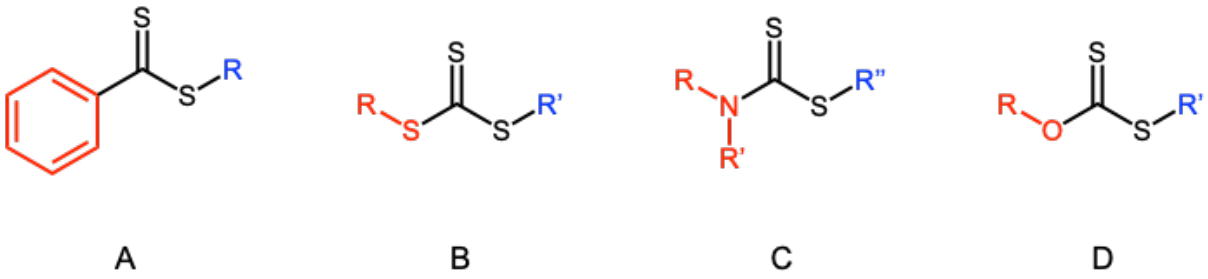

Figure 11. Chemical structures for four common RAFT agents: **A)** dithiobenzoate; **B)** trithiocarbonate; **C)** dithiocarbamate; **D)** xanthate.

Figure 12 illustrates the mechanism by which RAFT-mediated polymer chains are generated. In the initiation step, initiator radicals are formed by either thermal decomposition or light irradiation,[57] initiate a propagating polymer radical. This species reacts with the RAFT agent to afford a radical adduct. This then produces a radical leaving group, which then reacts with further monomer to initiate a new growing polymeric chain.[58] In the propagation step, the organosulfur chain-ends are shared equally between the growing polymer chains. Termination is suppressed relative to propagation but never eliminated; it proceeds by the same two mechanisms already discussed for conventional free radical polymerisation.

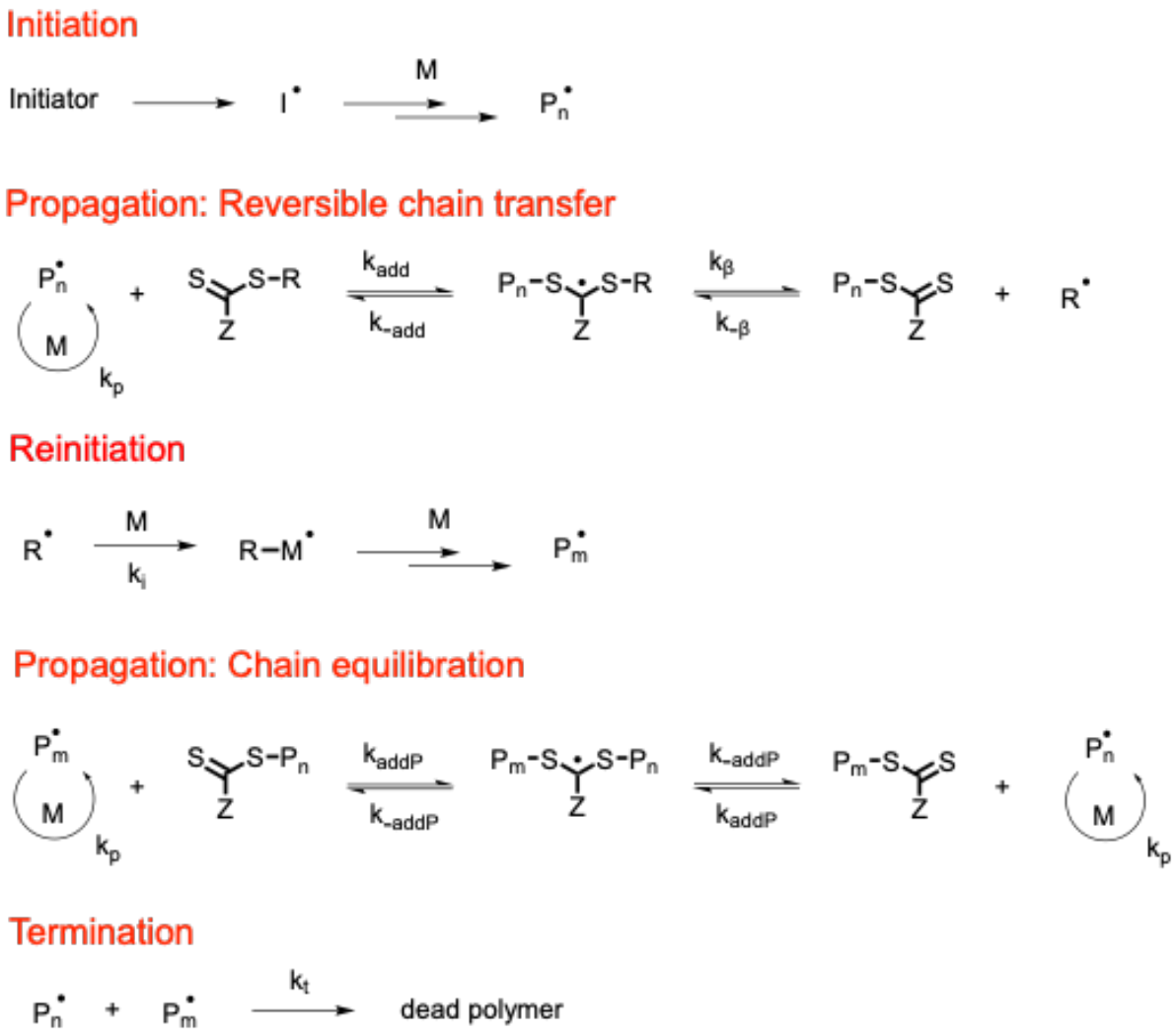

Figure 12. The RAFT polymerisation mechanism, which is composed of the following five main steps: (i) initiation which is the formation of radicals; (ii) propagation of the growing polymer chains; (iii) reinitiation, where the radical leaving group creates a new growing polymer radical; (iv) chain equilibration, where the organosulfur chain-ends are shared equally between the growing polymer chains; (v) termination, where two radicals react together and chain growth ceases.[59]

One of the main advantages of RAFT polymerisation is that it can be employed in polar solvents such as water and is applicable to many acrylates, methacrylates, acrylamides, methacrylamides, vinyl esters and styrene.[60] Moreover, the synthesis of functional diblock and triblock copolymers can be readily achieved without recourse to protecting group chemistry. Of particular relevance to this Thesis, amphiphilic diblock copolymers have attracted significant industrial and academic interest owing to their ability to self-assemble in aqueous solution to form various types of nano-objects.[61]

2.6 Emulsion Polymerisation

Emulsion polymerisation was originally developed for the production of synthetic latex rubber during World War II.[62] Because of its ease of implementation and flexible processing conditions, emulsion polymerisation is utilised for the industrial

manufacture of many vinyl polymers, such as paints, adhesives and paper coatings.[63–65] A typical emulsion polymerisation formulation involves a water-insoluble monomer, a water-soluble free radical initiator and a surfactant in water. The final product is a stable colloidal dispersion of microscopic polymer particles, otherwise known as a latex. Such polymerisations are environmentally friendly because they involve a cheap non-toxic solvent (water) and typically proceed to very high monomer conversion, so there is little waste and no volatile organic components (VOCs).

In his now seminal studies, Harkins outlined three distinct regimes for emulsion polymerisation: Intervals I, II and III.[66] As shown in Figure 13, Interval I usually occurs at 0–5% conversion and involves particle nucleation. The rate of polymerisation remains relatively constant during Interval II, which continues until all the monomer droplets have been consumed. The rate of polymerisation is reduced during Interval III, which proceeds until all the monomer has been consumed.

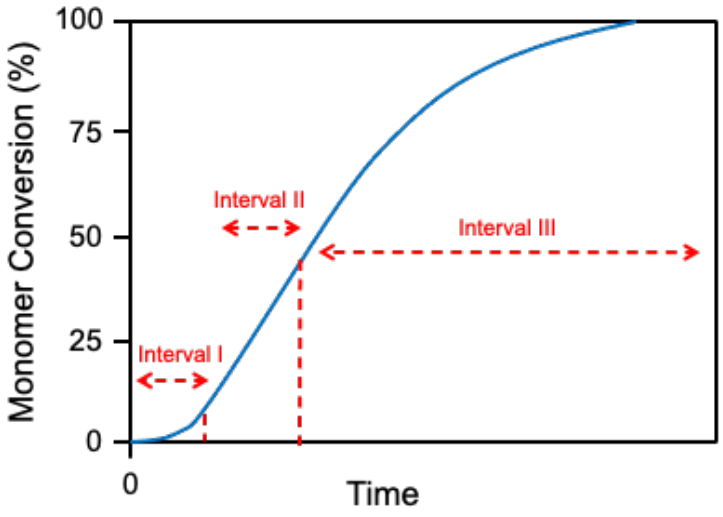

Figure 13. The three main stages (Intervals I, II and III) for an aqueous emulsion polymerisation.[67]

Figure 14 depicts a schematic representation of the three Intervals during an aqueous emulsion polymerisation. Micron-sized monomer droplets are formed and remain present during Interval I; this oil-in-water emulsion is stabilised by adsorbed surfactant molecules. The water-soluble free radical initiator slowly decomposes to generate radicals in the aqueous phase. Although the vinyl monomer is water-immiscible, it nevertheless exhibits some limited solubility (typically 0.1 to 5 g dm^{-3}) in the aqueous continuous phase. This small fraction of monomer reacts with the initiator radicals to form oligomeric radicals. As these oligomers grow beyond a critical chain length, they

become more hydrophobic, which leads to either heterogeneous or homogeneous nucleation.[68] In the former case, oligomeric radicals are transferred into the surfactant micelles located in the aqueous phase.[69] In contrast, homogeneous nucleation occurs when free surfactant adsorbs onto the oligomeric radicals to form new micelles.[70] Interval I is complete when all micelles are converted into nascent growing particles.

Interval II is characterised by the growth of monomer-swollen particles. During this period the number of particles does not change but the existing particles grow larger (see Figure 14).[67] One significant difference between Intervals II and III is the fact that the monomer droplets act as reservoirs, which results in a constant rate of polymerisation.[71]

Interval III is characterised by a rate reduction under monomer-starved conditions. There are no monomer droplets left during this final stage, only monomer-swollen colloidally stable latex particles. The final monomer conversion is very high (>99%).

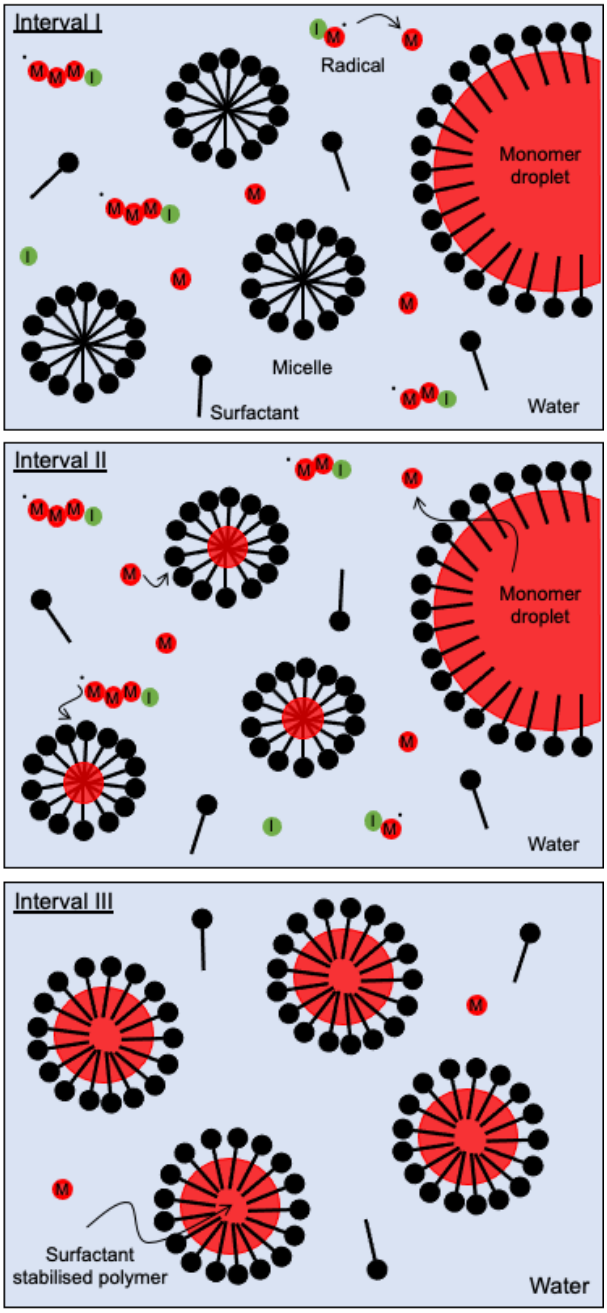

Figure 14. Schematic representation of the three Intervals that constitute a conventional emulsion polymerisation.[72,73]

Surfactant-free RAFT aqueous emulsion polymerisation has been developed over the past two decades.[74] This formulation will be discussed in more detail in section 2.7.4.

2.7 Self-Assembly

It is well-known that amphiphilic molecules such as surfactants or block copolymers self-assemble to form nanoparticles in aqueous media.[75] A very common, naturally occurring example of such a surfactant is a lipid. These typically consist of two long hydrophobic chains and a zwitterionic head-group; they form bilayers in order to

minimise energetically unfavourable hydrophobic interactions (this is known as the hydrophobic effect).[76] There are various definitions of self-assembly, but in this Thesis it refers to the process in which a disordered system spontaneously forms an organised structure without external intervention.[77]

2.7.1 Surfactant self-assembly

As briefly mentioned above, surfactants are amphiphilic molecules that are composed of a hydrophilic (water-loving) head-group and a long hydrophobic (water-repelling) tail, which typically comprises a hydrocarbon chain. These compounds are widely used in industry due to their ability to reduce surface tension and stabilise emulsions, which is useful in home and personal care applications.[78] Surfactants are classified according to the nature of their hydrophilic head-group: they can be neutral, anionic, cationic or zwitterionic.

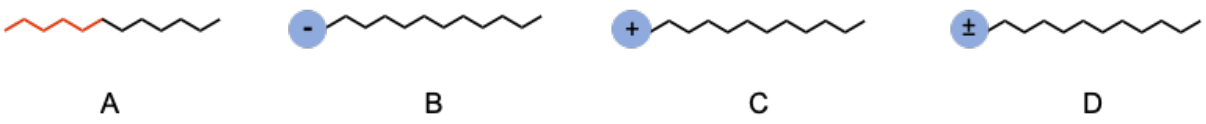

Figure 15. Schematic cartoon to illustrate: (A) neutral, (B) anionic, (C) cationic and (D) zwitterionic surfactant structures.

Surfactant self-assembly to form micelles is a thermodynamically-driven phenomenon, for which the driving force is the minimisation of unfavourable interactions of the hydrophobic tails with water. Various intermolecular forces can be involved, including H-bonding, electrostatics and van der Waals interactions.[79] Solution conditions such as the surfactant concentration, pH and temperature dictate the aggregate size and morphology.[80] The latter can be predicted using equation 12, which was introduced by Israelachvili and co-workers in 1976. Here C_{pp} is the critical packing parameter, V_0 denotes the volume occupied by the hydrocarbon chains, l_c is the length of those chains and a_0 is the surface area occupied by the hydrophilic head-group.[79,81]

$$C_{pp} = \frac{V_0}{a_0 l_c} \qquad (12)$$

The most commonly observed morphologies are presented in Figure 16 below, along with their associated numerical C_{pp} values.

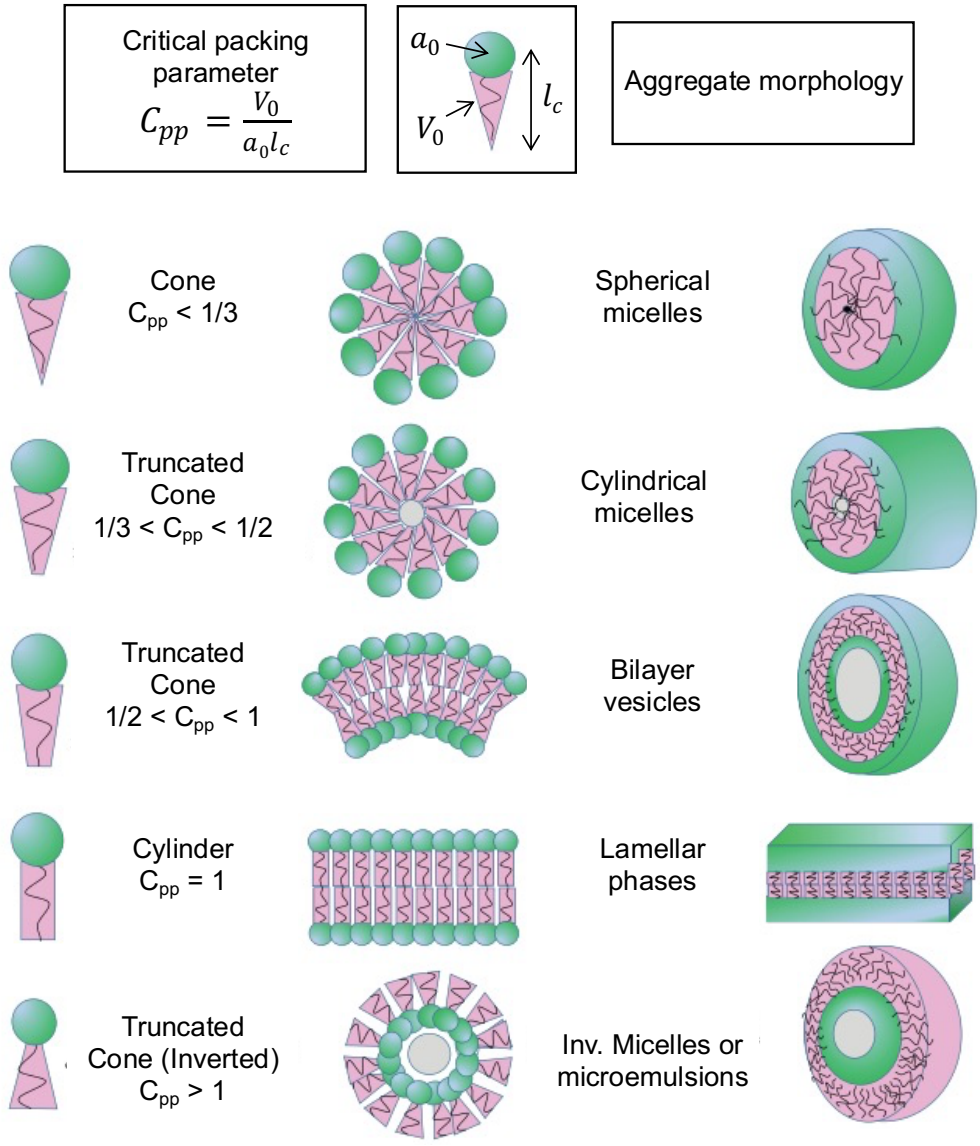

Figure 16. Schematic representation of surfactant self-assembly morphologies with their associated critical packing parameters.[80]

2.7.2 Block copolymer self-assembly

In the late 1950s, the invention of living anionic polymerisation by Szwarc et al. enabled the synthesis of well-defined diblock copolymer chains that underwent self-assembly in selective solvents.[82,83] The self-assembly behavior of such chains can easily be compared to that of surfactants. In AB type of diblock copolymers, one block is hydrophilic and the other is hydrophobic, hence the ratio of thereof determines their final morphology. Figure 17 below illustrates the accessible nanoparticle shapes; spheres, rods (also known as worm-like micelles), bilayers (lamellae and vesicles), hexagonally packed hollow hoops (HHH) and lastly large compound micelles.[84,85]

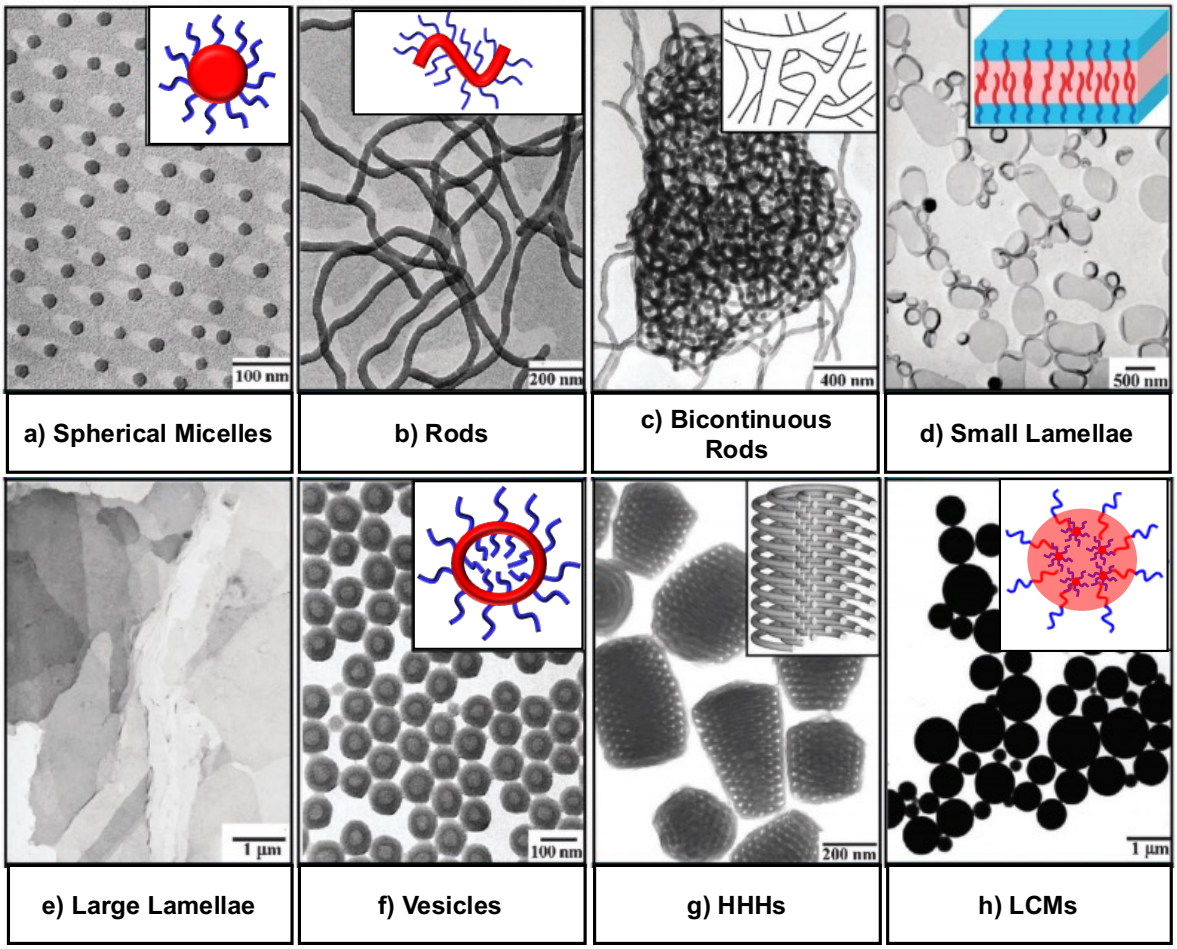

Figure 17. Transmission electron microscopy (TEM) images and schematic cartoons of the various morphologies that can be formed from amphiphilic PS_x-PAA_y diblock copolymers.[84,85]

Self-assembly in solution was traditionally achieved by employing either a pH switch or by the slow addition of a selective solvent to render one of the two blocks insoluble.[86] However, such post-polymerisation processing is typically restricted to dilute copolymer solutions (< 1% w/v). This limitation has severe implications in terms of scalability, which is a major issue for industrial applications.[87]

2.7.3 Polymerisation-Induced Self-Assembly (PISA)

PISA enables the *in situ* self-assembly of diblock copolymers to produce nano-objects with various morphologies. Typically, a soluble homopolymer precursor in a suitable solvent is chain-extended using an appropriate monomer such that the growing second block becomes insoluble at some critical DP.[61] This drives *in situ* self-assembly to produce various types of sterically-stabilised diblock copolymer nanoparticles. Figure 18 illustrates this process and also indicates the main three morphologies that can be obtained: spheres, worms or vesicles. The final copolymer morphology depends mainly on the relative volume fraction of each block, with relatively long

insoluble blocks favouring the formation of vesicles. However, various other parameters such as the copolymer concentration and the presence of ionic charge can also play important roles in this regard: it is well-known that many PISA formulations are restricted to kinetically-trapped spheres.[88]

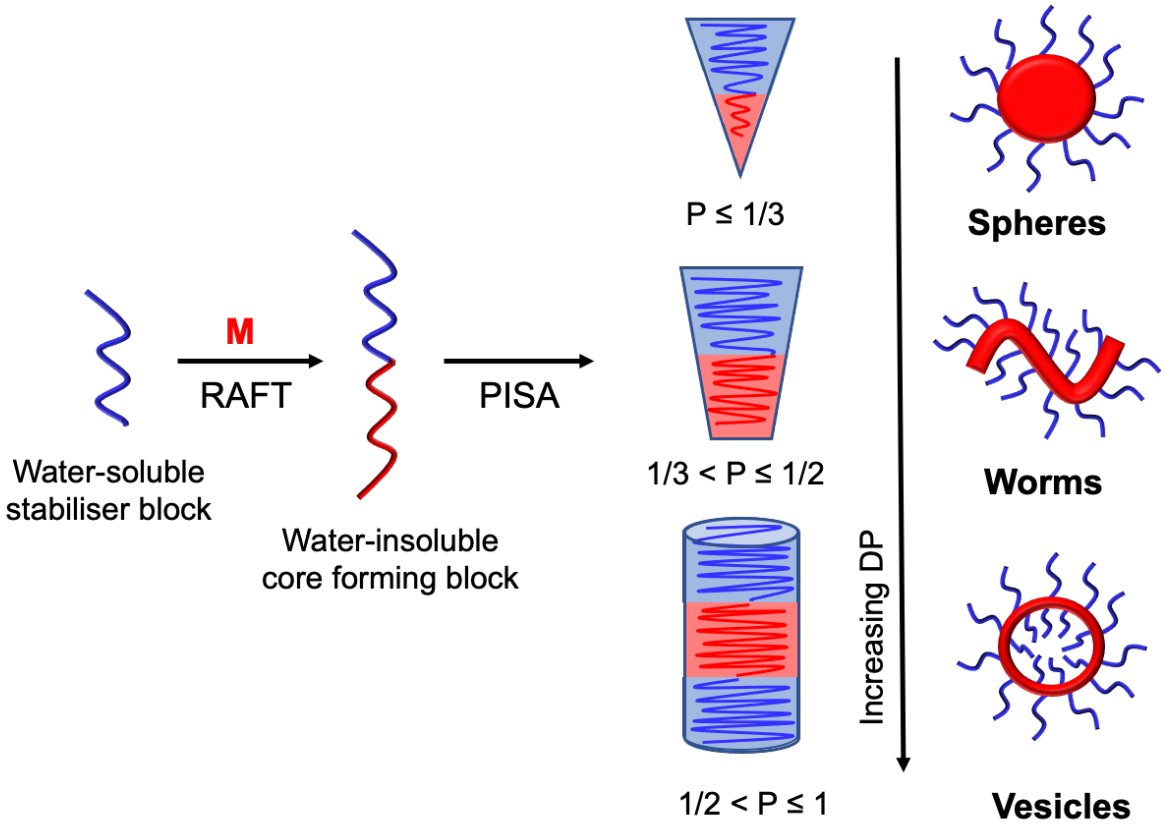

Figure 18. Schematic representation of the nanoparticle synthesis and morphologies using PISA. P denotes the packing parameter.[89]

The Armes group has constructed pseudo-phase diagrams for various PISA formulations that enable reliable PISA syntheses of the desired copolymer morphology.[90–92] Typically, the DP of the insoluble block is plotted against the copolymer concentration for a given (fixed) steric stabiliser DP.[93] However, in some cases the DP of each block can be plotted with all PISA syntheses being conducted at the same copolymer concentration.[94]

PISA syntheses have been conducted using various types of controlled radical polymerisation such as Nitroxide-Mediated Polymerisation[95–97] and Atom Transfer Radical Polymerisation (ATRP).[98–100] However, RAFT-mediated PISA remains the most commonly used technique reported in the literature.[101–110] This chemistry is applicable to a wide range of functional vinyl monomers under relatively mild

conditions.[111] Moreover, RAFT polymerisations can be conducted in a many different solvents, including water,[61,101,112] polar and non-polar solvents,[107,113–123] and even ionic liquids.[124] Importantly, RAFT-mediated PISA can be used to produce nanoparticles in the form of concentrated dispersions (i.e. 25–50% w/w).[61,113,116,125]

The versatility of the RAFT-mediated PISA approach makes it very suitable for many industrial applications. A wide range of solvents and materials can be used to achieve many nano-object morphologies in a relatively high solid concentration.

According to Hayward and Pochan, various parameters can dictate the final morphology of self-assembled diblock copolymer nano-objects.[126] When employing a polyelectrolytic steric stabiliser, it is well-known that strong electrostatic repulsion between neighbouring stabiliser chains prevents the evolution of copolymer morphology during PISA.[127] More specifically, Semsarilar et al. examined the synthesis of poly(potassium 3-sulfopropyl methacrylate)$_x$–poly(2-hydroxypropyl methacrylate)$_y$ (PKSPMA$_x$–PHPMA$_y$) diblock copolymer nanoparticles and found that the strongly anionic nature of the PKSPMA block led to kinetically-trapped spherical nanoparticles ranging from 50 to 200 nm (as illustrated in Figure 19 below).[127]

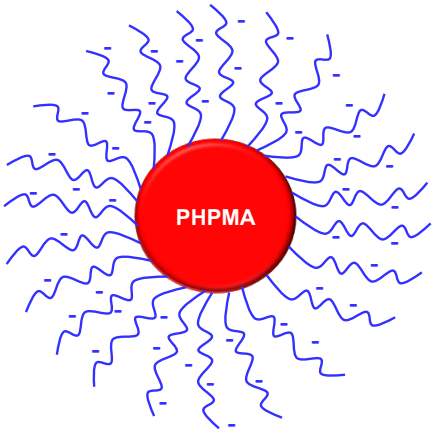

Figure 19. Schematic cartoon depicting PKSPMA$_x$ – PHPMA$_y$ spherical nanoparticles prepared by RAFT aqueous dispersion polymerisation.[127]

Given the anionic nature of the steric stabiliser block, only spherical nanoparticles could be obtained via RAFT aqueous dispersion polymerisation. However, this kinetically-trapped morphology is actually an advantage for industrial scale because it ensures that a relatively low dispersion viscosity can be maintained. Moreover, the copolymer morphology is irrelevant for this particular application because the initial spherical nanoparticles undergo *in situ* dissociation to form amphiphilic diblock copolymer chains (see later).

2.7.4 PISA by RAFT aqueous emulsion polymerisation

As described in Section 2.5, RAFT polymerisation enables the synthesis of various copolymer architectures with good control over the molecular weight distribution. However, unexpected problems were encountered for prototypical PISA formulations based on RAFT aqueous emulsion polymerisation, including (i) poor control over the

polymerisation resulting in broad molecular weight distributions,[110] (ii) slow polymerisation kinetics and incomplete conversion[128] and (iii) poor colloidal stability.[129]

Ferguson et al. developed the first really successful surfactant-free RAFT aqueous emulsion polymerisation formulation.[130,131] An amphiphilic RAFT agent was used to polymerise acrylic acid (AA) to produce a water-soluble precursor. Then a water-insoluble monomer, *n*-butyl acrylate (BA), was slowly added to the reaction mixture. When the hydrophobic block reaches a certain critical DP, micellar nucleation occurs.[130] These micelles become swollen with BA monomer, which allows the emulsion polymerisation to proceed efficiently. Figure 20 illustrates the mechanism of RAFT aqueous emulsion polymerisation. Gavena et al. extended this method by adding an second hydrophobic monomer and thus preparing well-defined triblock copolymers in the form of sterically-stabilised nanoparticles.[129]

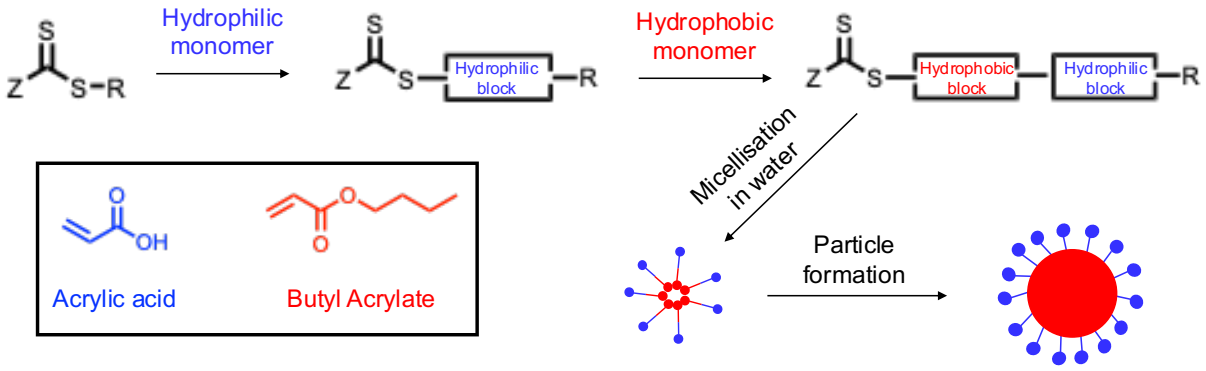

Figure 20. Particle formation process via ab initio RAFT aqueous emulsion polymerisation.[131]

RAFT aqueous emulsion polymerisation is a versatile technique that is applicable to many water-immiscible vinyl monomers. Charleux and co-workers have published a series of papers using various steric stabiliser blocks based on acrylic acid,[112,132] methacrylic acid,[133,134] acrylamides[135] and ethylene oxide.[136,137] A range of hydrophobic blocks have also been studied, such as methyl methacrylate,[138] styrene[134,138] and benzyl methacrylate[139,140]. More recently, many more specialty monomers have been examined, such as butyl acrylate,[135] vinyl acetate,[141] trifluoroethyl methacrylate,[142] isopropylideneglycerol methacrylate,[143] 2-methoxyethyl methacrylate[144] and glycerol monomethacrylate,[145] which demonstrates the structural diversity that is compatible with RAFT aqueous emulsion polymerisation. Such polymerisations often require optimisation in terms of the solution pH.[146,147] For

example, Chaduc et al. examined the effect of pH on the RAFT aqueous emulsion polymerisation of styrene using a PAA steric stabiliser.[147] In this case, the solution pH was systematically varied from highly acid (pH 2.5) to weakly basic (pH 8.1). At low pH, well-defined spherical nanoparticles were formed, whereas at high pH only poor control over the polymerisation was obtained (see Figure 21). Presumably, this was the result of partial hydrolysis of the RAFT end-groups.[148,149]

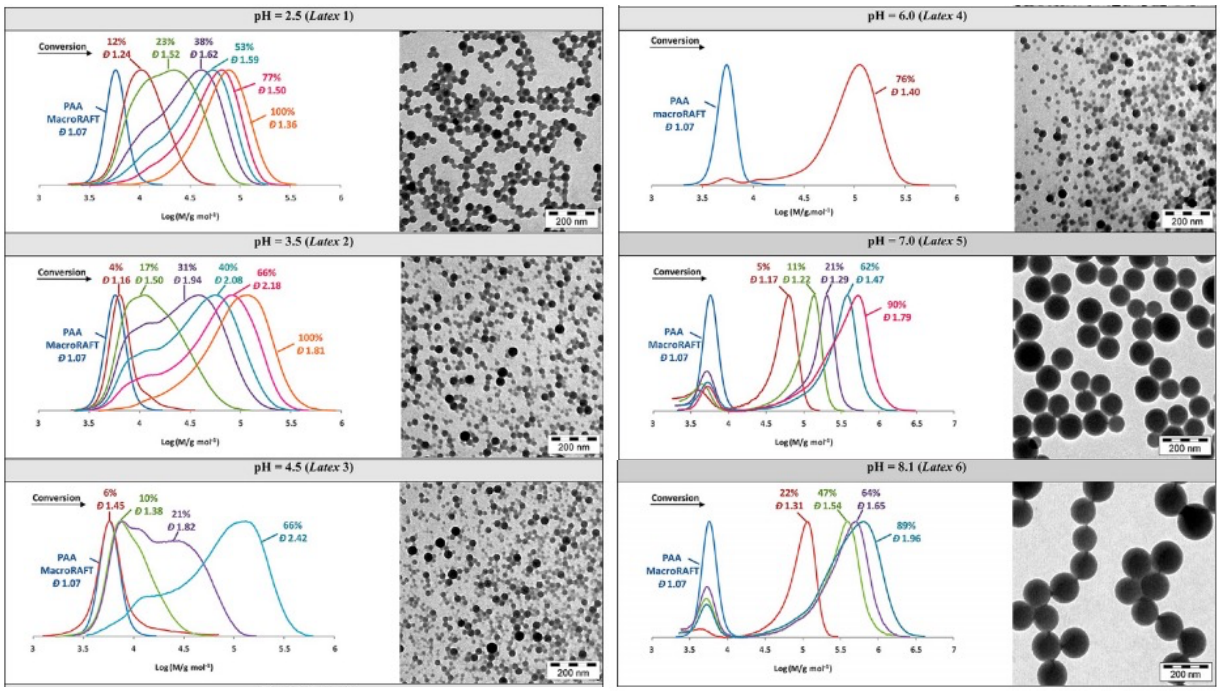

Figure 21. Effect of varying the solution pH on the evolution of molecular weight distribution with monomer conversion as determined by GPC analysis. For each PISA formulation, TEM studies of the final nanoparticles reveal a spherical morphology.[147]

In many cases RAFT aqueous emulsion polymerisation produces only kinetically-trapped spheres.[134,135,139,141–143,145] However, Boissé et al. reported that block copolymer worms and vesicles can also be accessed using such PISA formulations.[112] In this seminal study, a series of steric stabilisers were prepared by statistically copolymerising varying amounts of acrylic acid (AA) with poly(ethylene glycol) methyl ether acrylate (PEGA) using 2-(dodecylthiocarbonothioylthio)-2-methylpropanoic acid (TTC) as the RAFT agent. These water-soluble P(AA-co-PEGA) precursors were then chain-extended with styrene to produce spheres, worms or vesicles depending on the chemical composition of the stabiliser block. As shown in Figure 22, using a PAA-TTC stabiliser only produced spheres, whereas P(AA-co-PEGA)-TTC enabled the formation of worms. Finally, vesicles were observed when using a non-ionic PPEGA-TCC stabiliser.

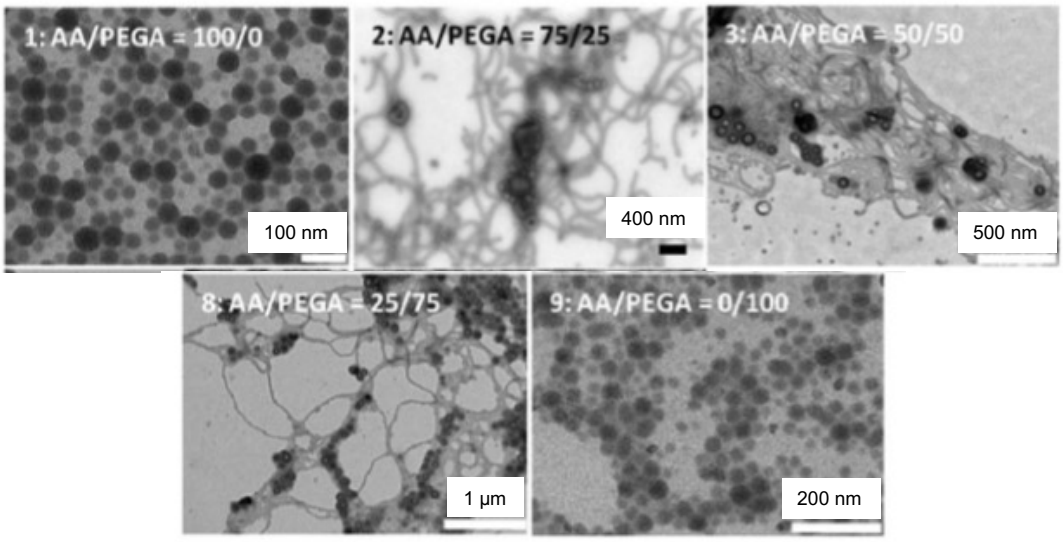

Figure 22. TEM images recorded for various P(AA-co-EGA)-PS morphologies obtained via RAFT aqueous emulsion polymerisation using statistical copolymers comprising AA and PEGA as the steric stabiliser block.[112]

The effect of varying the pH and salt concentration were also examined when using a steric stabiliser block comprising 50 mol% AA. The AA repeat units became increasingly ionised at higher pH, which led to a morphological transition from mainly worms to predominantly spheres. The addition of salt at pH 8 induced a morphological transition from spheres to worms or even vesicles. The same French group obtained similar results when using steric stabilisers comprising methacrylic acid (MAA) and poly(ethylene glycol) methyl ether methacrylate (PEGMA).[150–152]

In summary, although worms and vesicles can be accessed via certain RAFT aqueous emulsion polymerisation formulations, kinetically-trapped spheres are typically obtained when employing anionic steric stabiliser blocks such as poly(methacrylic acid) or poly(acrylic acid).[146]

2.8 Diblock copolymer stabilised oil-in-water nanoemulsions

Emulsions comprise a mixture of two (or more) immiscible liquids in which one liquid (the dispersed phase) is dispersed in another liquid (the continuous phase) in the form of droplets. Usually, one of the two liquids is water. There are two main types of emulsions, oil-in-water (O/W) and water-in-oil (W/O).[153] Emulsions are classified according to their droplet size, as well as their thermodynamic and kinetic stability. Macroemulsions comprise droplets that range in size from 1 to 1000 µm. Typically, high-shear homogenisation is required to produce such droplets, which may be kinetically stable but are never thermodynamically stable. If high-pressure

microfluidization is used to further process these micrometer sized droplets – and there is sufficient excess emulsifier – then a nanoemulsion is obtained. Nanoemulsions comprise droplets of 200-500 nm diameter and are also thermodynamically unstable. In contrast, microemulsions are composed of very fine droplets in the 10-100 nm range: they exhibit thermodynamic stability, tend to have narrower droplet size distributions and hence can be formed spontaneously in the absence of any shear.[154] Figure 23 illustrates the relative size ranges for a macroemulsion, a nanoemulsion and a microemulsion, respectively.

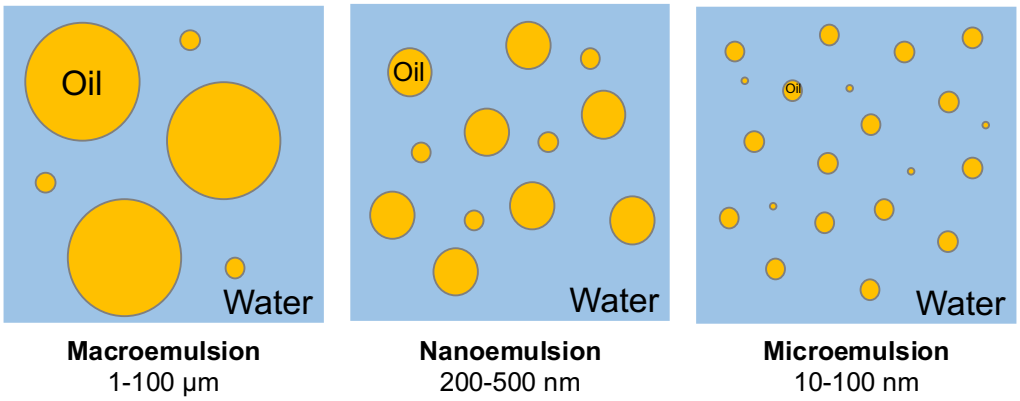

Figure 23. Illustration of the difference in size between a macroemulsion, a nanoemulsion and a microemulsion.[155]

The main destabilisation mechanisms[156] for emulsions are: i) droplet coalescence; (ii) aggregation, where multiple droplets stick together; (iii) sedimentation or creaming, where the dispersed phase either sediments or creams owing to gravitational forces (if there is a sufficiently large density difference between the two immiscible liquids); (iv) Ostwald ripening, which is the gradual diffusion of liquid from smaller droplets into larger droplets driven by the pressure difference.[154] Figure 24 summarises these four destabilisation mechanisms.

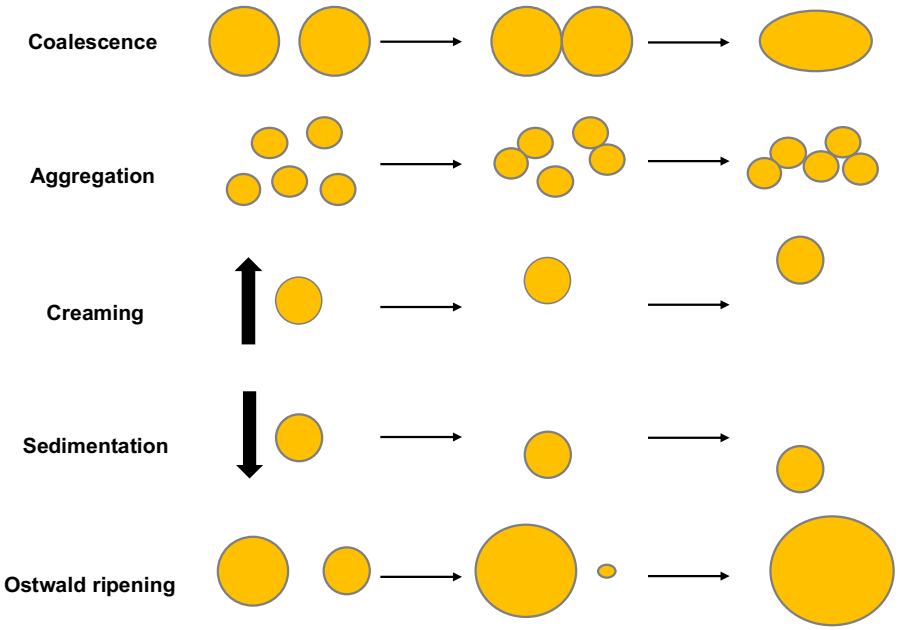

Figure 24. Schematic representation of the four main destabilisation mechanisms for emulsions.

Droplet coalescence tends to be the main reason for destabilisation in relatively unstable emulsions, whereas Ostwald ripening and either creaming or sedimentation tend to occur for more stable emulsions. Emulsifiers are used to prepare emulsions. They can be surfactants, amphiphilic copolymers or proteins, or colloidal particles.[157] Soluble emulsifiers are typically amphiphilic: for example, a surfactant comprising a hydrophilic head-group and one or more hydrophobic chains.[158] Adsorption of such molecules at the oil-water interface lowers the oil/water interfacial tension, which aids droplet formation and stabilisation.

As discussed in Sections 2.1 and 2.2, RAFT-mediated PISA enables the convenient synthesis of functional diblock copolymers in the form of sterically-stabilised nanoparticles.[61,86,159–166] The amphiphilic nature of some of these copolymer chains allows them to act as polymeric surfactants and hence stabilise either o/w emulsions or w/o emulsions, depending on the diblock composition.[167] Initially, the nanoparticles are dispersed in either the aqueous phase or the oil phase. High-shear homogenisation generates micron-sized droplets, which are stabilised by the adsorption of the diblock copolymer nanoparticles at the oil-water interface. Here the hydrophilic stabiliser block interacts with the aqueous phase and the hydrophobic core-forming block interacts with the oil phase. In order to form a nanoemulsion, high-pressure microfluidization is required to generate additional oil-water interface and excess nanoparticles must be present to adsorb at this fresh interface. If the original

diblock copolymer nanoparticles remain intact, a Pickering nanoemulsion is obtained.[157] However, it is also known that the diblock copolymer nanoparticles can undergo *in situ* dissociation under such conditions to produce molecularly-dissolved copolymer chains, which then act as a soluble emulsifier.[11]

These amphiphilic diblock copolymer chains not only stabilise nanoemulsions - they can also be designed to interact with growing inorganic crystals.[168] The prerequisite here is that the steric stabiliser chains should possess anionic character.[169]

2.9 Biomineralisation and incorporation of guest species

Living organisms are widely known for constructing complex, tailor-made organic-inorganic hybrid materials for specific functions that vary considerably in terms of their composition, morphology and mechanical properties.[170] In this context, the most abundant naturally occurring mineral is calcium carbonate or $CaCO_3$. It is primarily produced by marine organisms such as sea urchins, molluscs, sponges, corals and crustaceans.[170] Although the aforementioned organisms each produce $CaCO_3$-based composite materials, they are used for different purposes. For example, they can offer structural support and protection (in some cases an organism's entire exostructure can be made up of $CaCO_3$-based materials), or provide remarkable mechanical strength.[171] There are three main anhydrous crystalline polymorphs of $CaCO_3$: calcite, vaterite and aragonite. Figure 25 below illustrates these three structures, with calcite being the most commonly formed owing to its higher thermodynamic stability under ambient conditions.[172]

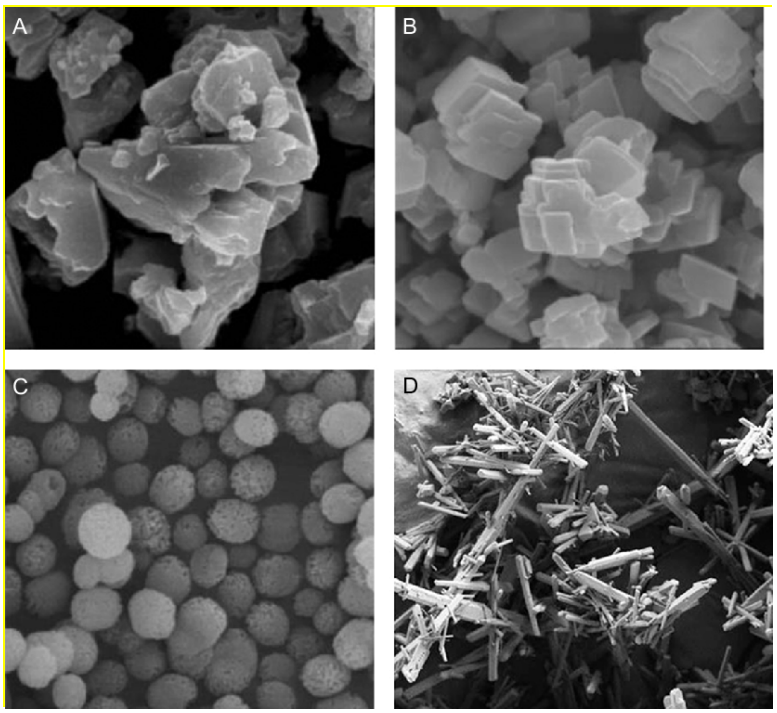

Figure 25. The four main polymorphs of $CaCO_3$: (A) amorphous calcite; (B) rhombohedral and/or layered calcite; (C) spherical vaterite; D) needle aragonite.[173]

Depending on its specific function, biogenic calcite is normally produced in the form of single crystals that can vary in size from micrometers up to millimetres. For a crystal to be suitable for use as a skeletal material, it must be hard and durable without being brittle. Pure calcite is very brittle along its {10.4} plane, so it is an unsuitable skeletal material.[174] Certain organisms have evolved to tackle this limitation by occluding proteins within calcite crystals, particularly in the planes where cracks would be likely to propagate.[175] Figure 26 below provides an illustration of the calcite unit cell. Proteins are primarily occluded parallel to the c-axis as part of an effective crack suppression mechanism.

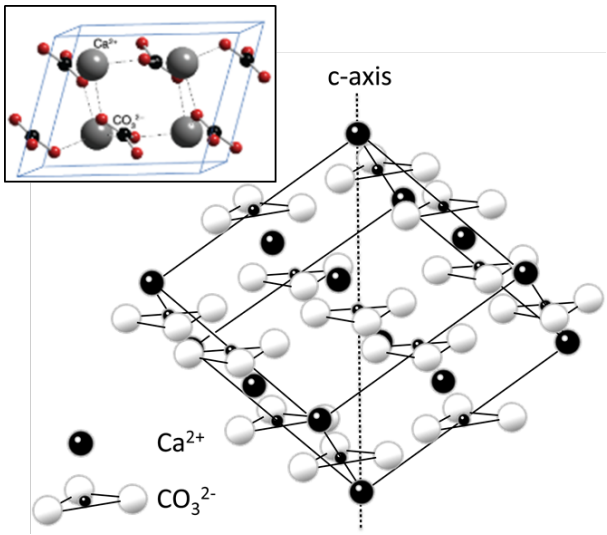

Figure 26. Hexagonal unit cell and c-axis configuration for crystalline calcite.[176]

As a result of introducing anisotropic fracture behaviour into this material, its propensity towards embrittlement is significantly reduced. Such protein occlusion by naturally-occurring organisms has inspired various synthetic studies focused on the fabrication of inorganic-organic hybrid materials.[169,177,178] The aim here is to be able to enhance the mechanical properties of the final crystals for a wide range of applications.

Since there are many naturally-occurring inorganic crystals, there has been considerable interest in the occlusion of guest species within such biocompatible inorganic hosts. A significant body of work is concerned with the occlusion of nanoparticles. For example, in 2005 Lu et al. prepared porous calcite crystals using copolymer latex particles as templates: in this case, the copolymer chains comprised styrene (St), methyl methacrylate (MMA) and acrylic acid (AA) in various proportions.[177] This Chinese team investigated the effect of various functional groups on the surface of the latex particles, the latex and calcium concentrations and the solution temperature on the crystal morphology and latex loading. Rhombohedral crystals with uniform porosity could be obtained and the pore size could be adjusted by varying the latex particle diameter. A three-stage crystallisation mechanism was suggested: (i) nucleation of $CaCO_3$ nanocrystals onto the latex particles; (ii) intermediate crystal growth and (iii) calcite occlusion of the latex particles. In order to obtain porous calcite crystals, the latex was removed either via dissolution in tetrahydrofuran (THF) or by calcination at 500°C. Figure 27 shows four SEM images obtained for such calcite-latex composite materials.

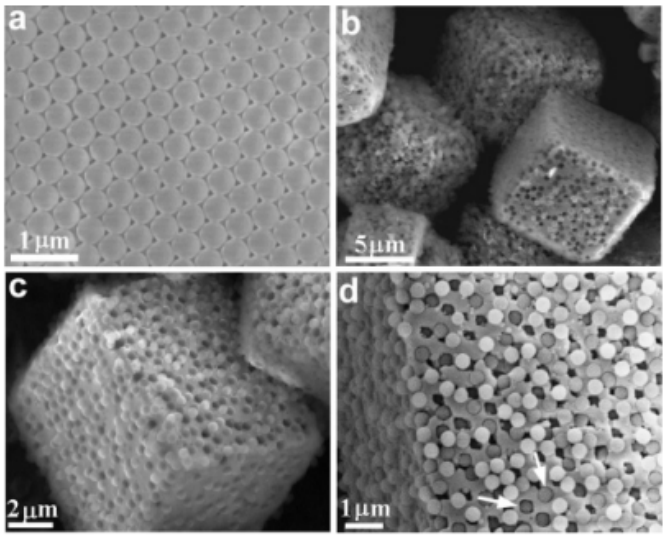

Figure 27. a) P(St-MMA-AA) latex particles via SEM imaging, **b-d)** SEM images of the composite material of latex-calcite.[167]

Latexes comprising various functional surface groups, including phosphates, sulfates, carboxylates, and ammonium cations, were examined. Empirically, it was found that surface-carboxylated latex particles produced the highest extents of occlusion and gave the most promising composite material. Moreover, employing high concentrations of either the latex particles and/or calcium ions yielded non-rhombohedral crystals, as depicted in Figure 27. Conducting occlusion experiments at lower temperatures also slightly affected the crystal morphology, but primarily this led to surface occlusion as opposed to uniform occlusion. This could be related to the slower rate of crystallisation under such mild conditions. This early study provided some useful insights with regard to the design of inorganic-organic nanocomposites with complex morphologies and provided a new perspective on biomineralisation.

More recently, Ning et al. studied the effect of varying the anionic surface density of the stabiliser block on the occlusion of sterically-stabilised diblock copolymer nanoparticles within calcite crystals.[169] Poly(ammonium 2-sulfatoethyl methacrylate)-poly(benzyl methacrylate) [PSEM–PBzMA] nanoparticles were prepared via RAFT-mediated PISA. Importantly, the surface density of the PSEM stabiliser chains could be varied simply by using either RAFT alcoholic dispersion polymerisation (high surface density) or RAFT aqueous emulsion polymerisation (low surface density), respectively. Figure 28 illustrates the two reaction schemes used to synthesise such PSEM-PBzMA nanoparticles. A schematic representation of the resulting nanoparticle morphologies is also shown for clarity. The ‘high surface density’ nanoparticles had a relatively high aggregation number of 224 whereas the ‘low surface density’ nanoparticles had a much smaller aggregation number of 40 for identical diblock copolymer compositions. This difference is a consequence of the polarity of the continuous phase: the more polar aqueous phase leads to greater electrostatic

repulsion between neighbouring anionic PSEM blocks, which inevitably leads to a significantly low aggregation number (and surface density of PSEM chains) when using RAFT aqueous emulsion polymerisation.

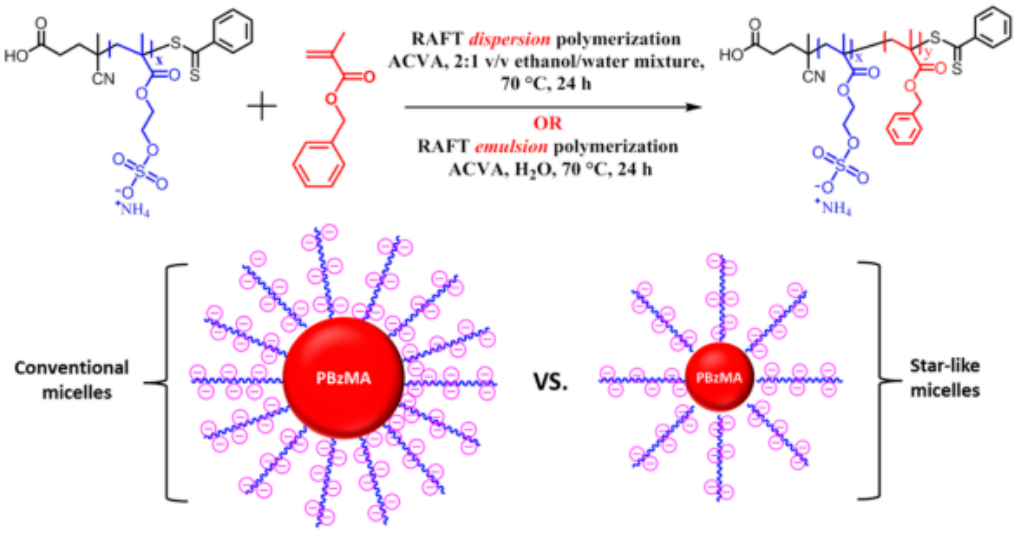

Figure 28. Schematic illustration of the differing PSEM-PBzMA diblock copolymer nanoparticles formed via RAFT alcoholic dispersion polymerisation and RAFT aqueous emulsion polymerisation, respectively.[169]

The aim of this study was to understand the synthesis parameters that influence the extent of occlusion in order to maximise the organic content of the final synthetic hybrid crystal. Ning et al. found that negligible nanoparticle occlusion occurred when employing PSEM-PBzMA nanoparticles prepared via RAFT alcoholic dispersion polymerisation. In contrast, TGA studies indicated more than 7% occlusion by mass could be achieved when using the nanoparticles prepared via RAFT aqueous emulsion polymerisation. Thus, perhaps counter-intuitively, greater occlusion was achieved when using nanoparticles bearing a lower surface density of sulfate groups for calcium ion binding. Ning et al. hypothesised that the lower surface density of PSEM chains enabled different interactions between the anionic nanoparticles and the growing crystal surface, see Figure 29.

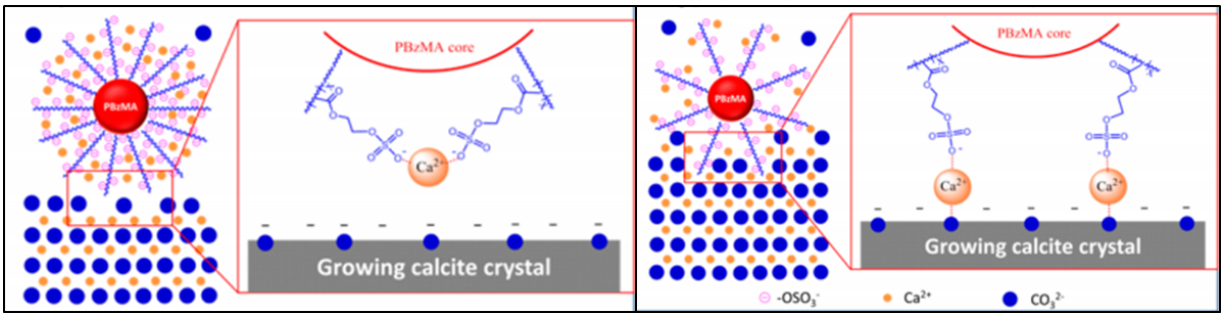

Figure 29. LHS: High anionic surface density PSEM-PBzMA nanoparticles formed via RAFT dispersion polymerisation and the intermolecular binding via the divalent calcium ions. RHS: Low anionic surface density PSEM-PBzMA nanoparticles formed via RAFT emulsion polymerisation and the binding of the sulfate group to the crystal surface via the divalent calcium ions.[169]

Similarly, Douverne et al. systematically varied the composition of well-defined anionic statistical copolymers in order to tune the anionic charge density of the steric stabiliser block and study how this affected the extent of nanoparticle occlusion within calcite crystals.[168] In this case, anionic 2-(phosphonooxy)ethyl methacrylate (POEMA) was statistically copolymerised with non-ionic glycerol monomethacrylate (GMA) to produce the steric stabiliser chains, while targeting a constant DP of 300 for the core-forming PBzMA block, see Figure 30.

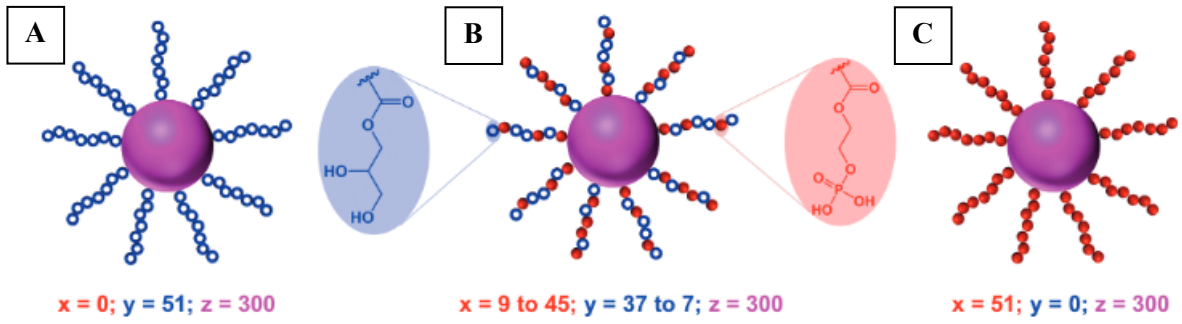

Figure 30. (A) purely non-ionic PGMA stabilizer chains; (B) statistically copolymerised P(GMA-POEMA) stabiliser chains; (C) purely anionic POEMA stabiliser chains.[168]

As expected, increasing the proportion of anionic phosphate groups (x) produced higher levels of uniform occlusion (as judged by TGA). The phosphate groups in the steric stabiliser chains enable the nanoparticles to bind strongly to the surface of the growing crystals, resulting in their engulfment. The morphology of the final single crystals can also provide an indication regarding the interaction between the inorganic and organic components. More strongly interacting nanoparticles led to abnormal morphologies, particularly when employed at higher nanoparticle concentrations. More specifically, the calcite morphology remained almost unchanged when using

nanoparticles containing a relatively low level of anionic phosphate groups, whereas unusual flower-like morphologies were observed at higher phosphate contents.

In 2019 Ning et al. reported the efficient occlusion of oil droplets of 250 - 500 nm diameter within calcite single crystals via the ammonia diffusion method.[11] First, sterically stabilised nanoparticles are used to prepare a relatively coarse precursor Pickering emulsion via high-shear homogenisation, which is then subjected to high-pressure microfluidisation to create the nano-sized oil droplets. At some point during these two processing steps, in situ nanoparticle dissociation occurs to generate highly amphiphilic diblock copolymer chains, which then act as a polymeric surfactant or emulsifier for the oil phase. More specifically, $PMAA_x$-$PLMA_y$ diblock copolymer nanoparticles were prepared via RAFT alcoholic dispersion polymerisation of LMA in methanol, as shown in Figure 31. No doubt the relatively low T_g of the PLMA block aids in situ nanoparticle dissociation during either high-shear homogenisation or high-pressure microfluidisation. The maximum extent of oil occlusion achieved under optimised conditions was 11% by mass when using methyl myristate as the oil phase.[11] This is quite remarkable given the significant difference in surface energy between such an oil and calcite.

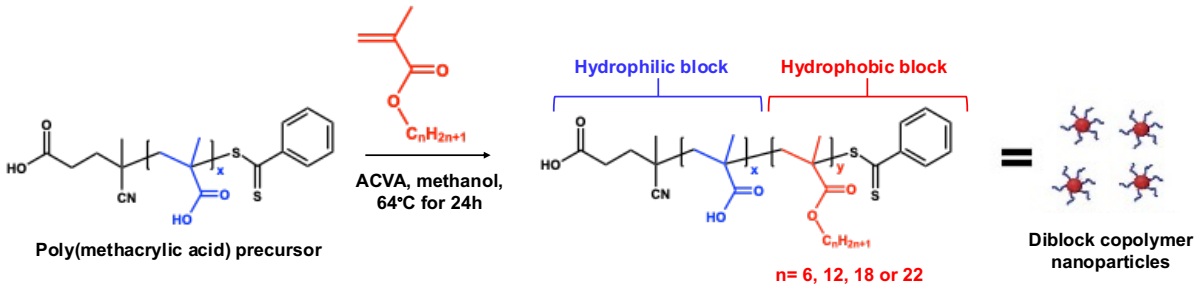

Figure 31. Reaction scheme for the RAFT dispersion polymerisation of lauryl methacrylate in methanol using a poly(methacrylic acid)-based precursor to produce $PMAA_x$-$PLMA_y$ diblock copolymer nanoparticles via PISA.[11]

In order to identify the optimum conditions required for oil occlusion within calcite crystals, Ning et al. examined the nanoparticle concentration used to stabilise the oil droplets, as well as a series of DPs for the stabiliser and core-forming blocks of the $PMAA_x$-$PLMA_y$ diblock copolymer nanoparticles. The findings of this prior study were used as the benchmark for the work carried out in this Thesis. The copolymer concentration used to prepare the nanoemulsion was systematically varied from 0.10 to 0.80% by mass. As a result, the nanoemulsion droplet diameter was reduced from approximately 500 to 250 nm, as judged by analytical centrifugation. The morphology

of the resulting calcite crystals was studied using SEM. It was found that the rhombohedral crystal morphology became increasingly perturbed when using higher nanoparticle concentrations.[11] As suggested by Kim et al. in their nanoparticle occlusion studies,[179] higher concentrations of smaller oil droplets tend to interference with the crystallisation process and hence exert a greater influence over the final crystal morphology. Empirically, the most suitable nanoparticle concentration was found to be 0.10 – 0.20% w/w. However, minimal occlusion was observed by SEM and TGA when using the lowest concentration, perhaps owing to the relatively large droplet diameter. Hence, 0.20% w/w was used by Ning et al. for all subsequent experiments.

In order to maximise the extent of oil droplet occlusion, the amphiphilic character of the diblock copolymer emulsifier was varied to determine which composition was most effective. Firstly, the DP of the hydrophobic PLMA block was varied from 15 to 150.[11] This parameter had an effect on the mean diameter of the resulting oil droplets. Fluorescence microscopy and SEM studies indicated that relatively high extents of occlusion with minimal effect on the crystal morphology could be achieved when using lower PLMA DPs. Above a PLMA DP of 80, lower extents of occlusion were observed and occlusion became primarily surface-confined. Therefore, a DP of 45 for the PLMA block was chosen for further study. The effect of varying the DP of the anionic stabiliser block was also examined. Three PMAA blocks were prepared with mean DPs of 40, 82 or 156. Empirically, it was found that longer stabiliser blocks produced finer oil droplets.[11] SEM images indicated some variation in the morphology of the resulting calcite crystals. Nanoparticles with shorter PMAA blocks did not significantly interact with the crystals, with resulted in lower levels of occlusion and a rhombohedral morphology. In contrast, the crystals possessed truncated edges when employing $PMAA_{156}$. This observation is consistent with a related study by Ning et al., whereby longer anionic stabiliser blocks promoted stronger interactions with growing calcite crystals, hence promoting higher levels of occlusion for block copolymer vesicles.[180] Hence a diblock copolymer composition of $PMAA_{156}$-$PLMA_{45}$ was found to be most efficient for the occlusion of oil droplets within calcite.[11] This copolymer composition was used as a starting point for this Thesis.

In summary, the effective occlusion of various types of nanoparticles - and even nano-sized oil droplets - within calcite has been achieved to produce a range of new

composite materials. According to the literature, various synthetic parameters can be adjusted to aid occlusion, such as the type and density of anionic groups within the steric stabiliser chains, particle size and morphology, and the concentration of both the calcium ions and the occluding species.

2.10 Flavour and Fragrance encapsulation

The use flavours and fragrance compounds is fundamental in many industries attempting to beautify people's lives. However, due to the very sensitive and volatile compounds in their compositions, they are often very difficult to preserve and endure the rough industrial processes.[181] The use of an encapsulation technique has been widely used in recent years in order to create a physical barrier that will retain the physiochemical properties of flavours and fragrances.[182] The ability to successfully encapsulate these volatile compounds and precisely control the mechanism and rate of their release can dramatically expand their application window and improve their efficiency.[183,184] Over the years, several materials have been considered for the storage, delivery and release of volatile compounds, such as naturally occurring or synthetic polymers, with inorganic crystals being the hot spot in latest research activities. Figure 32 below illustrates the main applications for which these capsules are used.

Figure 32. The three main routes of aroma encapsulation, as well as the most common applications of the resulting capsules.[185]

The wall materials used to encapsulate flavours and fragrances need to meet a few requirements in order to be successfully utilised. Although most compounds share the same volatile nature, each oil has a unique composition, thus the appropriate encapsulation material must be able to preserve a wide range of compounds. To be maintained, they must be encapsulated entirely in order to avoid any reactions with the external environment. The material of choice must be biocompatible and inert, thus unable to interact and alter the composition of the flavours and fragrances.[185] The recent need arising in greener, safer, healthier and more economic materials have made inorganic host crystal a very attractive route in fragrance encapsulation and release.

Inorganic crystals are thought to offer exceptional physical and chemical stability when relatively unstable compounds are occluded.[186] Research activities investigated the use of SiO_2 capsules via two main fabrication methods, sol-gel[187,188] and Pickering nanoemulsion[189,190] pathways, both offering controllable morphology and narrow dispersity.[191] Despite SiO_2 capsules being chemically inert with good mechanical properties, the research focus has recently been shifted to calcium carbonate, $CaCO_3$, as the release of encapsulated aroma compounds can be triggered by pH and mechanical forces (eg. mechanical fracture on fabric), which makes them desirable for home care applications.[185] Wang et. al published their ground-breaking results on synthesising oil-in-water emulsions (with fragrance as the oil phase) where calcium carbonate microcrystals (15-20 nm) stabilised the droplets via Pickering emulsion template.[192] The fact that they managed to achieve approximately 90% efficiency with a triggered release at a pH of 2 revolutionises the field of volatile compound encapsulation within biocompatible and bio-inspired inorganic crystals. Figure 33 below illustrates the synthetic pathway for the synthesis of core-shell $CaCO_3$ capsules via an O/W Pickering emulsion.

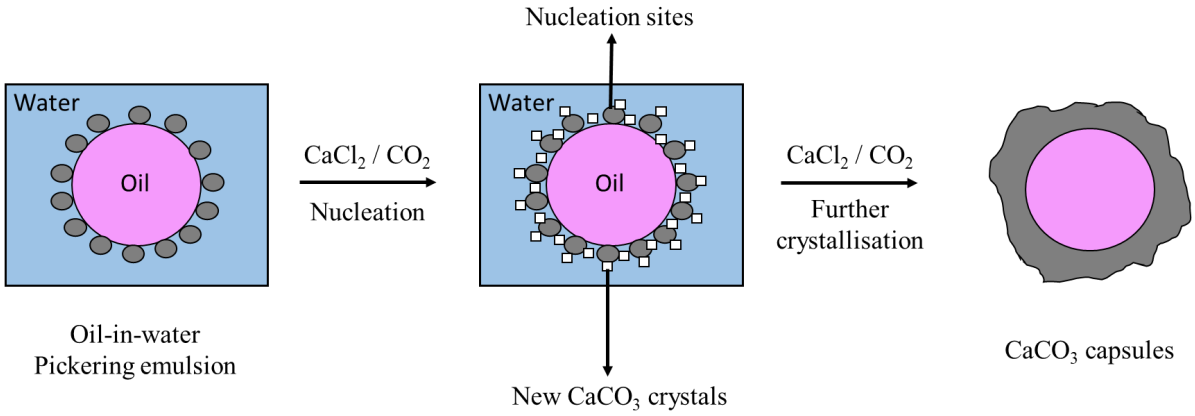

Figure 33. Illustration of the $CaCO_3$ capsule synthesis. [192]

2.11 Project Objectives

The encapsulation of multi-component fragrances within calcium carbonate crystals is a very promising biocompatible alternative to current laundry product formulations. The synthesis of various strongly amphiphilic diblock copolymers will be explored to identify a 'universal' emulsifier for oil-in-water nanoemulsions that can be prepared using a wholly aqueous formulation. This is likely to involve optimisation of both the stabiliser and core-forming block DPs. Once identified, this diblock copolymer emulsifier should enable the encapsulation of various fragrances within the inorganic

host crystal. Furthermore, the gram-scale synthesis of fragrance-loaded crystals will be attempted via the ammonia diffusion method, with alternative pathways also being explored. Such scale-up should enable various analytical techniques to be deployed to assess the parameters that enable efficient fragrance occlusion. Scale-up will also aid examination of the rate (and mechanism) of fragrance release. Since the potential application of the fragrance-loaded crystals will be in fabric conditioner formulations, the mechanism by which the fragrance is deposited onto the fabric during a wash cycle will be examined. Finally, to maximise oil encapsulation within the crystals and their subsequent deposition onto the fabric, an alternative approach will be examined whereby a relatively thick $CaCO_3$ coating will be deposited onto fragrance emulsion droplets stabilised by either surfactants or amphiphilic diblock copolymer chains. The overall aim of this *MPhil* project is shown in Figure 34. The RAFT aqueous emulsion polymerisation of 2-ethylhexyl methacrylate (EHMA) is conducted using a poly(methacrylic acid) (PMAA) precursor to prepare strongly amphiphilic PMAA-PEHMA diblock copolymers, which self-assemble *in situ* to form sterically-stabilised spherical nanoparticles. These nanoparticles are then used as an emulsifier to produce 200-600 nm diameter nanoemulsions by (i) high-shear homogenisation and (ii) high pressure microfluidisation of an oil-water mixture, where the hydrophobic oil is a multi-component fragrance supplied by P & G. The nanoparticles undergo *in situ* dissociation during generation of the nanoemulsion. Hence the oil droplets are stabilised by individual $PMAA_x$-$PEHMA_y$ diblock copolymer chains, rather than the original nanoparticles. In principle, the calcite crystals can serve as a highly biocompatible matrix for fragrance encapsulation and release in fabric conditioner products.

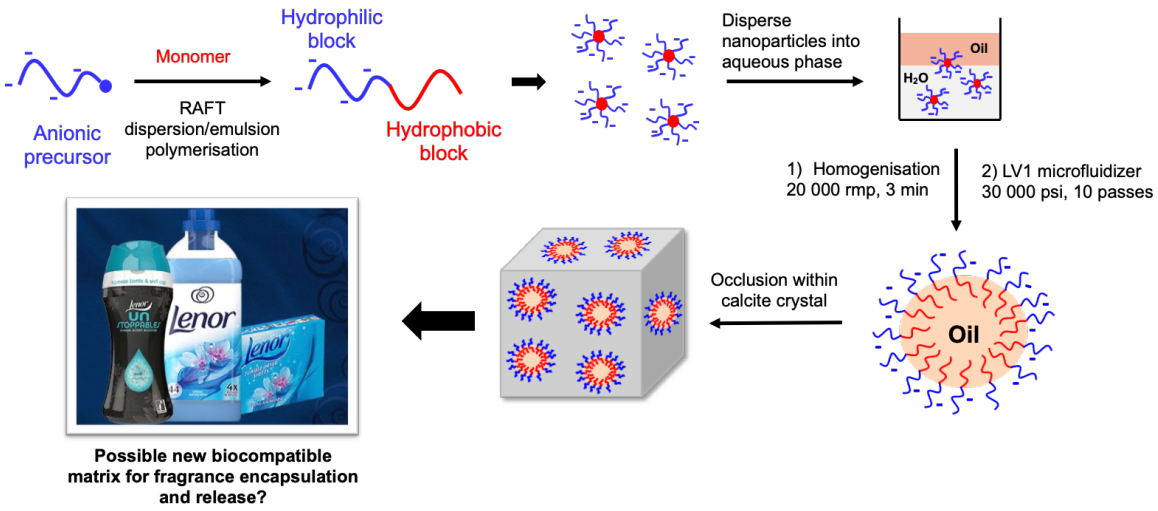

Figure 34. Schematic representation of the synthesis of an amphiphilic diblock copolymer in the form of sterically-stabilised nanoparticles, its use as an emulsifier for the formation of microscopic oil droplets and the subsequent encapsulation of such oil droplets within calcite crystals. In this project, the hydrophobic oil is a multicomponent fragrance supplied by P & G and the calcite crystals serve as a highly biocompatible, cost-effective matrix.

3 EXPERIMENTAL

3.1 Materials

Methacrylic acid (MAA) and 4,4'-azobis(4-cyanovaleric acid) (ACVA; 99%) were obtained from Wako Pure Chemical Industries, Ltd (Osaka, Japan) and used as received. Benzyl methacrylate (BzMA) was purchased from Alfa Aesar (UK) and was passed through an inhibitor remover prior to use. 2-Ethylhexyl methacrylate (EHMA), lauryl methacrylate (LMA), benzyl acrylate (BzA), methyl myristate (MM), Nile Red, 4-cyano-4-(phenylcarbonothioylthio)pentanoic acid (CPCP), 2-cyano-2-propyl dithiobenzoate (CPDB), calcium chloride hexahydrate ($CaCl_2$•$6H_2O$) and ammonium carbonate [$(NH_4)_2CO_3$] were all purchased from Sigma-Aldrich (UK) and used as received. Deionised water was obtained from an in-house Elgastat Option 3A water purification unit. All solvents were obtained from Sigma-Aldrich (UK). The fragrances used (Voyager Zen, APEX, Apple Burst 2, X-Ray 6) and the forced-deposition experimental kit were kindly supplied by P & G Belgium.

3.2 Methods

Synthesis of poly(methacrylic acid)$_x$ (PMAA$_x$) by RAFT solution polymerisation of MAA

The synthesis of a $PMAA_{138}$ precursor is representative and was conducted as follows. ACVA initiator (86.9 mg; 0.31 mmol) and CPCP RAFT agent (0.43 g; 1.53 mmol; [CTA]/[ACVA] molar ratio = 5.0) were added in turn to a 100 mL round-bottomed flask. Ethanol (30.6 g) was then added to the flask, followed by methacrylic acid (20.0 g; 0.232 mol; target DP = 150 at 40% solids). The flask was sealed using a rubber septum wrapped in parafilm. Then the reaction mixture was degassed using a stream of nitrogen gas for 30 min by immersing the flask in an ice bath to minimise evaporation during purging. Once degassing was complete, the sealed flask was immersed in a preheated oil bath set at 70 °C for 5 h. The flask was allowed to cool to room temperature and the reaction mixture was diluted using methanol prior to precipitation into a ten-fold excess of diethyl ether. This precipitation protocol was performed three times to remove traces of methacrylic acid, RAFT agent and initiator residues. The resulting purified PMAA precursor was dissolved in water and isolated by freeze-drying for 48 h. The mean DP of the final PMAA homopolymer was calculated to be 138 using ^{1}H NMR spectroscopy (the integrated signal intensity assigned to the aromatic protons at 7.2 – 8.1 ppm was compared to that of the methacrylic polymer backbone protons

at 0.5 – 2.7 ppm). GPC studies required exhaustive methylation to convert the PMAA into PMMA to ensure that there are no interactions between the polymer and the GPC column. Other examples of $PMAA_x$ precursors were prepared using the same protocol by adjusting the MAA/CPCP molar ratio in order to target lower molecular weights.

Synthesis of poly(methacrylic acid)$_x$–poly(lauryl methacrylate)$_y$ ($PMAA_x$–$PLMA_y$) diblock copolymer nanoparticles by RAFT alcoholic dispersion polymerisation of LMA

The synthesis of $PMAA_{138}$–$PLMA_{45}$ diblock copolymer nanoparticles via RAFT alcoholic dispersion polymerisation of lauryl methacrylate is representative and was conducted as follows. ACVA (3.4 mg, 12.2 μmol), $PMAA_{138}$ macro-CTA (500 mg, 36.5 μmol) and methanol (8.3 g) were added in turn to a 50 mL glass vial, followed by LMA (417.7 mg, 1.6 mmol). A [macro-CTA]/[ACVA] molar ratio of 3 was used for all syntheses. The vial was sealed using a rubber septum wrapped in parafilm and the reaction mixture was purged with a stream of nitrogen gas for 20 min while immersed within an ice bath to minimise evaporation. After degassing, the vial was immersed in a preheated oil bath set at 70 °C and the reaction mixture was stirred for 24 h. The resulting diblock copolymer nanoparticles were dialysed against deionised water using dialysis tubing (molecular weight cut-off = 3,500 Da) for 7 days. The resulting solids content was determined using a moisture analyser and ^{1}H NMR spectroscopy was used to assess the final monomer conversion (>99%). The vinyl signals at 5.6 and 6.5 ppm were compared relative to that of the aliphatic backbone protons at 0.9 – 2.5 ppm.

Synthesis of poly(methacrylic acid)$_x$–poly(2-ethylhexyl methacrylate)$_y$ ($PMAA_x$–$PEHMA_y$) diblock copolymer nanoparticles via RAFT aqueous emulsion polymerisation of EHMA

$PMAA_{138}$–$PEHMA_{45}$ diblock copolymer nanoparticles were prepared via RAFT aqueous emulsion polymerisation of 2-ethylhexyl methacrylate using the following protocol. ACVA (3.4 mg, 12.2 μmol), $PMAA_{138}$ macro-CTA (200 mg, 16.5 μmol) and water (3.135 g for a 10 w/w% solution) were added in turn to a 50 ml glass vial, followed by EHMA (146.8 mg, 740.4 μmol). The vial was sealed using a rubber septum wrapped in parafilm and the reaction mixture was purged using a stream of nitrogen gas for 20 min while immersing the flask in an ice bath to minimise evaporation. After degassing, the vial was immersed in a preheated oil bath set at 70 °C and the reaction mixture

was stirred for 24 h. ^{1}H NMR spectroscopy was used to assess the final monomer conversion (>99%). The vinyl signals at 5.5 and 6.2 ppm were compared relative to that of the aliphatic backbone protons at 0.8 – 2.3 ppm, in CD_3OD. The resulting 10% w/w aqueous dispersion of nanoparticles was used to prepare nanoemulsions without further purification.

Preparation of diblock copolymer-stabilised nanoemulsions

Various oils such as methyl myristate and P&G multi-component fragrances were investigated for the generation of nanoemulsions. A typical protocol used for the preparation of a methyl myristate-in-water nanoemulsion was as follows. Methyl myristate (0.50 mL) was added to water (5.0 mL) and the desired mass of diblock copolymer nanoparticles (0.1 – 0.3 w/w%) was added to this oil-water mixture prior to processing. High shear homogenisation was conducted for 3 min at 20 °C using an IKA Ultra-Turrax T-18 homogeniser operating at 20 000 rpm. The resulting primary emulsion (mean droplet diameter >> 1 μm) was then further processed using an LV1 low-volume Microfluidiser (Microfluidics, USA). The emulsion was passed through the LV1 ten times at an applied pressure of 30,000 psi to obtain a nanoemulsion (mean droplet diameter ~ 200–600 nm depending on the mass of diblock copolymer nanoparticles used). The mean droplet diameter was determined by analytical centrifugation using a LUMiSizer instrument. To assist fluorescence microscopy and confocal microscopy imaging, Nile Red was added to the oil phase (0.25 mg dye per gram of oil). The same protocol was followed when using the multi-component fragrances.

Occlusion of oil droplets within calcium carbonate crystals

Ammonia diffusion method: A fresh nanoemulsion was used to conduct occlusion experiments at 20 ºC. A glass slide was placed in a vial containing an aqueous $CaCl_2$ solution (1.5–50 mM) and 0.20% v/v oil-in-water nanoemulsion. The oil phase was either methyl myristate or one of the multicomponent fragrances provided by P&G. Calcite crystals were formed on exposure to ammonium carbonate vapor (2-20 g, placed at the bottom of a sealed dessicator). After 24 h, the glass slide was removed, rinsed three times with deionised water and allowed to dry in air. The vials were also washed three times with deionised water and, after air-drying overnight, the oil-occluded crystals were collected for further analysis.

Direct mixing method: In a typical experiment, equal volumes of 0.33 M $CaCl_2$•$6H_2O$ and 0.33 M Na_2CO_3 were used. Initially, $CaCl_2$•$6H_2O$ (7.23 g) was dissolved in deionised water (100 mL). 50 mL of the resulting solution was placed in a 250 mL beaker containing a magnetic stirrer. A temperature probe was employed to maintain the solution temperature at 25 ºC. A second solution was prepared by dissolving Na_2CO_3 (3.498 g) in deionised water (100 ml). A syringe pump was used to add 50 mL of this aqueous Na_2CO_3 solution to the $CaCl_2$ solution at a rate of 0.20 mL min^{-1} while stirring at 300-400 rpm. The reaction mixture was then stirred for 50-60 min. The resulting $CaCO_3$ powder was isolated via centrifugation at 10 000 rpm for 15 min followed by redispersion, with this clean-up protocol being repeated three times. The purified calcite crystals were dried at 60 °C overnight.

Synthesis of vaterite crystals: The synthesis of spherical vaterite crystals was attempted in a glass beaker at 25 °C. The temperature was monitored by placing a temperature probe inside a glass vial on the hot plate next to the reaction mixture. Na_2CO_3 (1.59 g, 0.50 M) was dissolved in deionised water (15 ml) along with NaOH (55 mg, 0.05 M). A second solution was made up by dissolving $CaCl_2$•$6H_2O$ (6.57 g, 1.0 M) and sodium citrate (0.221 g, 0.025 M) in water (15 mL). The second solution was added to the first solution with vigorous stirring at 500 rpm for 5 min. The resulting suspension was centrifuged at 10 000 rpm for 10 min (three times) and the resulting white powder was dried at 60 °C overnight.

Characterisation

Dynamic light scattering (DLS): A Malvern Zetasizer NanoZS instrument was used to conduct DLS measurements by detecting back-scattered light at an angle of 173°. Aqueous dispersions were diluted to 0.10% v/v using deionised water prior to analysis. This technique reports the z-average diameter, which is biased towards larger droplets.

Scanning electron microscopy (SEM): A field emission scanning electron microscope (Inspect F instrument) was used to examine the $CaCO_3$ crystal morphology. Crystals were studied on the same glass slide on which they were grown during the ammonia diffusion method. In order to examine whether occlusion was uniform, a clean glass slide was placed on top of the glass slide containing the calcite crystals and the crystals were fractured by pressing down lightly and twisting one slide relative to the other. The resulting fractured calcite crystals were gold-coated (15 mA,

1 min) and sample charging was further minimised by using a relatively low accelerating voltage (5 kV).

Transmission electron microscopy (TEM): TEM images were obtained using a FEI Tecnai G2 Spirit instrument, operating at 120 kV. The copolymer nanoparticles were prepared for imaging by adsorbing a 0.15 % w/w aqueous dispersion of thereof onto palladium-copper grids (Agar Scientific, UK) coated with carbon film. The grids were treated with a plasma glow discharge for approximately 30 seconds to create a hydrophilic surface prior to addition of the aqueous nanoparticle dispersion (5 µL). Excess solvent was removed via blotting and uranyl formate was used to stain the grid for *ca.* 30 seconds. Excess stain was removed via blotting and the grid was carefully dried under vacuum.

Analytical Centrifugation (LUMiSizer): A LUMiSizer analytical photocentrifuge (LUM GmbH, Berlin, Germany) was used to assess the droplet size distribution of each nanoemulsion at 20 °C. Nanoemulsions were diluted to 2.0 v/v%, placed in 2 mm path length polyamide cells and centrifuged at 2,000 rpm for 1,000 profiles (allowing 10 s between profiles). The density of each oil was determined by weighing a known volume using a four-figure balance and this value used as an input parameter. This sizing technique reports the volume-average diameter.

Thermogravimetric analysis (TGA): A Perkin-Elmer Pyris 1 TGA instrument was used to determine the extent of occlusion by heating $CaCO_3$ crystals from 30 °C up to 900 °C in air at a heating rate of 10 °C per min.

Forced deposition test (P & G): The forced deposition test is used to compare the activity of fragrance-loaded calcite crystals against P & G microcapsules and a non-encapsulated fragrance. A formulation was made up comprising 303 mg of fragrance-loaded calcite crystals containing 10 wt% oil and 10.86 g of heavy-duty liquid (HDL) detergent to target a fragrance concentration of 0.30% w/w, assuming an extent of occlusion of 10% by mass. Formulations containing 0.30% w/w fragrance were also prepared using the P&G capsules and the non-encapsulated oil. The components were mixed thoroughly for 5 min. In a conventional washing machine test, 58.47 g of HDL and 15 L of water are used. For these deposition tests, these quantities were scaled down to 0.97 g of HDL and 250 ml of tap water (thus mimicking household conditions). Three cotton cloths were used per sample (9 in total). Each cloth was fully wetted using 100 ml of tap water. Then 100 ml of the wash liquor was placed onto each cloth via pipette and the cloths were hand-washed prior to being hung to dry

overnight. The following day, these samples were evaluated to compare their fragrance intensity before and after physical wrinkling of the cloth. Such mechanical agitation is designed to rupture the microcapsules (or $CaCO_3$ crystals) and hence release the encapsulated fragrance that is deposited onto the cloth.

4 RESULTS & DISCUSSION

4.1 Amphiphilic diblock copolymers for stable fragrance nanoemulsion synthesis

Nanoparticle occlusion within inorganic host crystals has been extensively studied in the last few years.[193] However, the various parameters that influence the extent of occlusion are still not well understood. Of particular relevance to this Thesis, Ning et al. studied the occlusion of oil droplets within calcite crystals, as described in Section 2.4.[11] A series of diblock copolymer nanoparticles was synthesised by RAFT dispersion polymerisation of lauryl methacrylate using various poly(methacrylic acid) precursors. Empirically, it was found that poly(methacrylic acid)$_{156}$ – poly(lauryl methacrylate)$_{45}$ (PMAA$_{156}$-PLMA$_{45}$) formed the most stable (and relatively uniform) oil droplets. It was postulated that the spherical diblock copolymer nanoparticles undergo *in situ* dissociation to form individual copolymer chains under high shear. These strongly amphiphilic copolymer chains then act as a polymeric surfactant and adsorb at the oil-water interface to produce the nanoemulsion. Such copolymers must contain appropriate functional groups that can interact strongly with the growing calcite crystals. Ning et al. demonstrated that poly(methacrylic acid) is well-suited for this purpose.[11] It was hypothesised that the relatively low glass transition temperature (T_g) of the PLMA block aids *in situ* nanoparticle dissociation under high shear.[11] The reaction scheme for the synthesis of PMAA$_x$-PLMA$_y$ is illustrated in Figure 35 below.

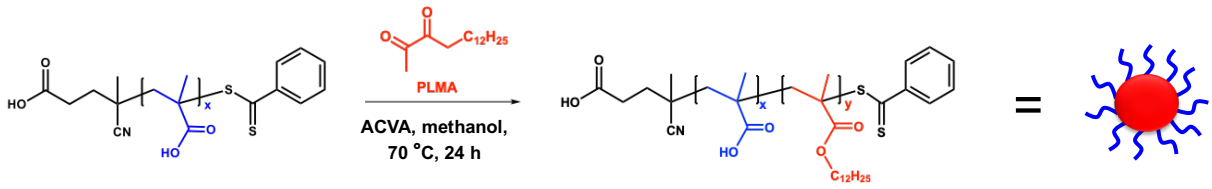

Figure 35. Reaction scheme for the RAFT dispersion polymerisation of lauryl methacrylate in methanol at 70 °C using a poly(methacrylic acid)-based precursor to produce PMAAx-PLMAy diblock copolymer nanoparticles.

Ning et al. reported remarkably high levels of occlusion, with thermogravimetry studies indicating up to 11% w/w oil droplets being incorporated within calcite crystals.[11] This observation led to the intriguing question of whether the model oil (methyl myristate) could be replaced by a hydrophobic multicomponent fragrance, for which the calcite crystals could serve as a cost-effective, environmentally-friendly encapsulating matrix. In principle, the dense crystalline nature of calcite should lead to relatively low permeability, and hence allow excellent long-term retention of the fragrance molecules - unless mechanical fracture of the crystals occurs or there is a change in the solution

pH. In this section, the aim was to examine whether a *single* diblock copolymer emulsifier could act as a 'universal' emulsifier for a range of oils and fragrances. Moreover, the reproducibility of the occlusion process was to be examined. A schematic representation of the generation of the diblock copolymer-stabilised nanoemulsion is shown in Figure 36.

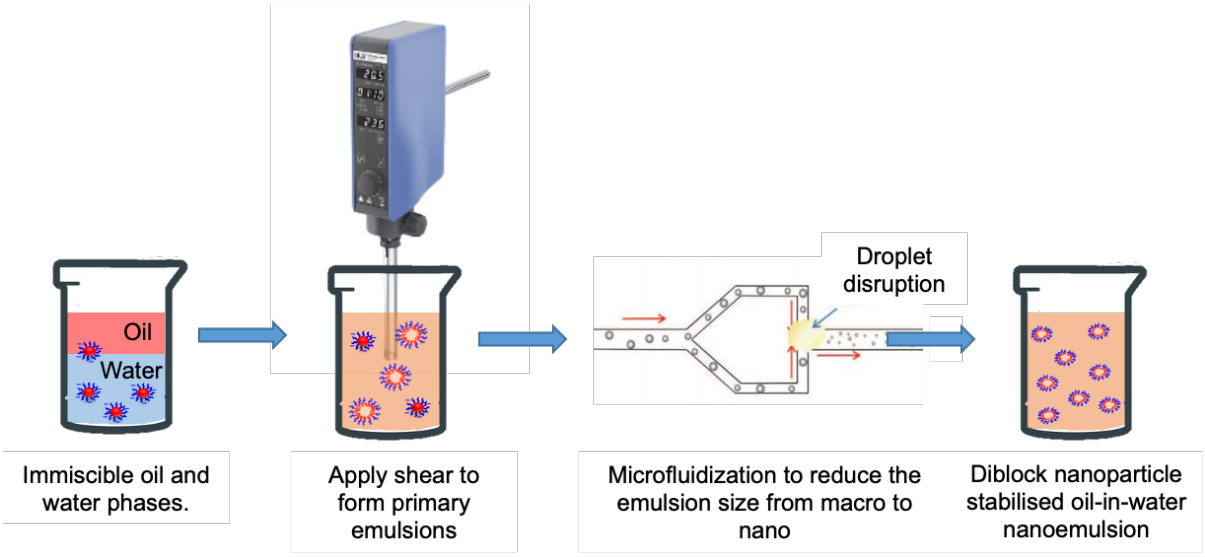

Figure 36. An immiscible mixture of oil and an aqueous dispersion of anionic $PMAA_{156}$-$PLMA_{45}$ diblock copolymer nanoparticles is subjected to high-shear homogenisation to generate a relatively coarse oil-in-water macroemulsion. Subsequently, this primary emulsion is subjected to high-pressure microfluidisation to produce a much finer nanoemulsion that comprises submicron-sized oil droplets stabilised by amphiphilic diblock copolymer chains acting as a soluble emulsifier. In situ dissociation of the anionic $PMAA_{156}$-$PLMA_{45}$ diblock copolymer nanoparticles to produce individual copolymer chains almost certainly occurs, but it is not clear whether this happens during the first step or the second step.

The effect of varying the $PMAA_{156}$-$PLMA_{45}$ concentration from 0.10 to 0.30% w/w on the droplet size, long-term stability and occlusion efficiency of nanoemulsions was examined using four multicomponent fragrances in turn as the oil phase. These commercial fragrances were Voyager Zen, Apple Burst 2, APEX and X-Ray 6 and were supplied by P & G. The volume-average droplet diameter obtained for oil-in-water nanoemulsions prepared using 0.20% w/w fragrance are summarised in Table 1.

Table 1. Volume-average droplet diameter determined via analytical centrifugation (LUMiSizer) analysis of oil-in-water nanoemulsions prepared using 0.20% w/w $PMAA_{156}$-$PLMA_{45}$ nanoparticles and various commercial multicomponent fragrances as the oil phase.

Fragrance	Droplet diameter (nm)
Voyager Zen	311 ± 76
Apple Burst 2	262 ± 51
APEX	315 ± 71
X-Ray 6	322 ± 65

Clearly, the mean droplet diameter does not vary significantly for each fragrance. For comparison, the model oil, methyl myristate, forms droplets of 352 ± 54 nm diameter under the same conditions. These observations confirm that $PMAA_{156}$-$PLMA_{45}$ can indeed act as a 'universal' emulsifier to produce o/w nanoemulsions of an appropriate size for a wide range of oils.

As shown in Figure 37, relatively dense, uniform occlusion can be achieved when using 1.5 mM $CaCl_2$ for the occlusion of nanoemulsions prepared using three of the four multicomponent fragrances shown in Table 1 (for further SEM images, see Figures A1-A3 in the Appendix).

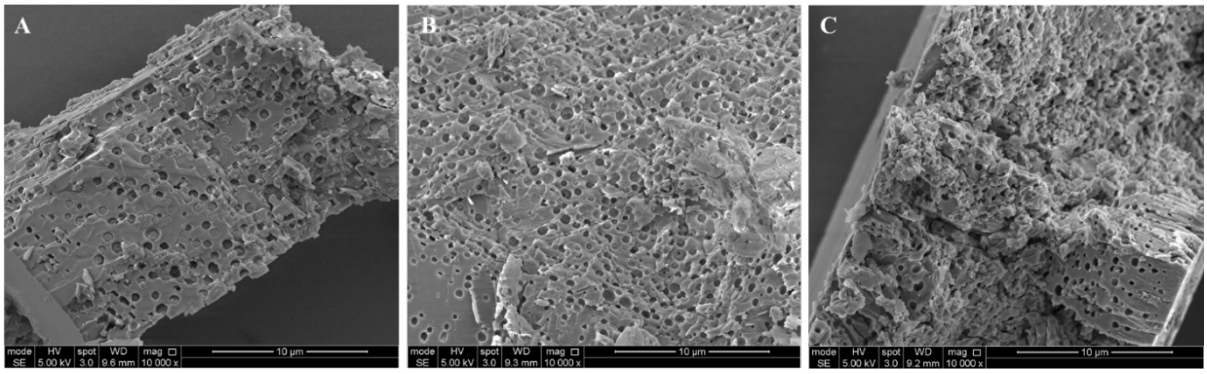

Figure 37. SEM images of ruptured calcite crystals prepared in the presence of o/w nanoemulsions comprising the following commercial fragrances: (A**)** Apple Burst 2, (B**)** APEX and (C**)** X-Ray 6. Occlusion conditions: 1.5 mM $[Ca^{2+}]$; 11.9 mg $PMAA_{156}$-$PLMA_{45}$; pH 9; 20 ^{o}C.

Clearly, this occlusion protocol is not only applicable to simple model oils, but also to multicomponent fragrances. However, this microencapsulation process requires substantial scale-up for it to become commercially viable. Nevertheless, it is certainly encouraging that a *single* amphiphilic diblock copolymer can be used to prepare o/w nanoemulsions of comparable size when using a range of oils/fragrances

4.1.1 Scale-up of oil-occluded crystals

The maximum extent of oil occlusion that has been achieved to date is approximately 11% w/w.[11] However, the isolated mass of oil-occluded calcite crystals remains very low (5-10 mg), which hinders multi-technique analysis using destructive techniques such as thermogravimetry. To better understand the various parameters that influence the extent of occlusion, a reliable scale-up protocol must be established. The two main methods considered here are the ammonia diffusion method (which produces calcite crystals deposited on a glass slide) and the direct mixing method (which generates calcite crystals in the form of an aqueous suspension).

4.1.1.1. Ammonia diffusion method

One of the most commonly used techniques for the laboratory-scale synthesis of calcium carbonate is the so-called ammonia diffusion method.[194] This involves using ammonium carbonate and calcium chloride hexahydrate for the synthesis of calcite crystals and is described in detail in Chapter 3.2. Figure 38 illustrates the experimental protocol, as well as an example of the resulting oil-occluded calcite crystals prepared using an oil that contains Nile Red, which confers a pink colouration (for further details see Figure A4 in the Appendix).

This ammonia diffusion method works well for the preparation of small quantities of calcite crystals. The standard protocol involves using 1.5 mM [Ca^{2+}] to produce *ca*. 10 mg oil-occluded crystals. However, scale-up is somewhat problematic because the nanoemulsion becomes unstable at higher $CaCl_2$ concentrations. Thus, an attempt was made to identify the maximum $CaCl_2$ concentration that did not cause nanoemulsion instability. The $CaCl_2$ concentration was systematically varied in a series of experiments conducted at 1.5, 3, 5, 10, 20, 30 and 50 mM. Unfortunately, the latter two concentrations proved to be too high because sedimentation of the calcite crystals was observed (see Figure 39).

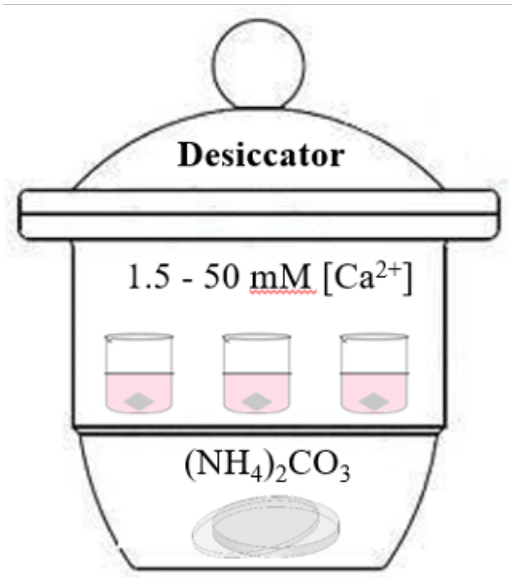

Figure 38. Schematic representation of the ammonia diffusion method, using a desiccator containing a 1.5 – 50 mM $CaCl_2$ solution mixed with the nanoemulsion and $(NH_4)_2CO_3$ powder as a source of carbonate for the synthesis of calcite. Oil-occluded $CaCO_3$ precipitates on the sides of the glass vial over the course of 24 h.

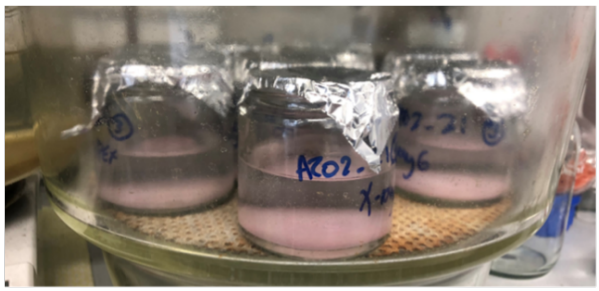

Figure 39. Gravitational sedimentation of pink calcite crystals observed after 24 h when using the ammonia diffusion method at 50 mM $CaCl_2$. The pink colouration arises from the presence of Nile Red dye dissolved in the oil phase (methyl myristate in this case).

No oil occlusion was achieved when growing calcite crystals using either 30 or 50 mM $CaCl_2$ Moreover, these crystals were much larger (up to 150-200 μm) than those formed when using lower $CaCl_2$ concentrations. The fact that no occlusion took place was initially indicated by optical microscopy studies and subsequently confirmed by SEM analysis and thermogravimetry measurements. SEM images are shown in Figure 40 for the 50 mM $CaCl_2$ experiment. The oil droplets become unstable under such conditions. Owing to their *in situ* coalescence, not even surface occlusion could be achieved.

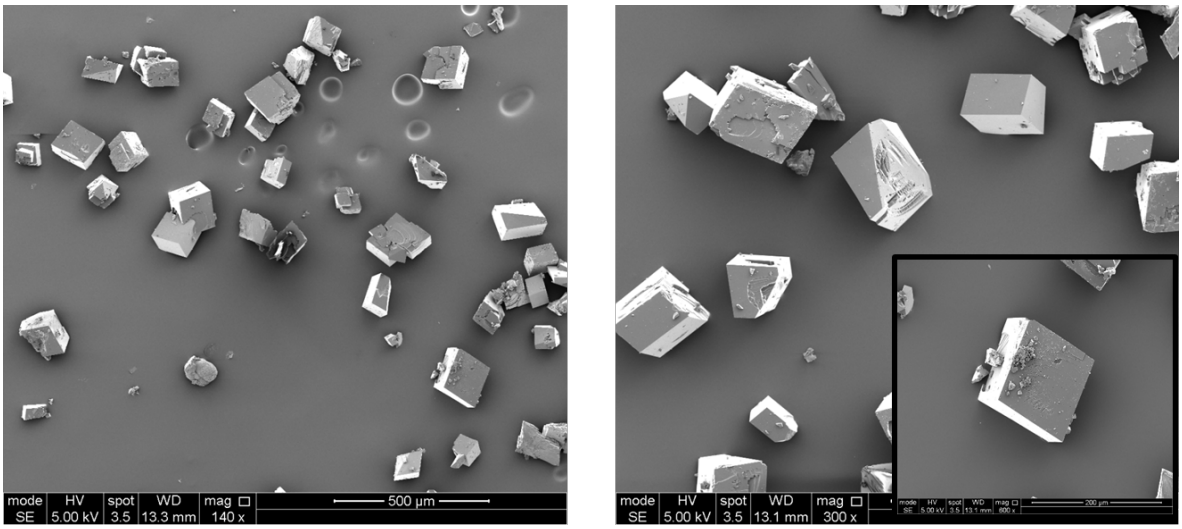

Figure 40. SEM images recorded for calcite crystals produced using 50 mM [Ca^{2+}], 11.9 mg $PMAA_{138}$-$PLMA_{45}$ copolymer and the multicomponent fragrance Voyager Zen as the oil phase at pH 9 and 20 ºC.

There is a strong correlation between the extent of oil occlusion and the crystal morphology. As shown in Figure 40, the resulting single crystals exhibit a distinctive rhombohedral structure. In contrast, crystals with rounder edges and a sponge-like porous structure were obtained when using 20 mM $CaCl_2$ solution (see Figure 41). These images were obtained using a benchtop SEM (FLEX-SEM instrument) at P&G.

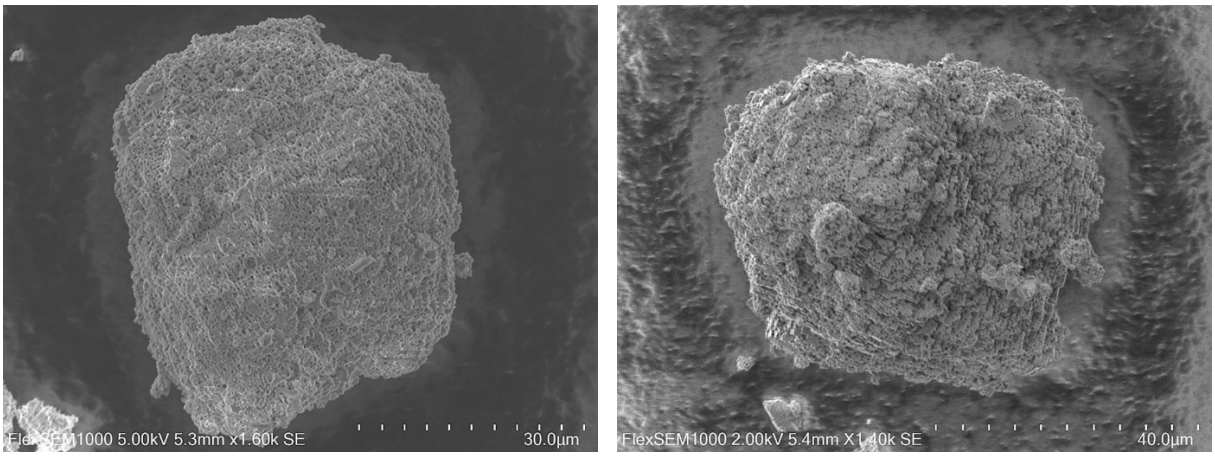

Figure 41. FLEX-SEM images of an X-RAY 6-occluded calcite crystal prepared at 20 mM [Ca^{2+}] using 11.9 mg $PMAA_{138}$-$PLMA_{45}$ at pH 9 and 20 °C

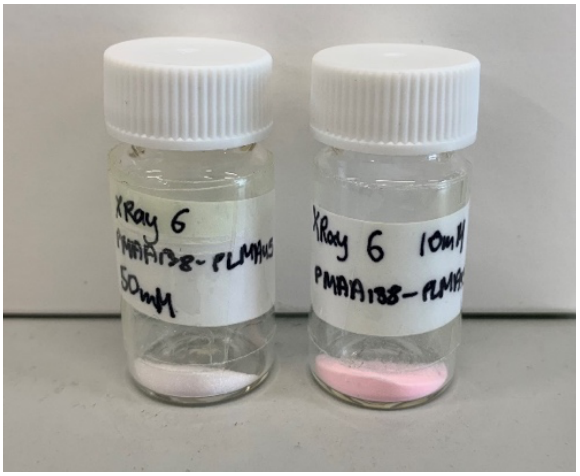

Figure 42. LHS: Calcite crystals collected after crystallisation using 50 mM [Ca^{2+}], 11.9 mg $PMAA_{138}$-$PLMA_{45}$ and X-RAY 6 as the oil phase. White appearance indicates unsuccessful occlusion. RHS: Calcite crystals collected after crystallisation using 10 mM [Ca^{2+}], 11.9 mg $PMAA_{138}$-$PLMA_{45}$ and X-RAY 6 as the oil phase. The pink hue indicates successful oil occlusion within these crystals.

In principle, adding an oil-soluble dye such as Nile Red to the oil phase should facilitate fluorescence microscopy studies. It also indicates immediately whether occlusion has been successful or not simply by inspecting the colour of the resulting calcite crystals. Thus, oil droplet incorporation should lead to pink crystals, whereas if the crystals remain white – as when employing higher $CaCl_2$ concentrations – this indicates minimal or zero occlusion. This principle is illustrated in Figure 42, which shows digital photographs recorded for calcite crystals prepared using 11.9 mg of $PMAA_{138}$-$PLMA_{45}$ to stabilise oil droplets comprising the multi-component fragrance X-RAY 6 at either 10 or 50 mM $CaCl_2$.

At the lower $CaCl_2$ concentration, the nanoemulsion remained stable during crystallisation. This results in successful oil occlusion within the host crystal lattice, as indicated by the distinctly pink crystals. On the other hand, only white crystals – signifying no detectable occlusion – were obtained at the higher $CaCl_2$ concentration.

Optical microscopy studies of calcite crystals prepared at 10 or 20 mM $CaCl_2$ suggested a high level of occlusion because the distinctive rhombohedral morphology was lost. However, SEM studies of the ruptured crystals indicated that only surface

occlusion was achieved, rather than uniform occlusion throughout the crystals. Such observations are perhaps surprising because uniform occlusion of up to 11% w/w oil droplets could be achieved when using 1.5 mM $CaCl_2$ to occlude the same fragrance (see Figure A5 in the Appendix). No oil occlusion was observed within calcite when employing either 10 mM $CaCl_2$ (APEX fragrance) or the 20 mM $CaCl_2$ (X-RAY 6 fragrance) in combination with the $PMAA_{138}$-$PLMA_{45}$ diblock copolymer.

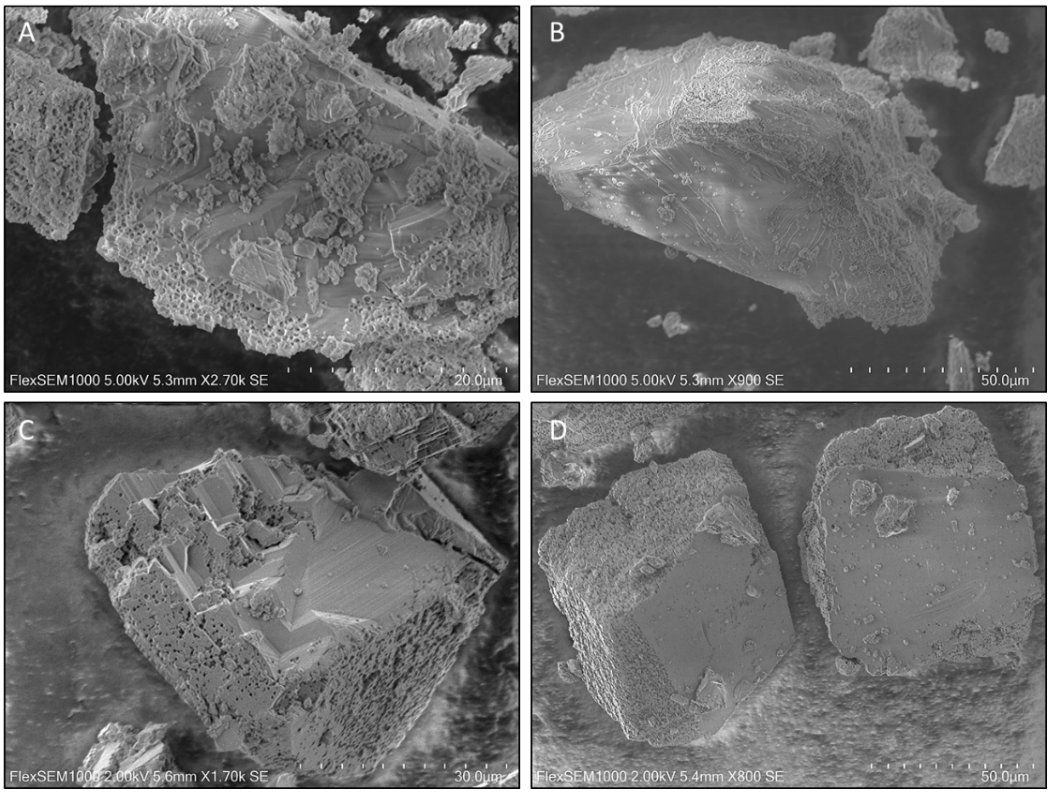

Figure 43. FLEX-SEM images recorded for a multi-component fragrance (X-RAY 6) within occluded calcite crystals prepared by the ammonia diffusion method using 11.9 mg $PMAA_{138}$-$PLMA_{45}$. **(A, B)** 20 mM $CaCl_2$; **(C, D)** 10 mM $CaCl_2$..

Raman spectroscopy and TGA studies were also undertaken. The former technique enables us to study individual crystals and offers sufficient spatial resolution (ca. 1 x 1 μm^2) to enable spectra to be recorded for the oil-rich regions within the calcite. Thus, in principle this enables the spatial distribution of fragrance within the crystal to be mapped. Based on the SEM images, it was expected that the near-surface of each crystal would be fragrance-rich, whereas its interior would be calcite-rich. This hypothesis was confirmed by Raman mapping experiments. The spectra used to conduct the following mapping experiment are shown in Figure A6 (see Appendix). The carbonyl band at *ca*. 1700 cm^{-1} and an intense aliphatic C-H stretch at *ca*. 2900 cm^{-1} were assigned to fragrance molecules and hence used to identify fragrance-rich

regions within the crystal. Similarly, strong bands at *ca*. 700 cm^{-1} and 1100 cm^{-1} were assigned to the calcite component. Figure A7 (see Appendix) shows the overlayed spectra of the APEX and X-RAY 6 occluded crystals, both synthesised at 20 mM [Ca^{2+}], showing that the peaks for X-RAY 6 are predominating when compared to APEX. The reason for the difference in peak intensity could be due to different extents of occlusion, or purely due to structure differences of the fragrances. Figure 44 shows the Raman map recorded for a single oil-occluded calcite crystal. On the LHS, the red area indicates fragrance-rich areas - which are confined to the outer surface of the crystal - while the blue area indicates an almost pure calcite region within the interior of the crystal. The more complex cursor images show the three main bands in three different colours for clarity; pure $CaCO_3$ is denoted in red, the carbonyl band at *ca*. 1700 cm^{-1} is shown in green and the 2900 cm^{-1} C-H stretch is indicated in blue. Again, most of the fragrance droplets are confined to the crystal edges/ surfaces, as indicated by SEM studies. Clearly, the crystal morphology has been significantly affected, yet the overall extent of occlusion remains relatively low owing to inefficient droplet engulfment during calcite formation.

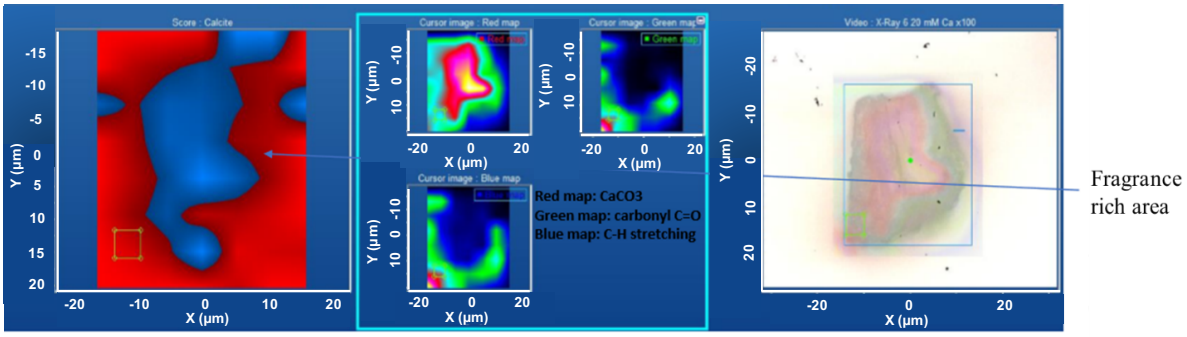

Figure 44. Raman mapping experiment conducted on an individual X-RAY 6-occluded calcite crystal. Occlusion conditions: 20 mM [Ca^{2+}]; 11.9 mg $PMAA_{138}$-$PLMA_{45}$; pH 9; 20 °C.

Finally, thermogravimetry was used to confirm the relatively low level of occlusion for the calcite crystals prepared using 20 mM $CaCl_2$, X-RAY 6 and 11.9 mg $PMAA_{138}$-$PLMA_{45}$, as seen in Figure 45 below.

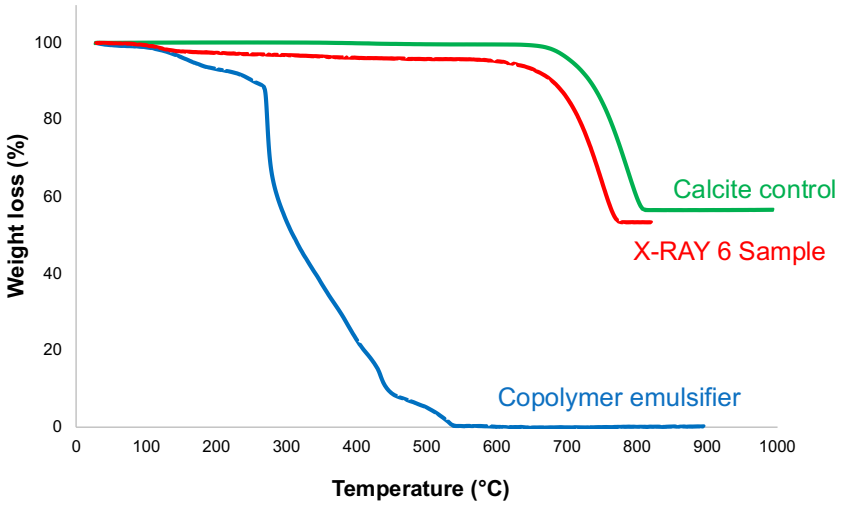

Figure 45. TGA curves recorded for X-RAY 6-loaded calcite crystals prepared using 20 mM $CaCl_2$ (red curve) pure calcite (green curve) and the $PMAA_{138}$-$PLMA_{45}$ diblock copolymer alone (blue curve).

A control experiment performed using pure calcite confirmed the expected 44% mass loss owing to release of CO_2 during its thermal decomposition, with the remaining solid residue being 56% CaO. If oil droplet occlusion within the $CaCO_3$ crystals occurs, this reduces the CaO content to less than 56%, which enables the extent of occlusion to be calculated. This is because both the oil and the diblock copolymer emulsifier are completely pyrolysed at *ca.* 550 °C, thus only CaO remains as an incombustible residue at 900 °C. In this particular example the remaining residue after heating the fragrance-occluded calcite crystals was 53.3%, hence the oil content was calculated to be equal to 4.8% by mass.

For comparative purposes, a second sample prepared with 20 mM $CaCl_2$ and using the APEX fragrance as the oil phase was studied by Raman microscopy. The purpose here was to determine whether the same crystallisation behaviour occurs regardless of the chemical nature of the fragrance. The same four vibrational bands were used to analyse this sample. The resulting 2D mapping of the single crystal is shown in Figure 46. Again, the interior of the crystal is calcite-rich, with fragrance-rich regions observed at its near-surface. The X-RAY 6 fragrance exhibited stronger aliphatic C-H and carbonyl stretches than the APEX fragrance, indicating a significant difference in the fragrance composition (comparative spectra can be found in the Appendix, see Figure A7).

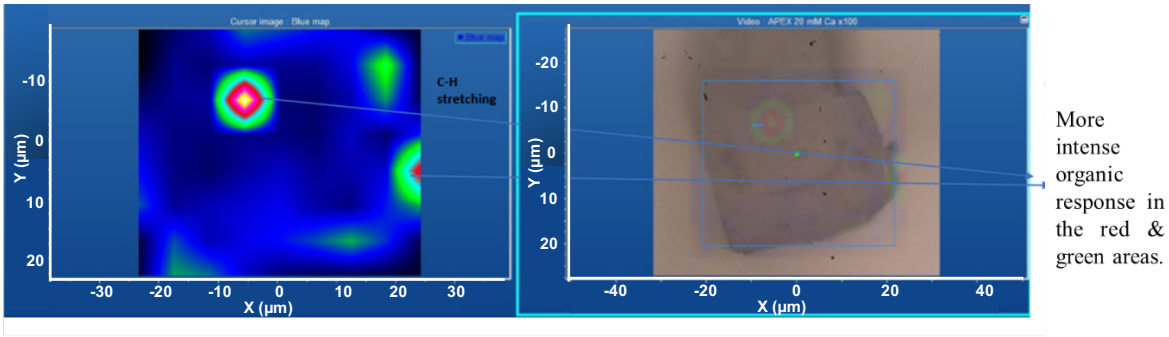

Figure 46. Raman microscopy map recorded for an individual APEX fragrance-loaded calcite crystal. Occlusion conditions: 20 mM [Ca^{2+}]; 11.9 mg $PMAA_{138}$-$PLMA_{45}$; pH 9; 20 °C.

Preliminary Forced Deposition Tests

P & G uses well-established experimental protocols to assess the performance of their new laundry formulations and compare them to established products. Their in-house forced deposition test is used to screen microcapsule leakage when mixed with laundry detergent, after deposition onto a fabric and subsequent fragrance release after fracture of the microcapsules. However, it is only a relative test that is based solely on an individual's perception of smell.

X-RAY 6-loaded calcite crystals prepared using 20 mM $CaCl_2$ and 11.9 mg $PMAA_{138}$-$PLMA_{45}$ were examined. The fragrance encapsulation efficiency of such crystals was compared against (i) the unencapsulated fragrance and (ii) X-RAY 6-loaded polymer-based microcapsules provided by P & G that are currently used in commercial products. Due to the limited amount of X-RAY 6-loaded calcite crystals available, formulations with a theoretical 0.30% w/w fragrance loading were made up. The three samples were deposited onto water-soaked white cloths that were then left to dry overnight. In principle, the unencapsulated fragrance formulation should initially exhibit an intense aroma both during fragrance deposition and after the washing step. However, given the volatile nature of the fragrance molecules, little or no aroma should be detected after drying owing to their evaporation overnight. In contrast, effective fragrance-loaded microcapsules should not be leaky when placed in the detergent formulation and should not release any fragrance during either the perfume deposition or the washing step. The fragrance should only be detectable after rubbing (or abrasion) of the cloth because this fractures the microcapsules and so releases their payload, see Figure 47. This test is used to demonstrate the importance of

microencapsulation technology for proving a consumer cue. Ideally, the commercial microcapsules provided by P & G capsules and the fragrance-occluded calcite crystals should behave similarly. However, this was not the case. The former microcapsules performed well: there was no leakage on mixing with the laundry formulation, but an intense aroma was evident upon their fracture. The fragrance-loaded calcite crystals did not meet the criteria for a successful forced deposition test. As expected, no fragrance was detected on mixing with the laundry detergent, but unfortunately no 'burst' release could be detected after vigorous abrasion of the deposited cloth.

Figure 47. Schematic cartoon to illustrate the forced deposition protocol conducted at P&G. **1)** Preparation of a 0.3 wt% fragrance formulation and deposition onto a water saturated cloth; **2)** Replication of hand-washing conditions of the fragrance-deposited cloth; **3)** Hanging of the cloth to let dry overnight. Three formulations were compared: (**i)** Unencapsulated X-RAY 6; (**ii)** P&G commercial X-RAY 6 capsules; (**iii)** X-RAY 6 – occluded calcite crystals prepared via the ammonia diffusion method.

If the calcite crystals had partially dissolved when immersed in the detergent liquid or during the washing step, then the fragrance should be detected. However, since no fragrance could be detected either during mixing or upon fracture, it was concluded that the amount of oil encapsulated within the crystals must be relatively low (less than 10% w/w). Thus the actual amount of oil in the formulation was less than 0.30% w/w, making it very difficult to detect. This hypothesis was confirmed by TGA, see Figure 45. Better occlusion performance is required to achieve higher fragrance loadings within the calcite crystals. So far, the $CaCl_2$ concentration has been varied with the fragrance volume fraction in the nanoemulsion being kept constant at 2.0% v/v. Presumably, there are simply too few droplets present in this dilute nanoemulsion for efficient occlusion. Thus, to increase the extent of fragrance occlusion within calcite, the oil volume fraction should be increased substantially, perhaps up to 30% v/v. Further fragrance occlusion experiments are described below.

4.2 Model deformable particles

For an experimental protocol to be industrially relevant, it should be both robust and readily scalable and preferably also as simple as possible. One obvious disadvantage to the oil occlusion protocol reported by Ning et al.[11] is that the amphiphilic diblock copolymer emulsifier had to be initially prepared in methanol before being transferred into aqueous solution for the occlusion studies. Given the cost and toxicity of this solvent, it would be much more convenient if the diblock copolymer emulsifier could be prepared directly via RAFT aqueous emulsion polymerisation.[195] This would be more environmentally-friendly and also eliminate the relatively slow dialysis step. Unfortunately, lauryl methacrylate is not amenable to via aqueous emulsion polymerisation because this monomer does not possess sufficiently high aqueous solubility for its efficient mass transport from the monomer droplets to the locus of the polymerisation.[196] Instead, 2-ethylhexyl methacrylate (EHMA) was chosen as the hydrophobic comonomer. This was because we had recently successfully performed the RAFT aqueous emulsion polymerisation of *n*-hexyl methacrylate[197] and we hypothesised that EHMA should also possess sufficient aqueous solubility to be suitable for such a formulation.

Three anionic PMAA precursors were prepared via RAFT solution polymerisation of MAA in ethanol with differing mean DPs: $PMAA_{62}$, $PMAA_{138}$ and $PMAA_{222}$, see Figure 48.

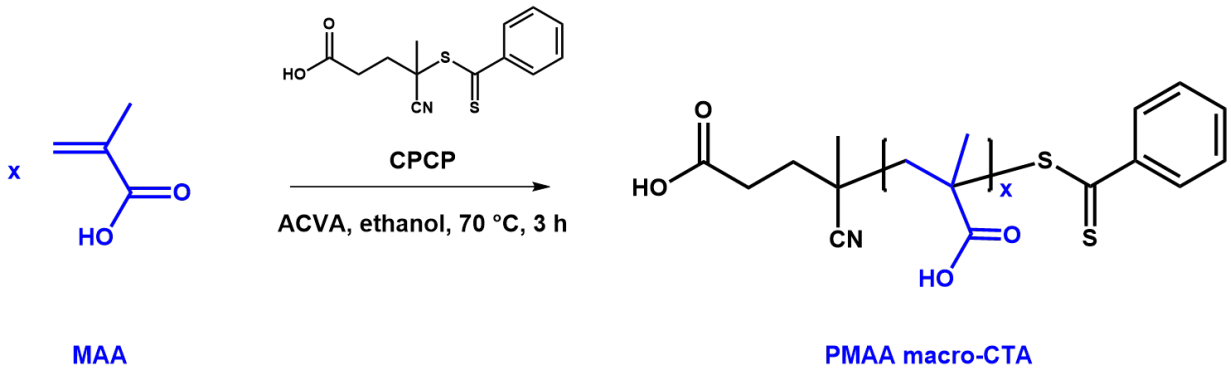

Figure 48. Reaction scheme for the RAFT solution polymerisation of methacrylic acid in ethanol using a CPCP RAFT agent and ACVA initiator to produce PMAA precursors with x = 62, 138 or 222.

All three PMAA precursors were characterised using THF GPC. Prior to GPC analysis, each precursor was reacted with excess trimethylsilyldiazomethane to methylate all the carboxylic acid groups. ^{1}H NMR spectra recorded for the unreacted and methylated $PMAA_{62}$ are shown in Figure 49. The degree of methylation can be

determined by integrating the new proton signal **g** at 3.4 – 3.9 ppm assigned to the methoxy group and comparing this to the integrated methacrylic backbone signals at 0.50 – 2.2 ppm. By this method, the mean degree of esterification was calculated to be 99%. This was sufficiently high to enable GPC analysis to be conducted.

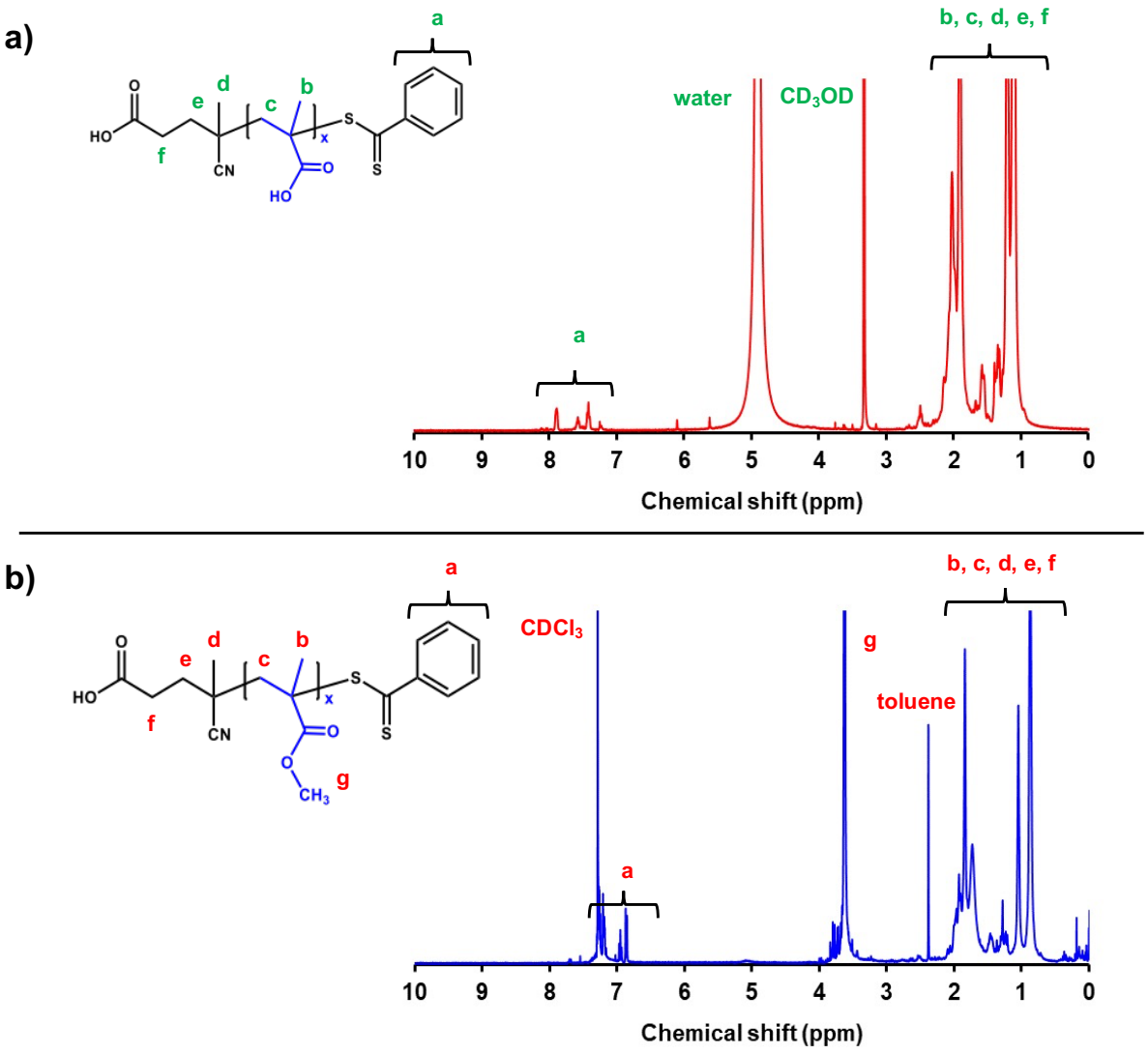

Figure 49. ^{1}H-NMR spectra recorded for (a) $PMAA_{62}$ in CD_3OD and (b) methylated $PMAA_{62}$ in $CDCl_3$. The peaks at *ca.* 0 ppm on spectrum (b) arise from the trimethylsilyldiazomethane methylating agent.

Each methylated PMAA precursor was analysed by THF GPC, see Figure 50. In each case, a relatively narrow molecular weight distribution is obtained (M_w/M_n < 1.25). However, a high molecular weight shoulder is also observed, which may be related to the incomplete methylation of the carboxylic acid groups.

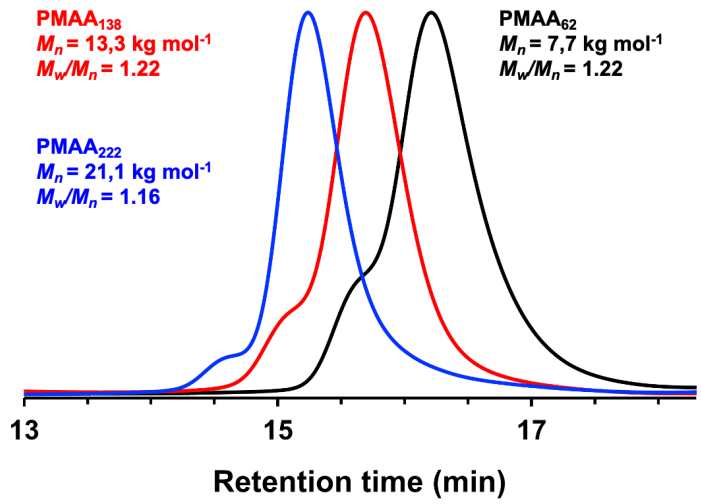

Figure 50. THF GPC curves recorded for three PMAA precursors with mean DPs of 62, 138 or 222.

Each anionic PMAA precursor was then chain-extended via RAFT aqueous emulsion polymerisation of EHMA at 70°C with various PEHMA DPs being targeted, see Figure 51.

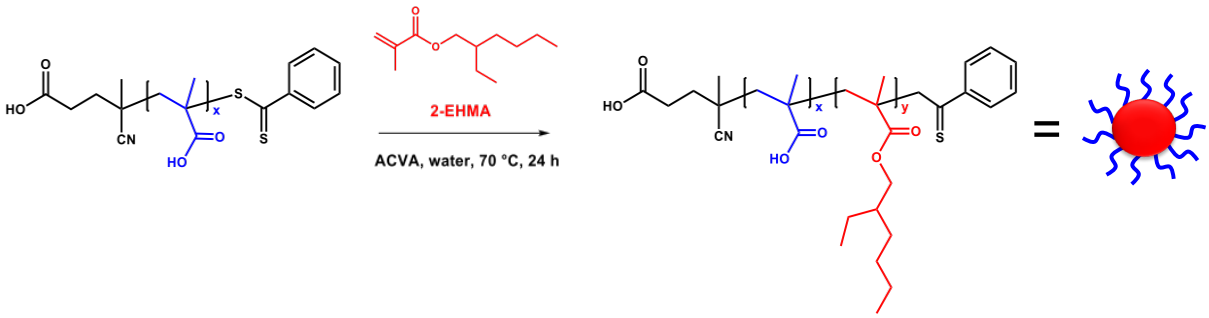

Figure 51. Reaction scheme for the RAFT aqueous emulsion polymerisation of 2-ethylhexylmethacrylate (EHMA) to afford sterically-stabilised $PMAA_x$-$PEHMA_y$ diblock copolymer nanoparticles.

The optimum pH and solids content was also investigated for this aqueous PISA formulation. According to the literature, PMAA is best chain-extended at pH 5.0.[151] However, this pH was unsuccessful for the RAFT aqueous emulsion polymerisation of EHMA. DLS measurements indicated that no nanoparticles were formed, which suggests a substantially incomplete polymerisation. Thus this heterogeneous polymerisation was also performed at pH 2.7 and pH 8.0, see Figure 52. The latter pH led to a change in colour that suggested premature deactivation of the dithiobenzoate-based RAFT agent. A similar problem has been reported by McCormick and co-workers, who observed end-group hydrolysis under similar conditions.[149] Fortunately, the former pH enabled the formation of uniform spherical nanoparticles. The target solids content was varied from 10 to 25%, see Figure 52. At 25%, the resulting

dispersion proved to be too viscous, with the resulting free-standing gel leading to inefficient stirring. Therefore, the remaining RAFT aqueous emulsion polymerisations conducted in this Thesis were performed at 20% w/w solids and pH 2.7.

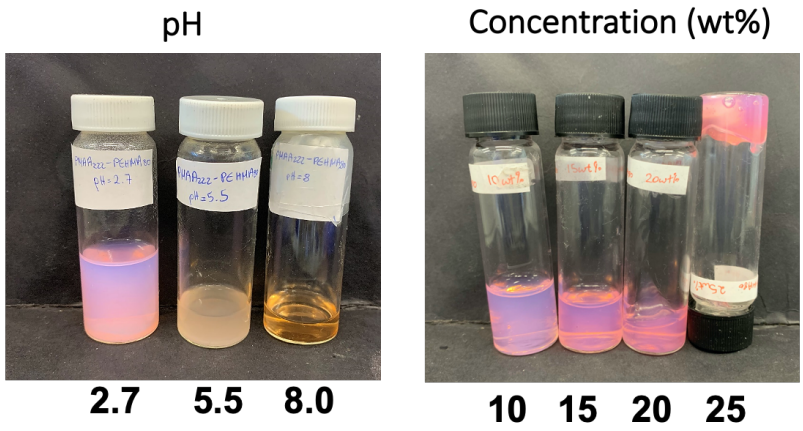

Figure 52. Digital photographs showing the effect of varying the dispersion pH and copolymer concentration during the synthesis of $PMAA_x$-$PEHMA_y$ diblock copolymer nanoparticles via RAFT aqueous emulsion polymerisation of EHMA at 70°C.

For each of the three PMAA precursors, PEHMA DPs of 30, 50, 100, 200, 300 and 400 were targeted under otherwise identical reaction conditions. The resulting nanoparticles were characterised by DLS, which reports the hydrodynamic z-average diameter. The evolution in nanoparticle diameter when varying the PEHMA DP is shown in Figure 53. For the $PMAA_{62}$ and $PMAA_{222}$ series, larger nanoparticles are obtained up to a PEHMA DP of 200, with an almost constant size being observed thereafter. A similar trend is observed for the $PMAA_{138}$ series, except in this case the nanoparticle diameter becomes more or less invariant above a PEHMA DP of 100. In all cases, the DLS polydispersity remains below 0.10, which indicates reasonably narrow particle size distributions.

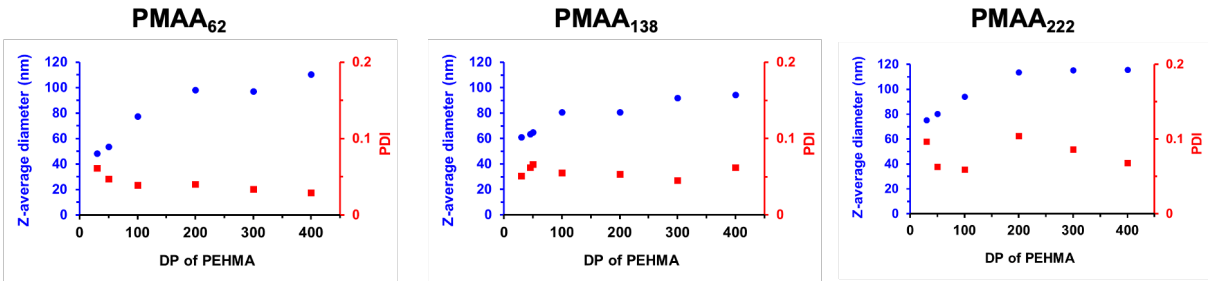

Figure 53. Variation in DLS z-average diameter and DLS polydispersity observed for the RAFT aqueous emulsion polymerisation of EHMA when systematically increasing the PEHMA DP when employing three different $PMAA_x$ precursors (x = 62, 138 or 222).

The diblock copolymers were analysed by GPC to assess their molecular weight distributions. Initially, the same methylating protocol was followed: thimethylsilyldiazomethane was used to convert PMAA into PMMA and hence minimise interactions with the GPC column when using a THF eluent. However, this technique proved to be inappropriate for these PMAA-PEHMA diblock copolymers since it led to inter-chain branching. Presumably, the highly reactive ketene diradical intermediate can abstract hydrogen atoms from the branched alkyl groups, which leads to radical-radical coupling. Certainly, the GPC curves recorded for a series of $PMAA_{62}$-$PEHMA_y$ diblock copolymers exhibit bimodal molecular weight distributions and hence relatively high dispersities (see Figure 54).

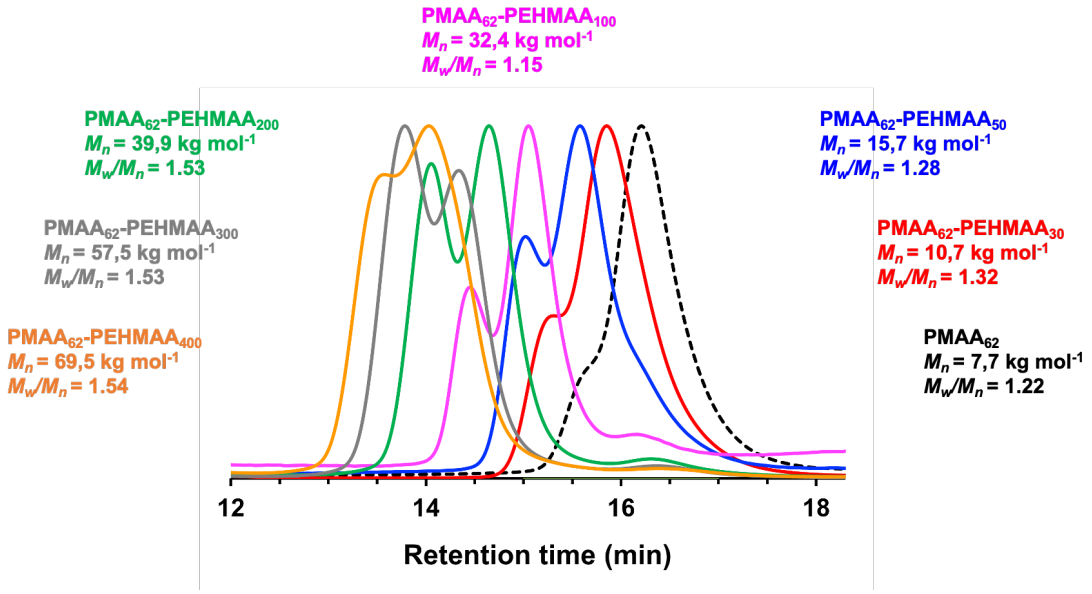

Figure 54. THF GPC traces recorded for a series of $PMAA_{62}$-$PEHMA_y$ diblock copolymers prepared via RAFT aqueous emulsion polymerisation of EHMA at 70°C when targeting 20% w/w solids at pH 2.7

Since selective methylation was unsuccessful for this particular diblock copolymer, an alternative method was employed whereby 4.0% v/v glacial acetic acid was added to the THF eluent. This acid protonates the carboxylic acid groups on the PMAA blocks and hence minimises unfavourable interactions with the GPC column. GPC traces obtained for the three series, $PMAA_{62}$-$PEHMA_y$, $PMAA_{138}$-$PEHMA_y$ and $PMAA_{222}$-$PEHMA_y$ are shown in Figure 55. The GPC traces remain unimodal and are gradually shifted to higher molecular weight when targeting higher PEHMA DPs. However, longer diblock copolymer chains always exhibited higher dispersities, with dispersities exceeding 1.50 for DP $\geq$ 200. In each case, ^{1}H NMR spectroscopy studies indicated that the EHMA polymerisation had proceeded to essentially full conversion.

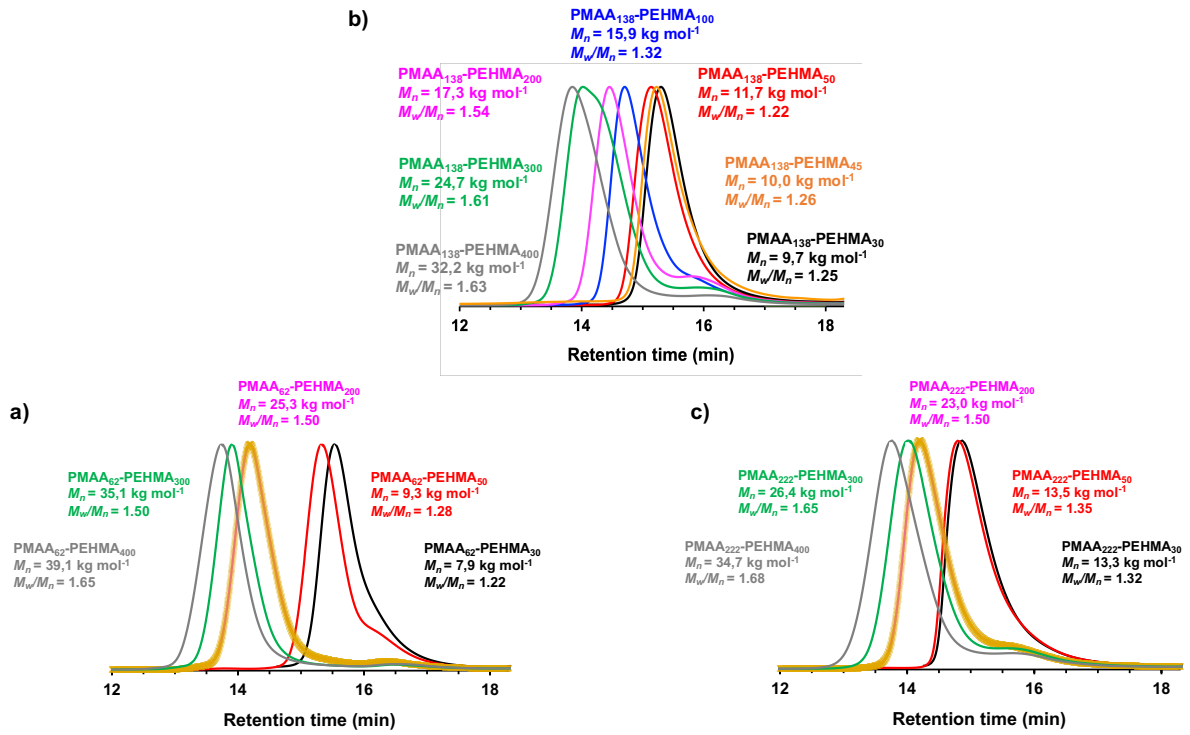

Figure 55. GPC traces recorded for $PMAA_{62}$-$PEHMA_y$, $PMAA_{138}$-$PEHMA_y$ and $PMAA_{222}$-$PEHMA_y$ diblock copolymers using THF eluent containing 4.0% v/v acetic acid.

Given the overall aim of this Thesis, the diblock composition chosen for the oil (and fragrance) occlusion experiments is $PMAA_{138}$-$PEHMA_{45}$. This is because this diblock composition most closely resembles $PMAA_{156}$-$PLMA_{45}$, which was reported to be the best-performing amphiphilic diblock copolymer by Ning et. al.[11] Its unimodal GPC trace is shown in Figure 56: this particular diblock copolymer has an M_n of 10,000 g mol^{-1} and a relatively low dispersity (M_w/M_n = 1.26).

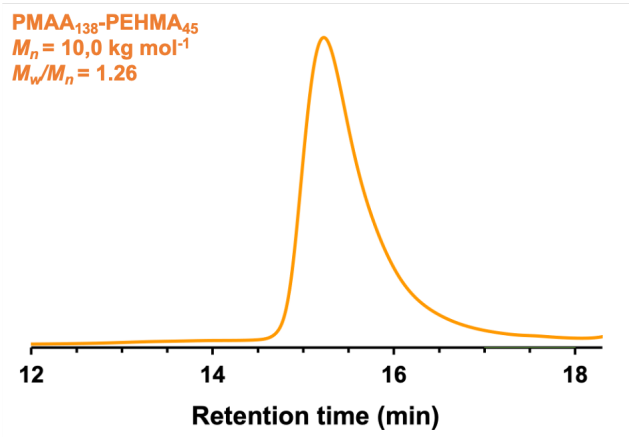

Figure 56. GPC trace recorded for the $PMAA_{138}$-$PEHMA_{45}$ diblock copolymer using THF eluent containing 4.0% v/v acetic acid.

The z-average particle diameter was found to be 63 nm (± 0.062 nm) according to DLS analysis and 34 nm according to transmission electron microscopy (TEM) studies. The latter technique indicated reasonably uniform spheres, which could be imaged successfully despite the relatively low T_g of the PEHMA block (-10 °C).[198]

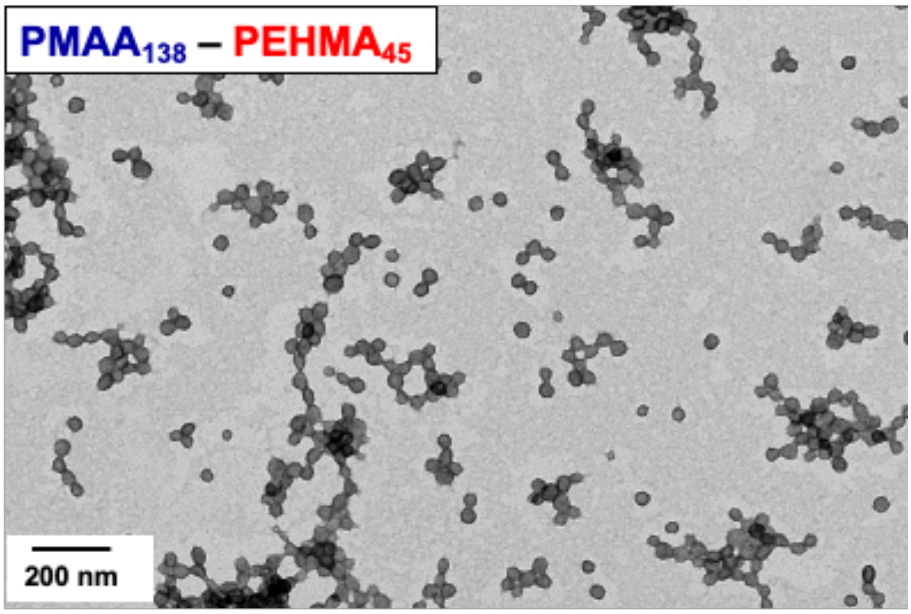

Figure 57. Representative TEM image recorded for $PMAA_{138}$-$PEHMA_{45}$ diblock copolymer nanoparticles prepared by RAFT aqueous emulsion polymerisation of EHMA when targeting 20% w/w solids at pH 2.7.

RAFT aqueous emulsion polymerisations tend to have relatively fast kinetic characteristics.[139,197] In order to determine the time required for the polymerisation to reach completion, kinetic studies were undertaken. Aliquots were extracted at regular time points throughout the polymerisation and the EHMA conversion was determined using ^{1}H NMR spectroscopy by monitoring the attenuation of the vinyl signals at 5.5 and 6.2 ppm relative to that of the aliphatic backbone protons at 0.8 – 2.3 ppm, see Figure 58. These experiments indicated that at least 4 h are required for more than 99% conversion.

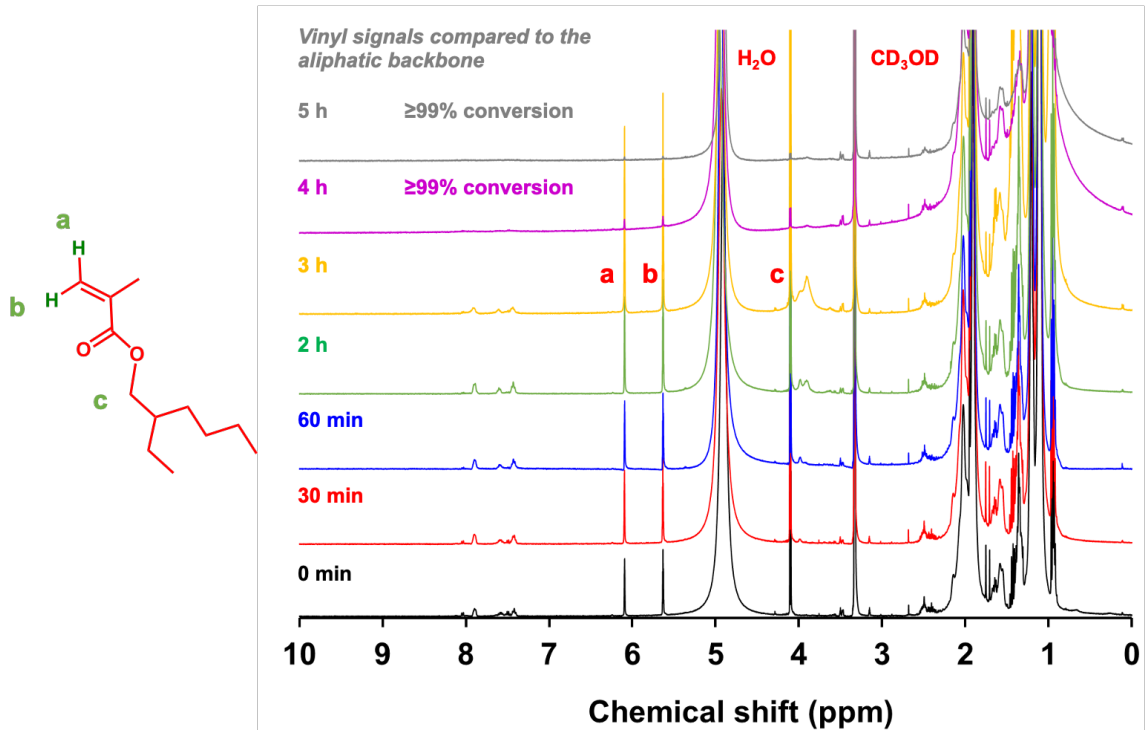

Figure 58. ^{1}H NMR spectra recorded during the synthesis of $PMAA_{138}$-$PEHMA_{45}$ diblock copolymer nanoparticles via RAFT aqueous emulsion polymerisation of EHMA at pH 2.7. Essentially full conversion is achieved within 4 h at 70 °C.

The $PMAA_{138}$-$PEHMA_{45}$ diblock copolymer nanoparticles could only be successfully prepared at pH 2.7. However, aqueous electrophoresis studies indicated only very weakly anionic nanoparticles under such conditions (zeta potentials below –5 mV). As the dispersion pH was increased, the nanoparticles became strongly anionic, exhibiting a zeta potential of around –35 mV at (and above) pH 6. Similar results were reported by Cockram et al.[199] This is because the carboxylic acid groups on the PMAA stabilizer chains become increasingly ionised. Accordingly, the nanoparticle diameter increases slightly owing to electrostatic repulsion between the highly anionic PMAA chains, which leads to a thicker stabiliser layer.

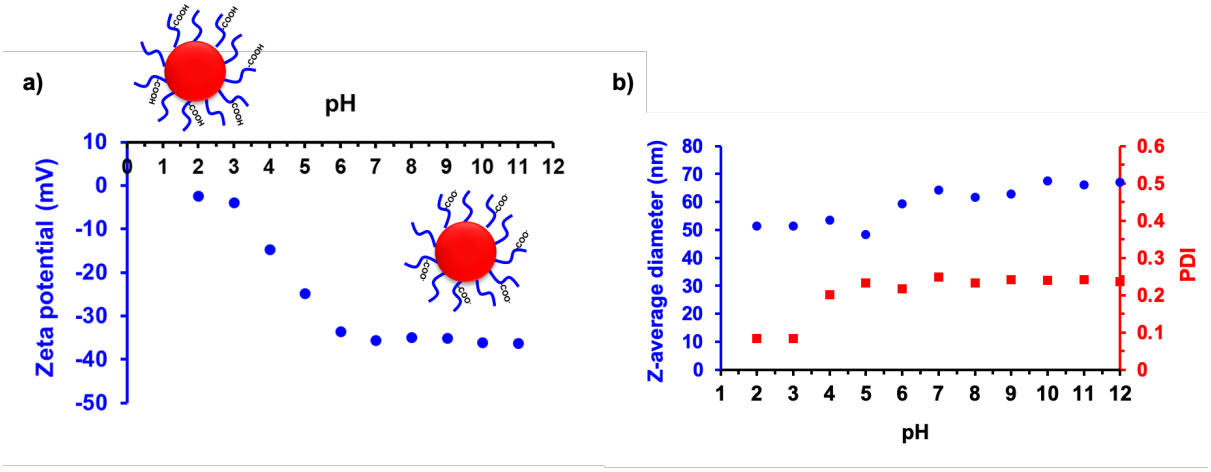

Figure 59. (a) Zeta potential vs. pH curve recorded for $PMAA_{138}$-$PEHMA_{45}$ nanoparticles. (b) Z-average nanoparticle diameter (and DLS polydispersity) vs. pH plot observed for the same nanoparticles.

The $PMAA_{138}$-$PEHMA_{45}$ diblock copolymer was used to prepare a methyl myristate-in-water nanoemulsion with a volume-average droplet diameter of 512 ± 96 nm (as judged by analytical centrifugation). Since the solution pH can vary during occlusion, a zeta potential vs. pH curve was constructed for these nanoemulsion droplets, see Figure 60. A typical occlusion experiment occurs at around pH 9. Under such conditions, the PMAA chains are fully ionised, which leads to a zeta potential of –40 mV. Thus, they can bind strongly to the Ca^{2+} cations located within the growing calcite lattice, which is essential for successful occlusion of the oil droplets.[11]

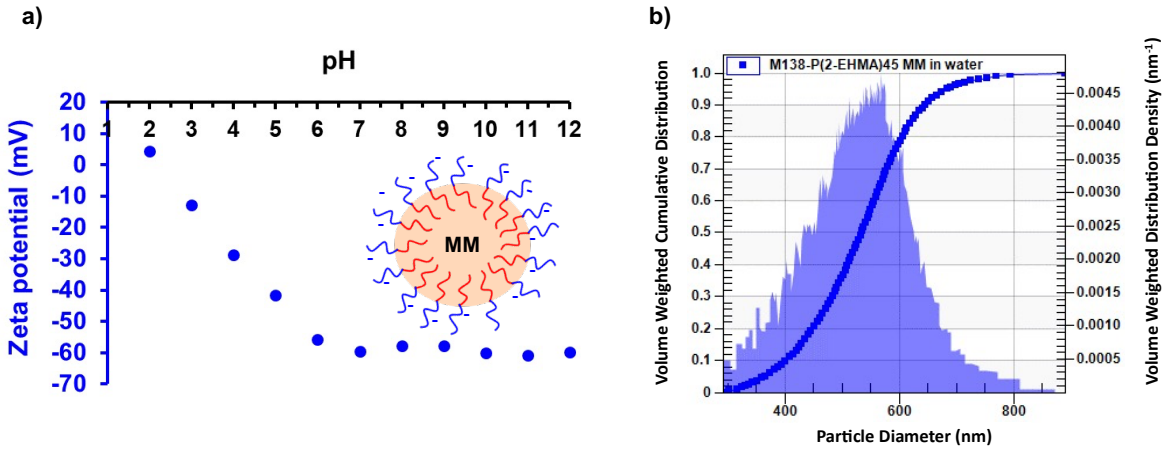

Figure 60. (a) Zeta potential vs. pH curve constructed for a methyl myristate–in–water nanoemulsion stabilised using $PMAA_{138}$-$PEHMA_{45}$ diblock copolymer chains. (b) Droplet size distribution recorded for the same methyl myristate -in-water nanoemulsion (volume-average droplet diameter = 512 ± 96 nm) using analytical centrifugation (LUMiSizer instrument).

Ideally, the amphiphilic diblock copolymer emulsifier used to stabilise nanoemulsions should have universal applicability, i.e. it should be suitable for a range of

multicomponent fragrances. Accordingly, $PMAA_{138}$-$PEHMA_{45}$ was evaluated as an emulsifier for four commercial fragrances: Voyager Zen, Apple Burst 2, Apex and X-RAY 6. As shown in Figure 61, similar mean droplet diameters and standard deviations are obtained in each case. Moreover, the nanoemulsion droplet diameter does not change significantly after ageing for three days at 20 °C. However, there is a discernible increase in the standard deviation (or breadth of the droplet size distribution), which has been reported to be an indication of Ostwald ripening by Thompson and co-workers.[200]

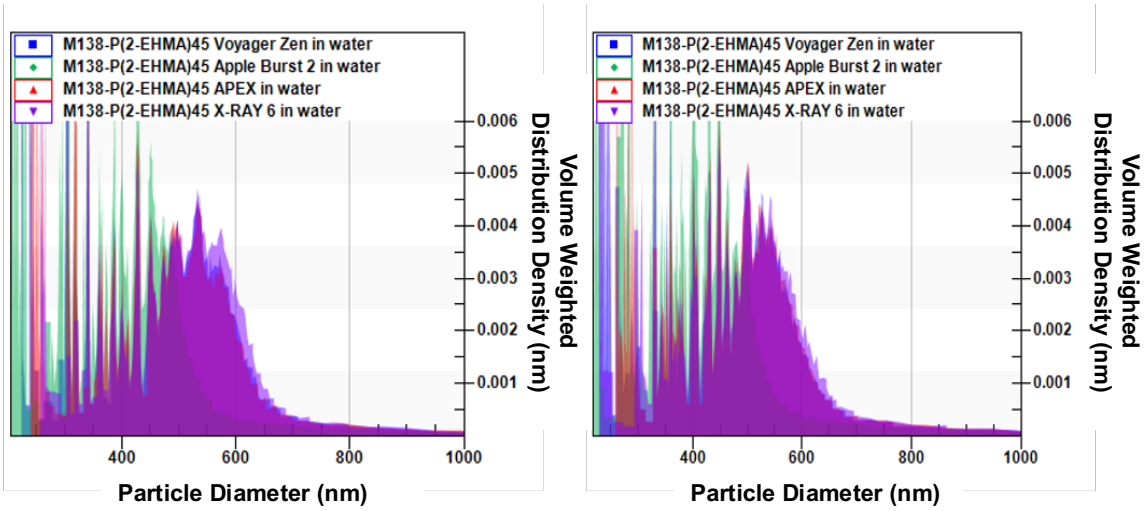

Figure 61. Droplet size distribution determined using the analytical centrifuge for nanoemulsions prepared using the four commercial multi-component fragrances employed in this study: (a) freshly-prepared nanoemulsions and (b) The same nanoemulsions aged for three days at 20 °C.

Table 2. Volume-average droplet diameter determined via analytical centrifugation analysis of o/w nanoemulsions prepared using the four multicomponent fragrances used in this study. Conditions: 6.19 mg $PMAA_{138}$-$PEHMA_{45}$. 30,000 psi, 5 passes, 20 °C

Fragrance	Droplet diameter (nm) Day 1	Droplet diameter (nm) Day 3
Voyager Zen	451 ± 257	451 ± 381
Apple Burst 2	364 ± 207	387 ± 142
APEX	450 ± 213	470 ± 387
X-Ray 6	476 ± 171	463 ± 206

Optical microscopy studies were consistent with conversion of the initial macroemulsion into a nanoemulsion because droplets could no longer be observed after the microfluidisation step, see Figure 62. This is because this imaging technique has limited resolution (~1 μm).

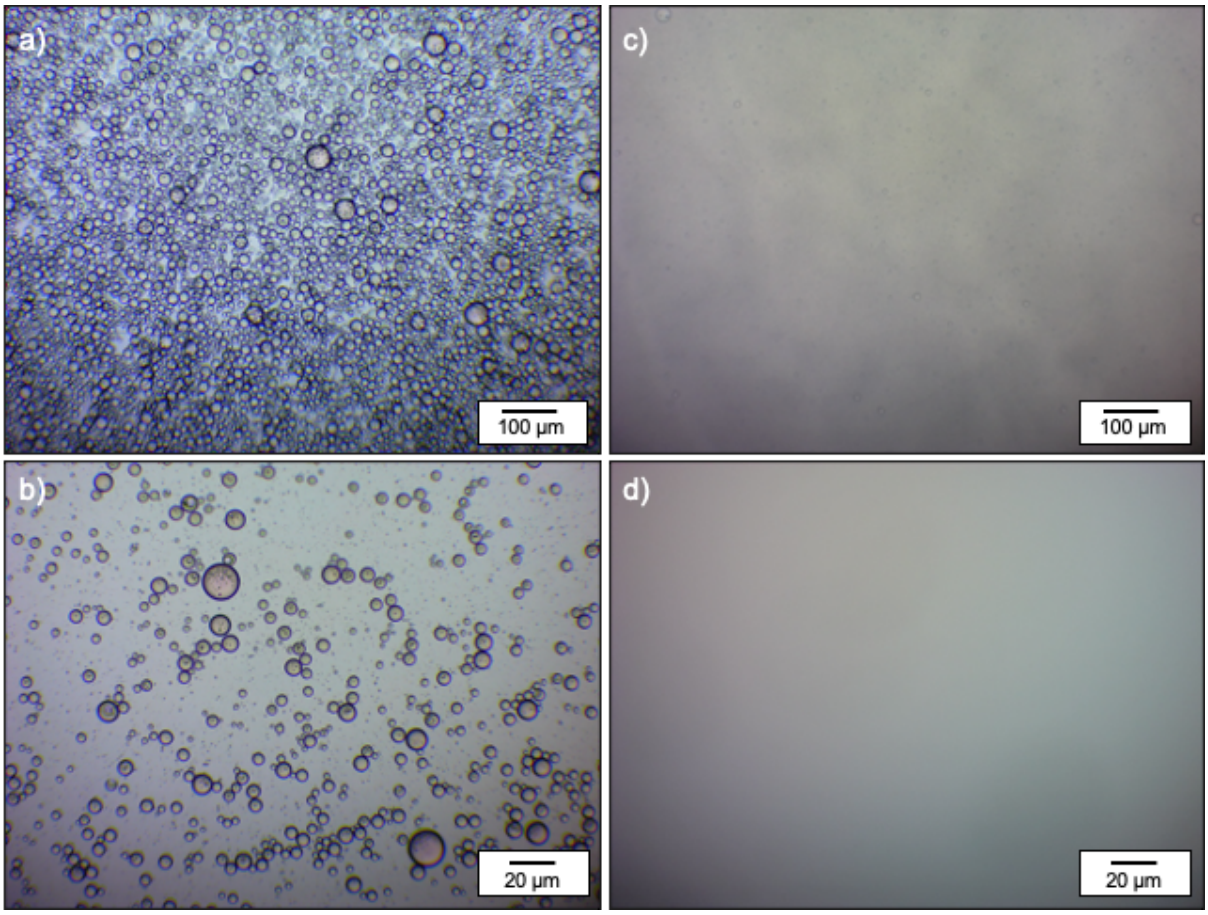

Figure 62. Optical microscopy images obtained for: (a, b) o/w macroemulsion droplets formed after high-shear homogenisation of methyl myristate using 0.10% w/w $PMAA_{138}$-$PEHMA_{45}$ recorded at low and high magnification, respectively; (c, d) o/w nanoemulsion droplets formed after microfluidisation (applied pressure = 30,000 psi, 5 passes) of this precursor macroemulsion recorded at low and high magnification, respectively. The visual absence of any emulsion droplets is consistent with their submicron dimensions.

We hypothesise that the initial sterically-stabilised diblock copolymer nanoparticles undergo *in situ* dissociation during either high-shear homogenisation or (more likely) high-pressure microfluidisation to form molecularly-dissolved diblock copolymer chains. These strongly amphiphilic chains then act as a polymeric surfactant to stabilise the nanoemulsion droplets. The relatively low T_g exhibited by the hydrophobic PEHMA block facilitates such nanoparticle dissociation by conferring high chain mobility at ambient temperature.

To assess whether $PMAA_x$-$PEHMA_y$ diblock copolymers can be used as an environmentally-friendly alternative to $PMAA_x$-$PLMA_y$, a series of oil droplet occlusion experiments were undertaken. Figure 63 shows a series of SEM images acquired for X-RAY 6-occluded crystals at various magnifications. Clearly, the crystal morphology is significantly affected even at just 0.1% $PMAA_{138}$-$PEHMA_{45}$. Such occlusion

behaviour resembles that shown in Figure 43, where the fragrance droplets were was predominantly located at the near-surface of the crystals.

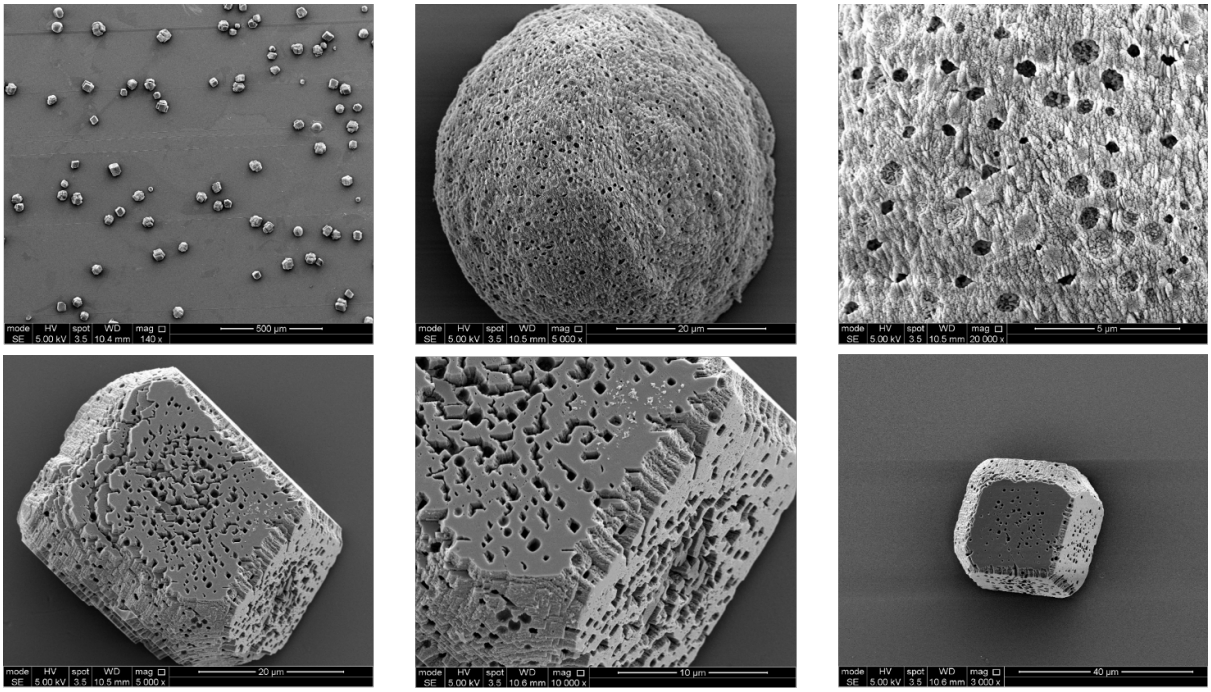

Figure 63. SEM images recorded for calcite crystals obtained after occlusion using the multicomponent fragrance X-RAY 6 as the oil phase. Conditions: 1.5 mM [Ca^{2+}], 6.19 mg $PMAA_{138}$-$PEHMA_{45}$ diblock copolymer emulsifier, at pH 9 and 20 ^{o}C

Owing to the relatively rough crystal morphology, it was difficult to determine whether oil droplet occlusion was confined to the crystal surface. Figure 64 shows a series of SEM images obtained from fractured calcite crystals in order to examine whether there was uniform occlusion. Clearly, there are fewer occluded oil droplets within the centre of the crystals, with occlusion appearing to be confined to within the first few microns of the crystal surface.

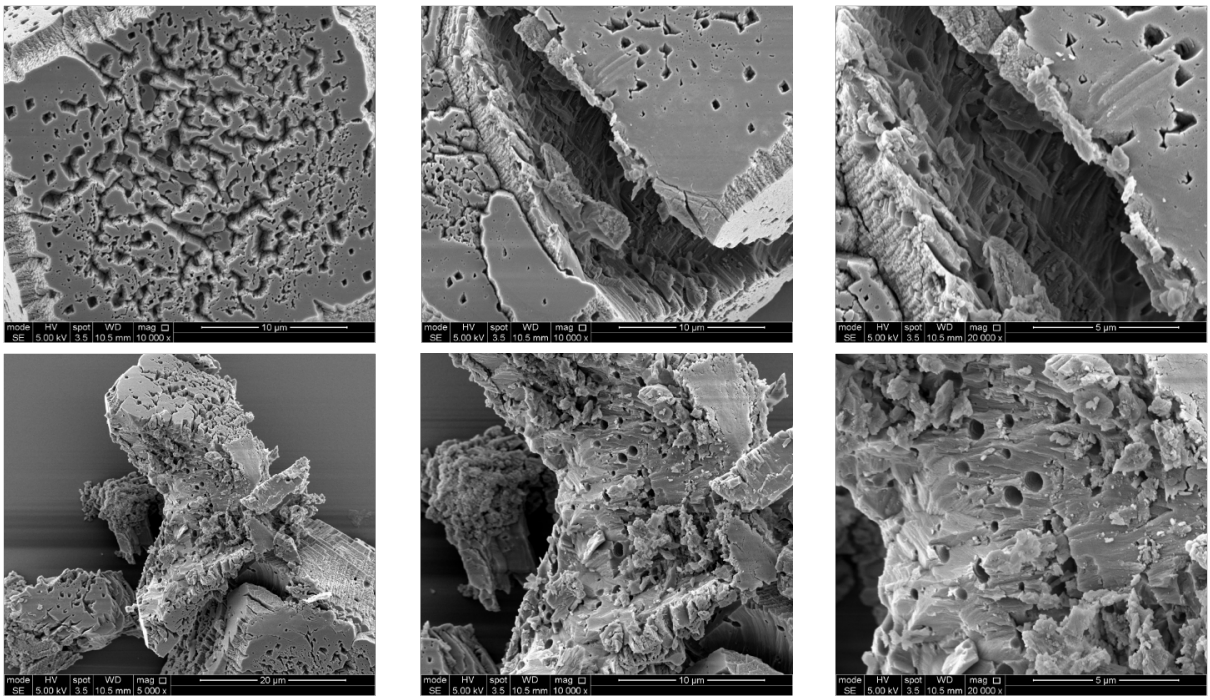

Figure 64. SEM images recorded for fractured calcite crystals obtained after occlusion using the multicomponent fragrance X-RAY 6 as the oil phase. Conditions: 1.5 mM [Ca^{2+}], 6.19 mg $PMAA_{138}$-$PEHMA_{45}$ diblock copolymer emulsifier, at pH 9 and 20 ^{o}C

When the calcium concentration was increased to 10 mM, surface-confined occlusion of large, micron-sized droplets was observed by SEM. As shown in Figure 65, such occlusion was observed for all multicomponent fragrances at higher calcium concentrations. It seems likely that the high salt concentration causes the initial nano-sized oil droplets to undergo partial coalescence, forming micron-sized emulsion droplets that become engulfed within the calcite crystals during crystallisation. This observation is very promising in terms of encapsulating fragrances for laundry applications, as it may be possible to encapsulate larger emulsion droplets within inorganic host crystals.

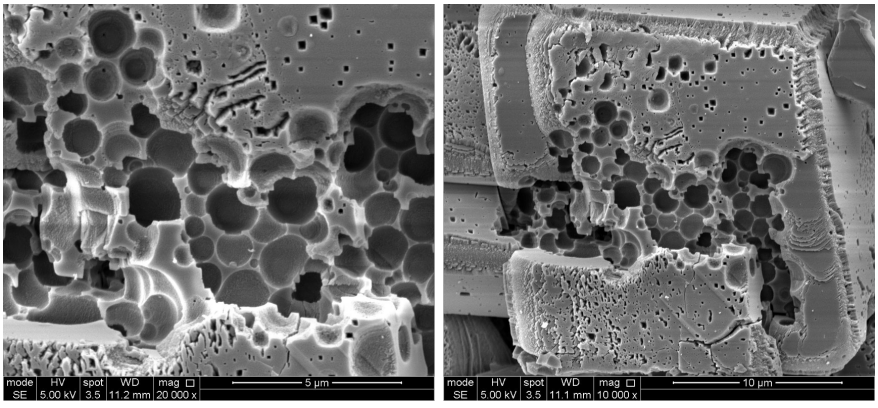

Figure 65. SEM images recorded for fractured calcite crystals obtained after occlusion using the multicomponent fragrance X-RAY 6 as the oil phase. Conditions: 10 mM [Ca^{2+}], 6.19 mg $PMAA_{138}$-$PEHMA_{45}$ diblock copolymer emulsifier, pH 9, 20 ^{o}C

The same occlusion conditions were used for all four multicomponent oils and the extent of oil occlusion achieved was comparable in each case. Owing to the malfunctioning TGA instrument, Apple Burst was used to indicate the occlusion behavior using various calcium concentrations. As shown in Figure 66, the extent of occlusion was found to be 8.3% by mass when using 1.5 mM $CaCl_2$, whereas only 4.3% occlusion was achieved when using 10 mM $CaCl_2$. Presumably, the faster rate of formation of the calcite crystals meant that there was less time for the nano-sized oil droplets to diffuse to and adsorb at the surface of the growing crystals, which is a prerequisite from occlusion.

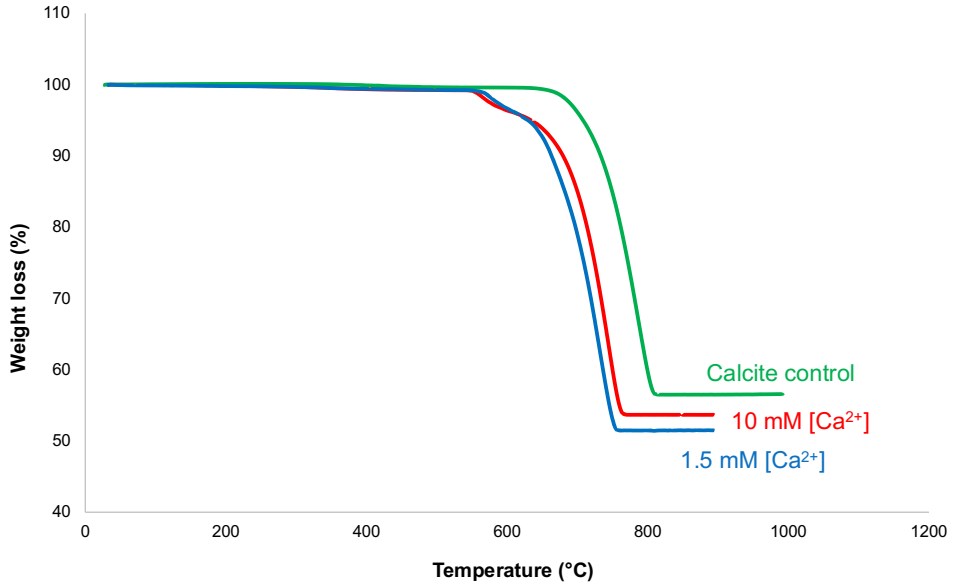

Figure 66. TGA curves recorded for Apple Burst-loaded calcite crystals prepared using 10 mM $CaCl_2$ (red curve) pure calcite (green curve) and 1.5 mM $CaCl_2$ (blue curve).

As shown previously in Figure 45, the extent of occlusion at 10 mM [Ca^{2+}] using $PMAA_{138}$-$PLMA_{45}$ was 4.8% by mass. Thus, $PMAA_{138}$-$PEHMA_{45}$ can be used as an alternative emulsifier for the occlusion of nanoemulsion droplets within calcite crystals, although the crystal morphology is severely affected. Further optimisation of the experimental protocol should improve this fragrance loading, with significantly higher levels being required for laundry applications.

5. CONCLUSION

Strongly amphiphilic $PMAA_{156}$-$PLMA_{45}$ and $PMAA_{138}$-$PLMA_{45}$ diblock copolymers enable the stabilisation of oil-in-water nanoemulsions and the efficient occlusion of such anionic droplets within calcite host crystals. The highest extent of occlusion achieved to date is *ca*. 11 wt% using the ammonia diffusion method at 1.5 mM [Ca^{2+}].[11] A wide range of oils can be occluded within calcite, including multicomponent fragrances, at reasonably high extents of occlusion. These findings are potentially useful in the context of fragrance encapsulation for laundry and other home care applications. However, there are two main issues that still need to be overcome: scalability and higher fragrance occlusion efficiency. It was shown that the ammonia diffusion method can be scaled up to 300 mg, but lower extents of occlusion were observed under such conditions. Using more concentrated nanoemulsions and addition of a highly hydrophobic oil each had a negative impact on the droplet size and stability, thus reducing the extent of occlusion. As a result, this crystal growth protocol appears to be ill-suited for industrial scale-up. Therefore, a new method is required to produce oil-occluded crystals. A direct mixing method was attempted using aqueous solutions of sodium carbonate and calcium chloride but this approach only produced amorphous precipitates. A direct mixing protocol reported in the literature for the formation of spherical vaterite crystals at 25 and 40 °C was briefly investigated but this also proved to be unsuccessful. Lastly, preliminary attempts have been made to coat micron-sized oil or fragrance droplets with a relatively thin shell of calcite. In principle, the Ca^{2+} cations should bind to the anionic stabiliser block, which should aid the deposition process. However, proof-of-concept for this synthetic route has not yet been achieved. In summary, occlusion of fragrance droplets within inorganic host crystals is feasible using an anionic amphiphilic diblock copolymer as an emulsifier. However, scalability and occlusion efficiency remain formidable technical barriers.

Alternative $PMAA_x$-$PEHMA_y$ diblock copolymer nanoparticles were successfully prepared via RAFT aqueous emulsion polymerisation. In principle, this new PISA formulation should enable a wholly aqueous route to oil-loaded calcite crystals to be devised. Reaction conditions were optimised for the synthesis of a $PMAA_{138}$-$PEHMA_{45}$ diblock copolymer because broader MWDs were observed when targeting higher PEHMA DPs. $PMAA_{138}$-$PEHMA_{45}$ stabilised nanoemulsion droplets when using a range of oils, including multicomponent fragrances. Thus, this particular diblock

copolymer can be considered to be a ‘universal’ emulsifier. Mean oil droplet diameters did not differ significantly from those obtained when using $PMAA_{138}$-$PLMA_{45}$. However, differing occlusion behaviour was observed for these two diblock copolymer emulsifiers. At high calcium concentrations, $PMAA_{138}$-$PEHMA_{45}$-stabilised oil droplets became unstable, forming micron-sized droplets that were only incorporated into the surface of the growing host crystals. Interestingly, such droplets are the largest guests to be occluded within calcite. If more efficient occlusion could be achieved, this system could yet prove to be promising for fragrance encapsulation in the context of laundry applications.

6. FUTURE WORK

The two main aims of this project were to significantly increase the extent of occlusion and to establish a method that would be amenable to industrial scale-up. However, as shown by the Flex-SEM images, droplet occlusion is no longer uniform when conducted at higher Ca^{2+} concentration. A reliable protocol is required to prepare more concentrated nanoemulsions that comprise oil volume fractions of at least 0.30. In principle, the deposition of $CaCO_3$, or possibly $Ca_3(PO_4)_2$, as a relatively thick overlayer around micron-sized oil droplets could produce microcapsules containing up to 70-80% oil. There is some literature evidence to suggest that such controlled deposition may be feasible. However, optimum $CaCl_2$ and Na_2CO_3 concentrations would need to be established, as well as the best rate of mixing for these two aqueous solutions.

The calcite form of $CaCO_3$ is the most widely explored morphology owing to its superior stability. However, targeting either vaterite or aragonite may offer some advantages in terms of droplet occlusion. For example, vaterite typically exhibits a spherical morphology, which may aid the deposition of an outer shell or coating layer. Alternatively, $CaSO_4$ and $Ca_3(PO_4)_2$ could be suitable host crystals, although they might require the design of either sulfate or phosphate-functionalised diblock copolymer emulsifiers, respectively.

A fragrance release mechanism for the oil-loaded $CaCO_3$ crystals (or $CaCO_3$-coated oil droplets) is essential for laundry product applications. Ideally, the rate and mode of release must be at least comparable to the microcapsules currently being utilised in commercial formulations. The following three aspects are expected to be important.

(i) Leak resistance under various conditions. The host matrix must be able to retain most of its fragrance for at least two years to ensure an acceptable product shelf-life.

(ii) The host matrix must be mechanically strong enough to withstand washing machine and drying conditions but be sufficiently brittle to undergo rupture via mechanical action after deposition onto fabrics to achieve consumer-activated ‘burst’ release.

(iii) The final product must be resistant to low pH (for fabric conditioners) or high pH (for laundry wash formulations).

In summary, increasing the fragrance loading within the host matrix while examining the scalability of the experimental protocol remain the main technical priorities. From a purely scientific perspective, scaling up the synthesis of the host calcite crystals (or $CaCO_3$-coated oil droplets) should facilitate the deployment of destructive analytical techniques such as thermogravimetric analysis.

7. BIBLIOGRAPHY

1 Top FMCG companies worldwide | Statista, https://www.statista.com/statistics/260963/leading-fmcg-companies-worldwide-based-on-sales/, (accessed May 2020).

2 EU moves to ban microplastics in most products – META, https://meta.eeb.org/2019/01/30/eu-moves-to-ban-microplastics-in-most-products/, (accessed May 2020).

3 EU proposes ban on 90% of microplastic pollutants | Plastics | The Guardian, https://www.theguardian.com/environment/2019/jan/30/eu-european-union-proposes-microplastics-ban-plastic-pollution, (accessed May 2020).

4 F. A. Andersen, *J. Am. Coll. Toxicol.*, 1995, **14**, 373–385.

5 M. Williams, B. Olland, S. P. Armes, P. Verstraete and J. Smets, *J. Colloid Interface Sci.*, 2015, **460**, 71–80.

6 Z. G. Wu, Y. Guo, J. Wang and Y. R. Jia, *Int. J. Mater. Res.*, 2017, **108**, 245–248.

7 G. Nehrke, H. Poigner, D. Wilhelms-Dick, T. Brey and D. Abele, *Geochem. Geophys. Geosyst.*, 2012, doi:10.1029/2011GC003996.

8 M. Galvan-Ruiz, J. Hernandez, L. Banos, J. Noriega-Montes and M. E. Rodriguez-García, *J. Mater. Civ. Eng.*, 2009, **21**, 694–698.

9 B. S. Bageri, M. Mahmoud, A. Abdulraheem, S. H. Al-Mutairi, S. M. Elkatatny and R. A. Shawabkeh, *J. Pet. Sci. Eng.*, 2017, **149**, 476–484.

10 S. S. Sali, M.Tech. Thesis, *Natural calcium carbonate for biomedical applications*, IITB, 2015.

11 Y. Ning, F. C. Meldrum and S. P. Armes, *Chem. Sci.*, 2019, **10**, 8964–8972.

12 P. J. Flory, *Principles of Polymer Chemistry* , Cornell University Press, Ithaca and London, 1953.

13 P. W. Morgan, *J. Macromol. Sci. Part A - Chem.*, 1981, **15**, 1113–1131.

14 T. S. Learner, *Analysis of Modern Paints*, 2006, vol. 51.

15 M. Le Bras and S. Bourbigot, Springer, Dordrecht, 1999.

16 K. L. Edwards, *Mater. Des.*, 1998, **19**, 57–67.

17 J. Kopecek, *J. Polym. Sci. Part A Polym. Chem.*, 2009, **47**, 5929–5946.

18 H. Ghanbari, H. Viatge, A. G. Kidane, G. Burriesci, M. Tavakoli and A. M. Seifalian, *Trends Biotechnol.*, 2009, 27, 359–367.

19 R. O. Ebewele, *Polymer Science and Technology,* CRC Press, New York, 2000.

20 G. Odian, *Principles of Polymerization,* Wiley, New Jersey, 2004.

21 R. G. Gilbert, M. Hess, A. D. Jenkins, R. G. Jones, P. Kratochvil and R. F. T. Stepto, *Pure Appl. Chem.*, 2009, **81**, 351–353.

22 M. Chanda, *Introduction to Polymer Science and Chemistry: A Problem-Solving Approach*, CRC Press, Florida, 2013.

23 J. K. Stille, *J. Chem. Educ.*, 1981, **58**, 862–866.

24 K. Matyjaszewski and T. P. Davis, Eds., *Handbook of Radical Polymerization*, John Wiley & Sons Inc., New Jersey, 2002.

25 P. Nesvadba, *Encyclopedia of Radicals in Chemistry, Biology and Materials*, Wiley, Bologna and Munster, 2012.

26 K. O. Havelka, *ACS Symp. Ser.*, 2000, **755**, 2–10.

27 W. A. Braunecker and K. Matyjaszewski, *Prog. Polym. Sci.*, 2007, **32**, 93–146.

28 J. W. U. Mewshaw and E. Richard, *J. Med. Chem.*, 2007, **50**, 2279–2280.

29 A. Székely and M. Klussmann, *Chem. – An Asian J.*, 2018, **14**, asia.201801636.

30 T. Furuncuoglu, I. Ugur, I. Degirmenci and V. Aviyente, *Macromolecules*, 2010, **43**, 1823–1835.

31 G. Moad, D. H. Solomon, *The chemistry of radical polymerization*, Elsevier, Victoria, 2006.

32 A. D. McNaught and A. Wilkinson, *IUPAC Compendium of Chemical Terminology*, Blackwell Scientific Publications, Oxford, 1997.

33 X. Tian, J. Ding, B. Zhang, F. Qiu, X. Zhuang and Y. Chen, *Polymers*, 2018, **10**, 318.

34 H. L. Hsieh and R. P. Quirk, *Anionic polymerization : principles and practical applications*, CRC Press, Ohio and Oklahoma, 1996.

35 H. Frey and T. Ishizone, *Macromol. Chem. Phys.*, 2017, **218**, 1700217.

36 K. Matyjaszewski, *J. Phys. Org. Chem.*, 1995, **8**, 197–207.

37 M. Szwarc, *Nature*, 1956, **178**, 1168–1169.

38 K. Sugiyama, A. Hirao, J. C. Hsu, Y. C. Tung and W. C. Chen, *Macromolecules*, 2009, **42**, 4053–4062.

39 N. Hadjichristidis and A. Hirao, *Anionic Polymerization: Principles, Practice, Strength, Consequences and Applications*, Springer Japan, Thuwal, 2015.

40 A. Hirao, R. Goseki and T. Ishizone, *Macromolecules*, 2014, **47**, 1883–1905.

41 K. Hong, D. Uhrig and J. W. Mays, *Curr. Opin. Solid State Mater. Sci.*, 1999, **4**, 531–538.

42 M. Morton, *Anionic polymerization : Principles and Practice*, Elsevier, Ohio, 1983.

43 K. Hong, W. Wang and J. W. Mays, in *Reference Module in Materials Science and Materials Engineering*, Elsevier, Amsterdam, 2016.

44 K. Matyjaszewski and J. Spanswick, *Mater. Today*, 2005, **8**, 26–33.

45 N. V Tsarevsky and B. S. Sumerlin, *Fundamentals of Controlled/Living Radical Polymerization*, Royal Society of Chemistry, Cambridge, 2013.

46 J. Chiefari, Y. K. Chong, F. Ercole, J. Krstina, J. Jeffery, T. P. T. Le, R. T. A. Mayadunne, G. F. Meijs, C. L. Moad, G. Moad, E. Rizzardo and S. H. Thang, *Macromolecules*, 1998, **31**, 5559–5562.

47 D. J. Keddie, G. Moad, E. Rizzardo and S. H. Thang, *Macromolecules*, 2012, **45**, 5321–5342.

48 Sigma Aldrich|Raft Polymerization, https://www.sigmaaldrich.com/technical-documents/articles/materials-science/polymer-science/raft-polymerization.html/ (accessed Jan 2021).

49 S. Perrier, *Macromolecules*, 2017, **50**, 7433–7447.

50 C. Barner-Kowollik, M. Buback, B. Charleux, M. L. Coote, M. Drache, T. Fukuda, A. Goto, B. Klumperman, A. B. Lowe, J. B. Mcleary, G. Moad, M. J. Monteiro, R. D. Sanderson, M. P. Tonge and P. Vana, *J. Polym. Sci. Part A Polym. Chem.*, 2006, **44**, 5809–5831.

51 J. Skey and R. K. O'Reilly, *Chem. Commun.*, 2008, **35**, 4183-4185.

52 G. Moad, E. Rizzardo and S. H. Thang, *Aust. J. Chem*, 2005, **58**, 379–410.

53 R. T. A. Mayadunne, E. Rizzardo, J. Chiefari, J. Krstina, G. Moad, A. Postma and S. H. Thang, *Macromolecules*, 2000, **33**, 243–245.

54 M. Destarac, D. Charmot, X. Franck and S. Z. Zard, *Macromol. Rapid Commun.*, 2000, **21**, 1035-1039.

55 R. Francis and A. Ajayaghosh, *Macromolecules*, 2000, **33**, 4699–4704.

56 H. Willcock and R. K. O'Reilly, *Polym. Chem.*, 2010, **1**, 149–157.

57 J. Phommalysack-Lovan, Y. Chu, C. Boyer and J. Xu, *Chem. Commun*, 2018, **54**, 6591.

58 G. Moad, E. Rizzardo and S. H. Thang, *Chem. - An Asian J.*, 2013, **8**, 1634–1644.

59 G. Moad, E. Rizzardo and S. H. Thang, *Aust. J. Chem.*, 2009, **62**, 1402–1472.

60 G. Moad, E. Rizzardo and S. H. Thang, *Polymer Science: A Comprehensive Reference*, 2012, **3**, 181-226.

61 N. J. Warren and S. P. Armes, *J. Am. Chem. Soc.*, 2014, **136**, 10174–10185.

62 M. Morton, *J. Macromol. Sci. Part A - Chem.*, 1981, **15**, 1289–1302.

63 H. Naidus, *Ind. Eng. Chem.*, 1953, **45**, 712–717.

64 R. Jovanović and M. A. Dubé, *J. Macromol. Sci. Part C Polym. Rev.*, 2004, **44**, 1–51.

65 L. D. A. Rodrigues, C. R. Hurtado, E. F. Macedo, D. B. Tada, L. M. Guerrini and M. P. Oliveira, *Prog. Org. Coatings*, 2020, **145**, 105693.

66 W. D. Harkins, *J. Chem. Phys.*, 1945, **13**, 381–382.

67 P. A. Lovell and F. J. Schork, *Biomacromolecules*, 2020, **21**, 4396–4441.

68 R. J. Hunter, *Introduction to Modern Colloid Science*, Oxford University Press, Oxford, 1993.

69 W. J. Priest, *J. Phys. Chem.*, 1952, **56**, 1077–1082.

70 R. M. Fitch and C. H. Tsai, *Proc. Nat. Acad. Sci.*, 1967, **64**, 1424–1425.

71 W. D. Harkins, *J. Chem. Phys.*, 1945, **13**, 381–382.

72 P. A. Lovell and M. S. El-Aasser, *Emulsion Polymerization and Emulsion Polymers*, Wiley, Manchester, 1997.

73 H. Warson, *Polym. Int.*, 2003, **41**, 352–352.

74 J. Zhou, H. Yao and J. Ma, *Polym. Chem.*, 2018, **9**, 2532–2561.

75 P. Alexandidis and B. Lindman, *Amphiphilic Block Copolymers Self-Assembly and Applications*, Elsevier, Amsterdam, 2000.

76 D. Chandler, *Nature*, 2005, **437**, 640–647.

77 G. M. Whitesides and B. Grzybowski, *Science*, 2002, **295**, 2418–2421.

78 L. L. Schramm, E. N. Stasiuk and D. G. Marangoni, *Annu. Reports Prog. Chem. - Sect. C*, 2003, **99**, 3–48.

79 J. N. Israelachvili, *Intermolecular and Surface Forces*, Elsevier, California, 2011.

80 D. Lombardo, M. A. Kiselev, S. Magazu and P. Calandra, *Advances in Condensed Matter Physics*, 2015, **2015,** 1-22.

81 J. N. Israelachvili, *Thermodynamic and geometric aspects of amphiphile aggregation into micelles, vesicles and bilayers, and the interactions between them*, Physics of Amphiphiles: Micelles, Vesicles and Microemulsions, Amsterdam, 1985.

82 M. Szwarc, *Nature*, 1956, **178**, 1168-1169.

83 M. Szwarc, M. Levy and R. Milkovich, *J. Am. Chem. Soc.*, 1956, **78,** 2656–2657.

84 Y. Mai and A. Eisenberg, *Chem. Soc. Rev*, 2012, **41**, 5969–5985.

85 N. S. Cameron, M. K. Corbierre and A. Eisenberg, *Can. J. Chem.*, 1999, **77**, 1311–1326.

86 X. Wang and Z. An, *Macromol. Rapid Commun.*, 2019, **40**, 1800325.

87 U. Tritschler, S. Pearce, J. Gwyther, G. R. Whittell and I. Manners, *Macromolecules*, 2017, **50**, 3439–3463.

88 D. Zhou, S. Dong, R. P. Kuchel, S. Perrier and P. B. Zetterlund, *Polym. Chem.*, 2017, **8**, 3082–3089.

89 S. L. Canning, G. N. Smith and S. P. Armes, *Macromolecules*, 2016, **49**, 1985–2001.

90 A. Blanazs, A. J. Ryan and S. P. Armes, *Macromolecules*, 2012, **45**, 5099–5107.

91 C. György, M. J. Derry, E. J. Cornel and S. P. Armes, *Macromolecules*, 2021, **54**, 1159–1169.

92 C. György, S. J. Hunter, C. Girou, M. J. Derry and S. P. Armes, *Polym. Chem.*, 2020, **11**, 4579–4590.

93 N. J. W. Penfold, J. R. Lovett, P. Verstraete, J. Smets and S. P. Armes, *Polym. Chem.*, 2017, **8**, 272–282.

94 S. J. Byard, M. Williams, B. E. McKenzie, A. Blanazs and S. P. Armes, *Macromolecules*, 2017, **50**, 1482–1493.

95 E. Groison, S. Brusseau, F. D'Agosto, S. Magnet, R. Inoubli, L. Couvreur and B. Charleux, *ACS Macro Lett.*, 2012, **1**, 47–51.

96 S. Brusseau, F. D'Agosto, S. Magnet, L. Couvreur, C. Chamignon and B. Charleux, *Macromolecules*, 2011, **44**, 5590–5598.

97 G. Delaittre, J. Nicolas, C. Lefay, M. Save and B. Charleux, *Chem. Commun.*, 2005, 614.

98 K. H. Kim, J. Kim and W. H. Jo, *Polymer (Guildf).*, 2005, **46**, 2836–2840.

99 S. Sugihara, S. P. Armes and A. L. Lewis, *Angew. Chemie Int. Ed.*, 2010, **49**, 3500–3503.

100 I. Y. Ma, E. J. Lobb, N. C. Billingham, S. P. Armes, A. L. Lewis, A. W. Lloyd and J. Salvage, *Macromolecules*, 2002, **35**, 9306–9314.

101 Y. Li and S. P. Armes, *Angew. Chemie Int. Ed.*, 2010, **49**, 4042–4046.

102 G. Moad, E. Rizzardo and S. H. Thang, *Aust. J. Chem*. 2006, **59**, 669–692.

103 J. Rieger, *Macromol. Rapid Commun.*, 2015, **36**, 1458–1471.

104 B. Charleux, G. Delaittre, J. Rieger and F. D'Agosto, *Macromolecules*, 2012, **45**, 6753–6765.

105 J. T. Sun, C. Y. Hong and C. Y. Pan, *Polym. Chem.*, 2013, **4**, 873–881.

106 J. T. Sun, C. Y. Hong and C. Y. Pan, *Soft Matter*, 2012, **8**, 7753-7767.

107 M. J. Derry, L. A. Fielding and S. P. Armes, *Prog. Polym. Sci.*, 2016, **52**, 1–18.

108 Y. K. Chong, T. P. T. Le, G. Moad, E. Rizzardo and S. H. Thang, *Macromolecules*, 1999, **32**, 2071–2074

109 M. R. Hill, R. N. Carmean and B. S. Sumerlin, *Macromolecules*, 2015, **48**, 5459–5469.

110 G. Moad, J. Chiefari, YK Chong, J. Krstina, R. T. A. Mayadunne, A. Postma, E. Rizzardo and S. H. Thang, *Polym. Int.*, 2000, **49**, 993–1001.

111 S. P. Armes, S. Perrier and P. B. Zetterlund, *Polym. Chem.*, 2021, **12**, 8–11.

112 S. Boisse, J. Rieger, K. Belal, A. Di-Cicco, P. Beaunier, M. H. Li and B.

Charleux, *Chem. Commun.*, 2010, **46**, 1950.

113 M. Semsarilar, E. R. Jones, A. Blanazs and S. P. Armes, *Adv. Mater.*, 2012, **24**, 3378–3382.

114 L. A. Fielding, J. A. Lane, M. J. Derry, O. O. Mykhaylyk and S. P. Armes, *J. Am. Chem. Soc.*, 2014, **136**, 5790–5798.

115 L. Houillot, C. Bui, M. Save, B. Charleux, C. Farcet, C. Moire, J. A. Raust and I. Rodriguez, *Macromolecules*, 2007, **40**, 6500–6509.

116 E. R. Jones, M. Semsarilar, A. Blanazs and S. P. Armes, *Macromolecules*, 2012, **45**, 5091–5098.

117 M. Semsarilar, V. Ladmiral, A. Blanazs and S. P. Armes, *Polym. Chem.*, 2014, **5**, 3466–3475.

118 M. Semsarilar, N. J. W. Penfold, E. R. Jones and S. P. Armes, *Polym. Chem.*, 2015, **6**, 1751–1757.

119 W. Zhao, G. Gody, S. Dong, P. B. Zetterlund and S. Perrier, *Polym. Chem.*, 2014, **5**, 6990–7003.

120 X. Zhang, J. Rieger and B. Charleux, *Polym. Chem.*, 2012, **3**, 1502.

121 W. M. Wan and C. Y. Pan, *Macromolecules*, 2010, **43**, 2672–2675.

122 W. M. Wan, X. L. Sun and C. Y. Pan, *Macromol. Rapid Commun.*, 2010, **31**, 399–404.

123 A. P. Lopez-Oliva, N. J. Warren, A. Rajkumar, O. O. Mykhaylyk, M. J. Derry, K. E. B. Doncom, M. J. Rymaruk and S. P. Armes, *Macromolecules*, 2015, **48**, 3547–3555.

124 Q. Zhang and S. Zhu, *ACS Macro Lett.*, 2015, **4**, 755–758.

125 M. J. Derry, L. A. Fielding and S. P. Armes, *Polym. Chem.*, 2015, **6**, 3054–3062.

126 R. C. Hayward and D. J. Pochan, *Macromolecules*, 2010, **43**, 3577–3584.

127 M. Semsarilar, V. Ladmiral, A. Blanazs and S. P. Armes, *Langmuir*, 2012, **28**, 914–922.

128 I. Uzulina, S. Kanagasabapathy and J. Claverie, *Macromol. Symp.*, 2000, **150**, 33–39.

129 D. E. Ganeva, E. Sprong, H. De Bruyn, G. G. Warr, C. H. Such and B. S. Hawkett, *Macromolecules*, 2007, **40**, 6181–6189.

130 C. J. Ferguson, R. J. Hughes, B. T. T. Pham, B. S. Hawkett, R. G. Gilbert, A. K. Serelis and C. H. Such, *Macromolecules*, 2002, **35**, 9243–9245.

131 C. J. Ferguson, R. J. Hughes, D. Nguyen, B. T. T. Pham, R. G. Gilbert, A. K. Serelis, C. H. Such and B. S. Hawkett, *Macromolecules*, 2005, **38**, 2191–2204.

132 S. Boissé, J. Rieger, G. Pembouong, P. Beaunier and B. Charleux, *J. Polym. Sci. Part A Polym. Chem.*, 2011, **49**, 3346–3354.

133 I. Chaduc, W. Zhang, J. Rieger, M. Lansalot, F. D'Agosto and B. Charleux, *Macromol. Rapid Commun.*, 2011, **32**, 1270–1276.

134 M. Manguian, M. Save and B. Charleux, *Macromol. Rapid Commun.*, 2006, **27**, 399–404.

135 J. Rieger, W. Zhang, F. Stoffelbach and B. Charleux, *Macromolecules*, 2010, **43**, 6302–6310.

136 J. Rieger, G. Osterwinter, C. Bui, F. Stoffelbnach and B. Charleux, *Macromolecules*, 2009, **42**, 5518–5525.

137 J. Rieger, F. Stoffelbach, C. Bui, D. Alaimo, C. Jerome and B. Charleux, *Macromolecules*, 2008, **41**, 4065–4068.

138 X. Zhang, S. Boisse, W. Zhang, P. Beaunier, F. D'Agosto, J. Rieger and B. Charleux, *Macromolecules*, 2011, **44**, 4149–4158.

139 V. J. Cunningham, A. M. Alswieleh, K. L. Thompson, M. Williams, G. J. Leggett, S. P. Armes and O. M. Musa, *Macromolecules*, 2014, **47,** 5613–5623.

140 X. Zhang, J. Rieger and B. Charleux, *Polym. Chem.*, 2012, **3**, 1502–1509.

141 S. Binauld, L. Delafresnaye, B. Charleux, F. D'Agosto and M. Lansalot, *Macromolecules*, 2014, **47**, 3461–3472.

142 B. Akpinar, L. A. Fielding, V. J. Cunningham, Y. Ning, O. O. Mykhaylyk, P. W. Fowler and S. P. Armes, *Macromolecules*, 2016, **49**, 5160–5171.

143 C. P. Jesson, V. J. Cunningham, M. J. Smallridge and S. P. Armes, *Macromolecules*, 2018, **51**, 3221–3232.

144 E. E. Brotherton, F. L. Hatton, A. A. Cockram, M. J. Derry, A. Czajka, E. J. Cornel, P. D. Topham, O. O. Mykhaylyk and S. P. Armes, *J. Am. Chem. Soc.*, 2019, **141**, 13664–13675.

145 F. L. Hatton, J. R. Lovett and S. P. Armes, *Polym. Chem.*, 2017, **8**, 4856–4868.

146 W. Zhang, F. D'Agosto, P. Y. Dugas, J. Rieger and B. Charleux, *Polymer*, 2013, **54**, 2011–2019.

147 I. Chaduc, A. Crepet, O. Boyron, B. Charleux, F. D'Agosto and M. Lansalot, *Macromolecules*, 2013, **46**, 6013–6023.

148 M. Mertoglu, A. Laschewsky, K. Skrabania and C. Wieland, *Macromolecules*, 2005, **38**, 3601–3614.

149 D. B. Thomas, A. J. Convertine, R. D. Hester, A. B. Lowe and C. L. McCormick, *Macromolecules*, 2004, **37**, 1735–1741.

150 W. Zhang, F. D'Agosto, O. Boyron, J. Rieger and B. Charleux, *Macromolecules*, 2011, **44**, 7584–7593.

151 I. Chaduc, M. Girod, R. Antoine, B. Charleux, F. D'Agosto and M. Lansalot, *Macromolecules*, 2012, **45**, 5881–5893.

152 W. Zhang, F. D'Agosto, O. Boyron, J. Rieger and B. Charleux,

Macromolecules, 2012, **45**, 4075–4084.

153 A. Y. Khan, S. Talegaonkar, Z. Iqbal, F. J. Ahmed and R. K. Khar, *Curr. Drug Deliv.*, 2006, **3**, 429–43.

154 R. Marquez, A. M. Forgiarini, D. Langevin and J. L. Salager, *Langmuir*, 2018, **34**, 9252–9263.

155 H. A. Lieberman, M. M. Rieger and G.S. Banker, *Pharmaceutical Dosage Forms: Disperse Systems*, CRC Press, Boca Raton, 1998

156 F. Leal-Calderon, V. Schmitt and J. Bibette, *Emulsion science: basic principles*, Springer, New York, 2007.

157 K. L. Thompson, N. Cinotti, E. R. Jones, C. J. Mable, P. W. Fowler and S. P. Armes, *Langmuir*, 2017, **33**, 12616–12623.

158 D. J. McClements, L. Bai and C. Chung, *Annu. Rev. Food Sci. Technol.*, 2017, **8**, 205–236.

159 Y. Ding, M. Cai, Z. Cui, L. Huang, L. Wang, X. Lu and Y. Cai, *Angew. Chemie Int. Ed.*, 2018, **57**, 1053–1056.

160 J. C. Foster, S. Varlas, B. Couturaud, J. R. Jones, R. Keogh, R. T. Mathers and R. K. O'Reilly, *Angew. Chemie Int. Ed.*, 2018, **57**, 15733–15737.

161 G. Mellot, J. M. Guigner, L. Bouteiller, F. Stoffelbach and J. Rieger, *Angew. Chemie Int. Ed.*, 2019, **58**, 3173–3177.

162 A. B. Lowe, *Polymer*, 2016, **106**, 161–181.

163 C. E. Boott, J. Gwyther, R. L. Harniman, D. W. Hayward and I. Manners, *Nat. Chem.*, 2017, **9**, 785–792.

164 F. Lv, Z. An and P. Wu, *Nat. Commun.*, 2019, **10**, 1397.

165 P. Yang, Y. Ning, T. J. Neal, E. R. Jones, B. R. Parker and S. P. Armes, *Chem. Sci.*, 2019, **10**, 4200–4208.

166 J. Yeow and C. Boyer, *Adv. Sci.*, 2017, **4**, 1700137.

167 B. P. Binks, *Current Opinion in Colloid & Interface Science,* 2002, **7**, 21-41.

168 M. Douverne, Y. Ning, A. Tatani, F. C. Meldrum and S. P. Armes, *Angew. Chemie Int. Ed.*, Angew. Chem. Int. Ed., 2019, **58**, 8692–8697.

169 Y. Ning, L. A. Fielding, L. P. D. Ratcliffe, Y. W. Wang, F. C. Meldrum and S. P. Armes, *J. Am. Chem. Soc.*, 2016, **138**, 11734–11742.

170 F. Nudelman and N. A. J. M. Sommerdijk, *Angew. Chemie Int. Ed.*, 2012, **51**, 6582–6596.

171 H. A. Lowenstam and S. Weiner, *On biomineralization*, Oxford University Press, Oxford, 1989.

172 M. Ukita, K. Toyoura, A. Nakamura and K. Matsunaga, *J. Appl. Phys.*, 2016, **120**, 142118.

173 M. M. H. Al Omari, I. S. Rashid, N. A. Qinna, A. M. Jaber and A. A. Badwan,

Profiles Drug Subst. Excipients Relat. Methodol., 2016, **41**, 31–132.

174 S. Weiner and L. Addadi, *J. Mater. Chem.*, 1997, **7**, 689–702.

175 A. Berman, J. Hanson, L. Leiserowitz, T. F. Koetzle, S. Weiner and L. Addadi, *Science*, 1993, **259**, 776–779.

176 Calcium Carbonate – $CaCO_3$ – Polymorphs, https://www.chemtube3d.com/ss-caco3/, (accessed January 2021).

177 C. Lu, L. Qi, H. Cong, X. Wang, J. Yang, L. Yang, D. Zhang, J. Ma and W. Cao, *Chem. Mater.*, 2005, **17**, 5218–5224.

178 Y. Y. Kim, M. Semsarilar, J. D. Carloni, K. R. Cho, A. N. Kulak, I. Polishchuk, C. T. Hendley, P. J. M. Smeets, L. A. Fielding, B. Pokroy, C. C. Tang, L. A. Estroff, S. P. Baker, S. P. Armes and F. C. Meldrum, *Adv. Funct. Mater.*, 2016, **26**, 1382–1392.

179 Y. Y. Kim, K. Ganesan, P. Yang, A. N. Kulak, S. Borukhin, S. Pechook, L. Ribeiro, R. Kröger, S. J. Eichhorn, S. P. Armes, B. Pokroy and F. C. Meldrum, *Nat. Mater.*, 2011, **10**, 890–896.

180 Y. Ning, L. Han, M. J. Derry, F. C. Meldrum and S. P. Armes, *J. Am. Chem. Soc.*, 2019, **141**, 2557–2567.

181 A. Herrmann, *Angew. Chemie Int. Ed.*, 2007, **46**, 5836–5863.

182 A. M. Bakry, S. Abbas, B. Ali, H. Majeed, M. Y. Abouelwafa, A. Mousa and L. Liang, *Compr. Rev. Food Sci. Food Saf.*, 2016, **15**, 143–182.

183 A. Madene, M. Jacquot, J. Scher and S. Desobry, *Int. J. Food Sci. Technol.*, 2006, **41**, 1–21.

184 H. Lee, C. H. Choi, A. Abbaspourrad, C. Wesner, M. Caggioni, T. Zhu and D. A. Weitz, *ACS Appl. Mater. Interfaces*, 2016, **8**, 4007–4013.

185 L. He, J. Hu and W. Deng, *Polym. Chem.*, 2018, **9**, 4926–4946.

186, C. Wandrey, A. Bartkowiak and S. E. Harding, *Materials for Encapsulation*, Springer, New York, 2010.

187 C. H. Xue, L. Y. Deng, S. T. Jia and P. B. Wei, *RSC Adv.*, 2016, **6**, 107364–107369.

188 F. L. Sousa, S. Horta, M. Santos, S. M. Rocha and T. Trindade, *Results Pharma Sci.*, 2012, **2**, 52–6.

189 B. Duncan, X. Li, R. F. Landis, S. T. Kim, A. Gupta, L.-S. Wang, R. Ramanathan, R. Tang, J. A. Boerth and V. M. Rotello, *ACS Nano*, 2015, **9**, 7775–7782.

190 Y. Zhao, Y. Li, D. E. Demco, X. Zhu and M. Möller, *Langmuir*, 2014, **30**, 4253–4261.

191 T. Bollhorst, K. Rezwan and M. Maas, *Chem. Soc. Rev.*, 2017, **46**, 2091–2126.

192 X. Wang, W. Zhou, J. Cao, W. Liu and S. Zhu, *J. Colloid Interface Sci.*, 2012, **372**, 24–31.

193 F. C. Meldrum and H. Cölfen, *Chem. Rev.*, 2008, 108, 4332–4432.

194 J. Ihli, P. Bots, A. Kulak, L. G. Benning and F. C. Meldrum, *Adv. Funct. Mater.*, 2013, **23**, 1965–1973.

195 A. A. Cockram, R. D. Bradley, S. A. Lynch, P. C. D. Fleming, N. S. J. Williams, M. W. Murray, S. N. Emmett and S. P. Armes, *React. Chem. Eng.*, 2018, **3**, 645–657.

196 S. Rimmer and P. Tattersall, *Polymer,* 1999, **40**, 5729-5731.

197 A. Cockram, PhD Thesis, *Novel Block Copolymer Nanoparticles via RAFT Aqueous Emulsion Polymerization***,** University of Sheffield, 2018.

198 Thermal Transitions of Homopolymers | Sigma-Aldrich, https://www.sigmaaldrich.com/technical-documents/articles/materials-science/polymer-science/thermal-transitions-of-homopolymers.html, (accessed 31 January 2021).

199 A. A. Cockram, T. J. Neal, M. J. Derry, O. O. Mykhaylyk, N. S. J. Williams, M. W. Murray, S. N. Emmett and S. P. Armes, *Macromolecules*, 2017, **50**, 796–802.

200 K. L. Thompson, M. J. Derry, F. L. Hatton and S. P. Armes, *Langmuir*, 2018, **34**, 9289–9297.

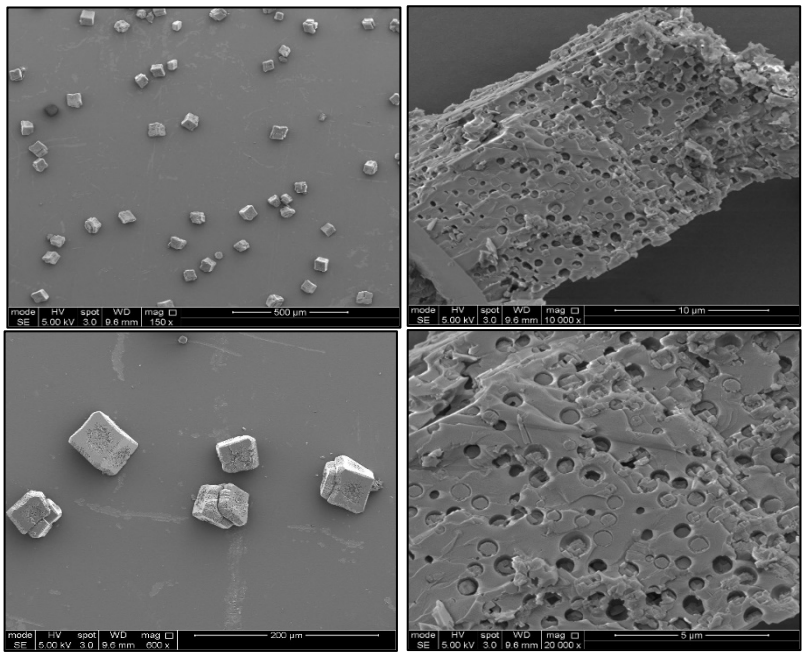

Figure A1. SEM images recorded for fractured calcite crystals obtained after occlusion using the multicomponent fragrance Apple Burst 2 as the oil phase. Conditions: 1.5 mM [Ca^{2+}], 5.07x10^{-7} mol of $PMAA_{156}$-$PLMA_{45}$ diblock copolymer emulsifier, pH 9, 20 ^{o}C

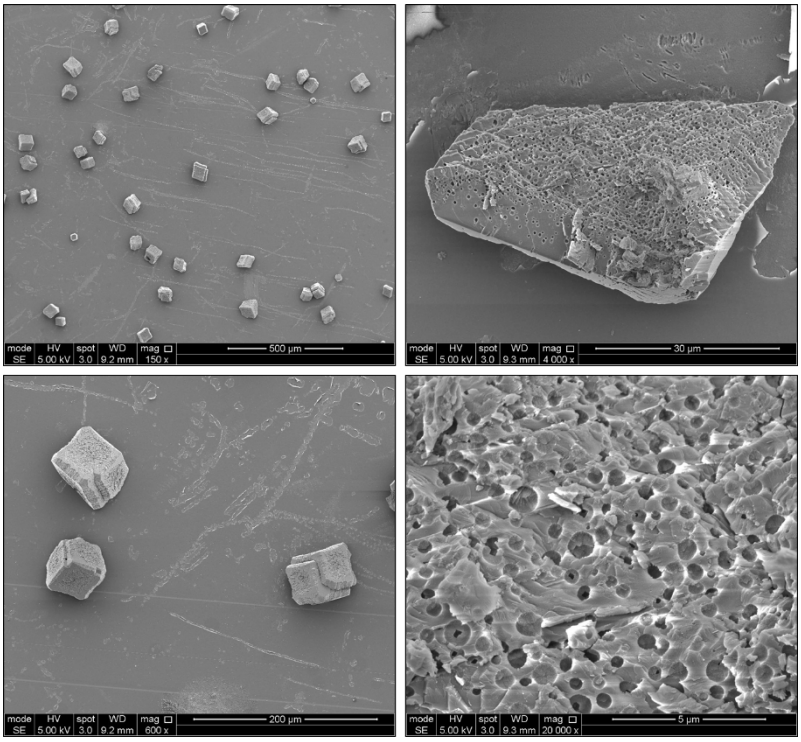

Figure A2. SEM images recorded for fractured calcite crystals obtained after occlusion using the multicomponent fragrance APEX as the oil phase. Conditions: 1.5 mM [Ca^{2+}], 5.07x10^{-7} mol of $PMAA_{156}$-$PLMA_{45}$ diblock copolymer emulsifier, pH 9, 20 ^{o}C

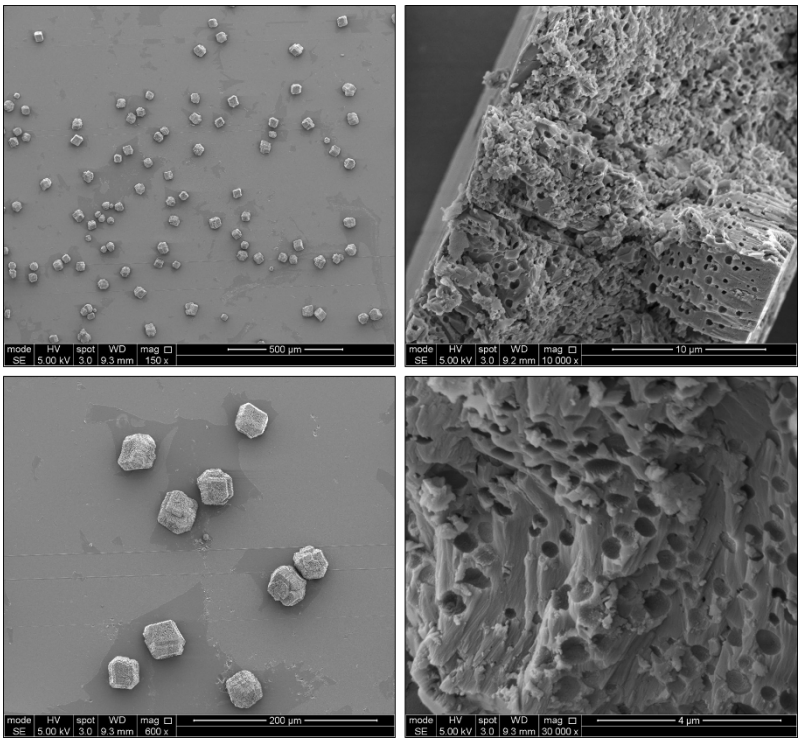

Figure A3. SEM images recorded for fractured calcite crystals obtained after occlusion using the multicomponent fragrance X-RAY 6 as the oil phase. Conditions: 1.5 mM [Ca^{2+}], 5.07x10^{-7} mol of $PMAA_{156}$-$PLMA_{45}$ diblock copolymer emulsifier, pH 9, 20 ^{o}C

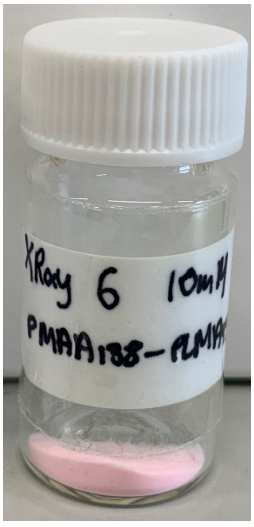

Figure A4. Calcite crystals collected after crystallisation using 10 mM [Ca^{2+}], 11.9 mg $PMAA_{138}$-$PLMA_{45}$ and X-RAY 6 as the oil phase. The pink hue indicates successful oil occlusion within these crystals.

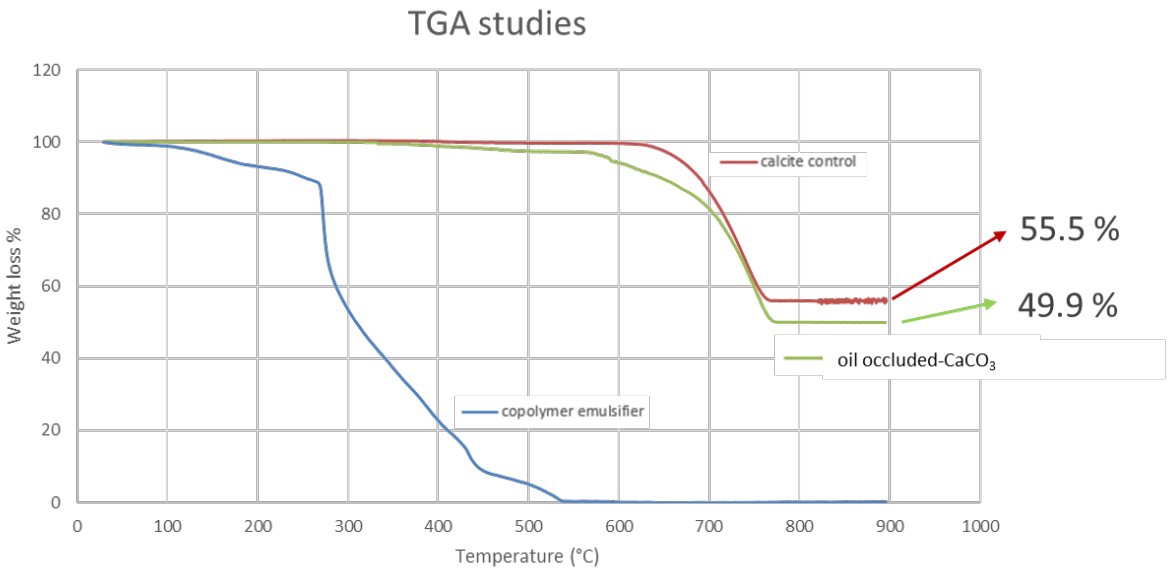

Figure A5. TGA curves recorded for Apple Burst 2-loaded calcite crystals prepared using 1.5 mM $CaCl_2$ (green curve) using $5.07x10^{-7}$ mol of $PMAA_{156}$-$PLMA_{45}$, pure calcite (red curve) and the $PMAA_{138}$-$PLMA_{45}$ diblock copolymer alone (blue curve).

Green spectrum is showing mainly Calcite
Blue spectrum is showing calcite + Fragrance peaks (carbonyl, C-H stretching and Aromatic Ar-H str)

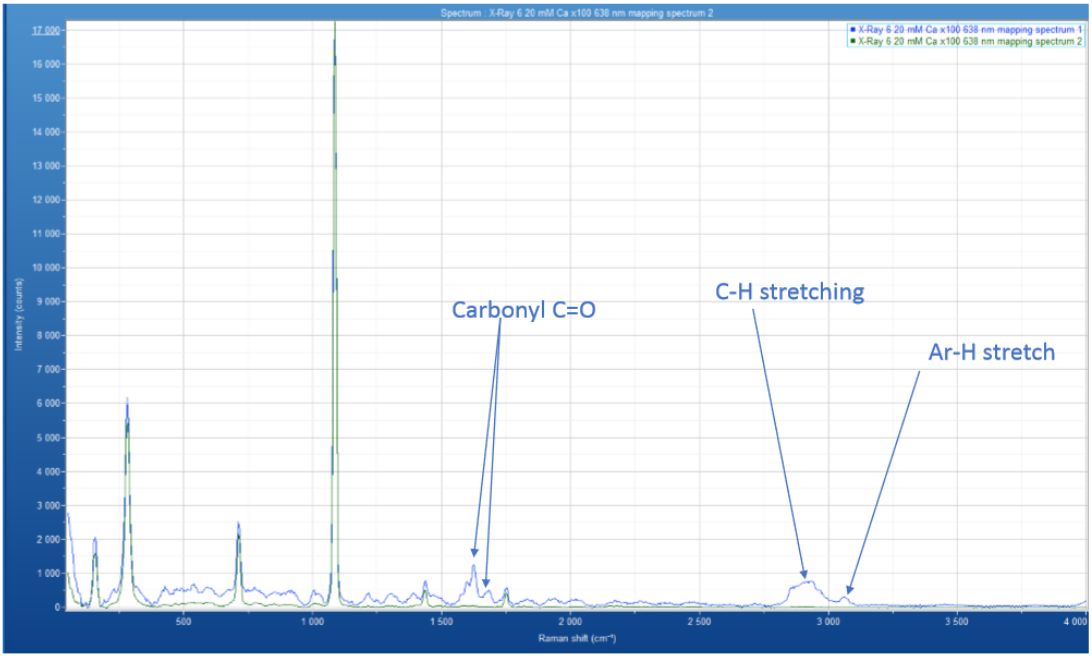

Figure A6. IR spectra indicating the peaks used for the Raman mapping experiment, both for calcite and the organic peaks of the fragrance.

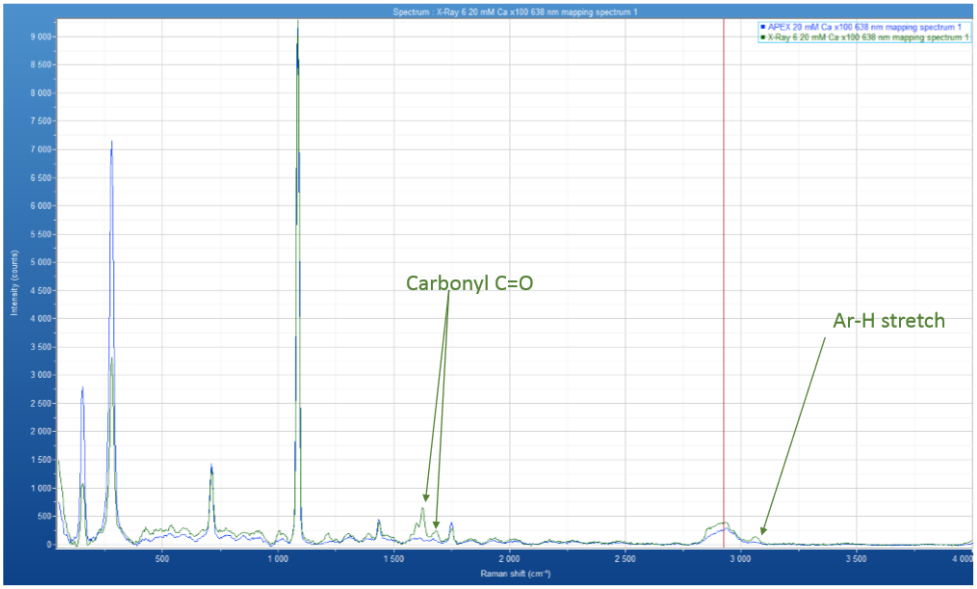

X-Ray 6 shows strong carbonyl peaks and stronger Ar-H peaks

Figure A7. Comparative IR of APEX and X-RAY 6 occluded crystals, both synthesised at 20 mM [Ca^{2+}], showing that the peaks for X-RAY 6 are more intense and strong when compared to APEX. This could be due to higher extent of occlusion or purely due to structural differences between the fragrances.